

Progressive damage analysis of Open-Hole Compression based on a delamination-dependent bending-fracture model for fibre kinking and the Floating Node Method

MASTER OF SCIENCE THESIS

V. T. Mateescu



Progressive damage analysis of Open-Hole Compression based on a delamination-dependent bending-fracture model for fibre kinking and the Floating Node Method

MASTER OF SCIENCE THESIS

by

V. T. Mateescu

to obtain the degree of Master of Science
at the Delft University of Technology,
to be defended publicly on March 8, 2019 at 14:00.

Student number:	4273214	
Thesis committee:	Dr. B. Chen,	Supervisor
	Dr. S. R. Turteltaub,	Chair
	Dr. R. C. Alderliesten,	Examiner

This thesis is confidential and cannot be made public until March 08, 2019.

An electronic version of this thesis is available at <http://repository.tudelft.nl/>.

Preface

Dear reader,

This report describes my work for almost one year on a topic that took me a long time to find. I wanted my last student project to be on something difficult and industry relevant. At the time of writing, fiber reinforced polymers are gaining ground in the commercial aircraft industry with the recently introduced Boeing 787 and the Airbus A350. In my courses on composite materials I encountered multiple times remarks like: "compression in composites is a Pandora's box" or "composites and compression should not be used in the same sentence". Enticed by the challenge I started looking for subjects into this field. Dr. Chen was interested in the topic so, under his guidance, I started a long phase of literature study trying to find something new and yet feasible to do for my master thesis. While reading I discovered a world of overall disagreement between the believed compressive mechanisms of fibers in compression and simulation frameworks that treat compression as if it was tension. Nevertheless there are also extremely valuable researches, some of which provided a foundation for this thesis. We decided to focus the thesis on the industry relevant open hole compression problem which would be modelled using our own physically based constitutive law for fibers in compression. This be implemented into the relatively new Floating Node Method (used for the first time for an Open Hole Compression simulation). This report presents the constitutive law proposed, describes concisely how the Floating Node Method works and how are the two integrated. Anyone with interest in the field of composite design will enjoy reading this report. Readers with prior experience with the Open Hole Compression problem and the Floating Node Method are encouraged to read directly from chapter 4. The writer would like to express his gratitude towards his supervisor, Dr. Boyang Chen, for his invaluable advises. Moreover, a big thanks to Bas Tijs from Fokker Aerostructures for his help during the meetings. Finally, my productivity level would not have been the same without the office provided by the department of Aerospace Structures and Computational Mechanics.

V.T. Mateescu

Abstract

Strong, stiff and lightweight, high performance Fiber Reinforced Polymers (FRP) meant for the aerospace industry a turning point in terms of structural design. In a time where fuel efficiency (society expectations) and cost reduction (economics) are the major terms deciding if an aircraft will sell, composite materials quickly gained importance, offering the perspective of lighter structures. The Boeing 707, launched at the end of the 50's, was the first commercial airliner to use composites, representing about 2% of the structural weight. In 2015 the Airbus 350 was launched, containing composite materials accounting for just over 50% of the structural weight. Those very prudent steps made by the industry are, among others, an indicator that also downsides are associated with composites: high cost, the need of specialized repair techniques, damage tolerance requirements, non-destructive inspection requirements, troubles in failure prediction and the absence of existing design data. Despite decades of research trying to improve on the mentioned downsides, composite materials are still not used at their full potential. Meeting damage tolerance requirements is challenging as, due to their anisotropic nature, FRP are characterized by higher than normal concentration factors in the presence of damage and structural holes. Even if somehow damage is avoided (which is impossible), aircraft structures are clustered with holes of different sizes e.g. windows, doors, passing fuel and hydraulic pipes, outside sensors (Pitot tubes), etc.. Holes are the actually one of the most common stress raisers, making their design one of the most critical parts in composite structures. But even without the holes present there is a general inability of making consistent accurate failure predictions, aspect made clear by The World Wide Failure Exercise. State of the art Finite Element based Progressive Damage Analyses (PDA) are limited by the poor modelling of composites governing mechanisms. Academia is actively striving to find new failure theories that capture the correct physical basis. Compression failure mechanisms are arguably less understood than those tension related, which has led a number of authors to model compression as if it was identical to tension. In compression however, despite the fibers being the main load bearers, the matrix plays the essential role of laterally supporting the fibers. Failure of the matrix results in local instabilities and further into complex strain fields. These cause compression failure to occur at significantly lower stresses than tension failure and makes it a more critical design factor. Using FRP efficiently requires then, among other things, a good understanding of its compressive mechanisms and behavior in the presence of holes or notches. This is what makes the problem of Open-Hole Compression in FRP panels to be extensively treated by the academic and industrial environments.

This thesis is focused on delivering a computational framework capable of accurately simulating OHC. The increasingly popular Discrete Crack Models (DCM) are preferred to Continuum Damage Models (CDM) for modelling cracks in PDAs as they explicitly represent discontinuities. The popular state of the art eXtended Finite Element Method as implemented in Abaqus is shown in this report to be unable to simulate the problem of OHC beyond an incipient state of failure. A novel approach, the Floating Node Method (FNM), that has been used recently to simulate several Open Hole Tension (OHT) problems is adopted instead. The method had no convergence issues up to an extensive failure propagation state. In addition to the explicit representation of cracks, the OHC simulation requires a physically accurate constitutive model for compression specific failure modes. The expected dominant failure mode for OHC is fiber kinking. This work proposes a new 3D constitutive law that incorporates the microscale bending stress of a fiber, under the assumptions of the Euler-Bernoulli beam theory, in the kink band within the framework of meso scale CDM. The proposed hypothesis for kinking onset is that the following three non-competing requirements need to be met: 1) the matrix around the kinking fibers must have failed locally; 2) the maximum bending stress in a fiber should be large enough to fracture it; 3) the longitudinal compressive stress must be large enough to satisfy the previous requirement when the shear in the kink plane is smaller than the traverse shear strength of a ply. While the first requirement is commonly adopted in kinking theories, the second is new and based on fractographic investigation of kink bands. The third requirement, supported by experimental results, is meant to distinguish fiber kinking from the similar shear dominated fiber splitting phenomenon. After kinking onset, in contrast to using standard linear softening laws, a bilinear cohesive law, obtained via superimposition, is used to more accurately represent the physics behind softening and assure that the dissipated fracture energy is mesh ob-

jective. In the last softening stages, where constitutive laws typically assume that stress converges to a traction free or crushing state, the proposed model assumes that a traction free state can only be achieved if the kink band terminations are able to escape out of plane on either side of the ply through existing delaminations.

The model described for kinking is implemented within the FNM and the full simulation framework is used to model different sized $[45/90/-45/0]_s$ OHC laminates using the IM7/8552 ply material system. This validation against experimental results shows that the predicted panel strengths do not exceed experimental results by more than 8% while both thickness and in plane size effects are captured.

Nomenclature

Acronyms

C3D8	8 node linear brick element
CDM	Continuum Damage Model
CE	Cohesive Element
CLPT	Classical Laminated Plate Theory
COH3D8	8 node 3D cohesive element
DCM	Discrete Crack Model
DGD	Deformation Gradient Decomposition
DoF	Degree of Freedom
FEM	Finite Elements Method
FNM	Floating Node Method
FRP	Fiber Reinforced Polymers
LEFM	Linear Elastic Fracture Mechanics
OH	Open Hole
OHC	Open Hole Compression
OHT	Open Hole Tension
PDA	Progressive Damage Analysis
PNM	Phantom Node Method
PSM	Point Stress Model
SCF	Stress Concentration Factor
UMAT	User Material Subroutine
VCCT	Virtual Crack Closure Technique
XFEM	eXtended Finite Element Method

Greek Symbols

β	(only in ch 2) kink band angle	rad
$\sigma^{(\theta)}$	kink plane stress matrix	MPa
$\sigma^{(\varphi)}$	misalignment plane stress matrix	MPa
σ	stress matrix	MPa
δ_l	separation between surfaces in longitudinal shear direction	mm
δ_n	separation between surfaces in normal direction	mm

δ_t	separation between surfaces in traverse shear direction	mm
δ_c	traction free axial displacement	mm
η_L	longitudinal angle of internal shear	rad
η_T	traverse angle of internal shear	rad
Γ_Ω	(only in ch 2) boundary of a physical domain	–
Γ_{Ω_c}	(only in ch 2) surface of a cohesive crack	–
ϵ	(only in ch 2) strain tensor	–
ν'	damaged ply poisson ratio	–
ϕ_0	fracture plane angle under a purely compressive load	rad
Φ_{KMC}	compression matrix failure index in the kinking criterion	–
Φ_{KMT}	tension matrix failure index in the kinking criterion	–
Φ_{KM}	matrix failure index in the kinking criterion	–
σ_c	(only in ch 2) critical kinking stress	MPa
$\sigma_{11_{min}}$	minimum axial stress for kinking	MPa
$\sigma_{b_{max}}$	maximum bending stress in a fiber	MPa
σ_{crush}	mean crushing stress	MPa
$\sigma_{fib_{max}}$	strength of a single fiber	MPa
$\sigma_{simulation}$	simulated panel strength	MPa
σ_{test}	experimentally determined panel strength	MPa
$\tau_{12}^{(\theta)}$	kink plane shear stress	MPa
τ_l	longitudinal shear traction on matrix crack surface	MPa
τ_n	normal traction on matrix crack surface	MPa
τ_t	traverse shear traction on matrix crack surface	MPa
τ_{12}	shear stress	MPa
θ	(in ch 2) the location along the circumference of a circular hole	rad
θ	kink plane angle	rad
ν_f	fiber volume fraction	–
ϵ_0	longitudinal strain at kinking onset	–
φ	fiber misalignment angle	rad
φ_0	initial misalignment angle	rad
w_{kink}	kink band width	mm
Roman Symbols		
ΔT_{min}	minimum allowed time increment	s
$\frac{E}{E_{nn}}$	(only in ch 3) penalty stiffness in mode i	MPa/mm

$\frac{G_1}{E_{ss}}$	(only in ch 3) penalty stiffness in mode ii	MPa/mm
$\frac{G_2}{E_{tt}}$	(only in ch 3) penalty stiffness in mode iii	MPa/mm
γ_m	shear strain	–
γ_{mC}	shear strain at failure under a purely compressive load	–
J	jacobian matrix	–
K	stiffness matrix	MPa
Q	tensor of forces	kN
q	tensor of degrees of freedom	mm
R	transformation matrix	–
u	tensor of displacements	mm
x	tensor of nodal coordinates	mm
ν	poisson's ratio	–
φ_0	initial misalignment angle	rad
φ_C	misalignment angle at failure under a purely compressive load	rad
a_0	(only in ch 2) characteristic distance in the method of Whitney and Nuismer	m
A_{fib}	fiber cross sectional area	mm ²
d_0	(only in ch 2) characteristic distance in the method of Whitney and Nuismer	m
d_f	fiber damage variable	–
d_m	matrix damage variable	–
d_{fib}	fiber diameter	mm
E_1	longitudinal axial stiffness	MPa
E_{11}^L	(only in ch 2) smeared laminate elastic longitudinal stiffness	Pa
E_{22}^L	(only in ch 2) smeared laminate elastic traverse stiffness	Pa
E'_1	damaged ply longitudinal stiffness	MPa
$E'_{II,slender}$	equivalent elastic modulus for orthotropic materials	MPa
E'_{II}	equivalent elastic modulus for a slender body	MPa
f_{index_c}	matrix failure index for compression	–
f_{index_t}	matrix failure index for tension	–
G_m	(only in ch 2) effective longitudinal shear modulus of the laminate	MPa
G_{12}^L	(only in ch 2) smeared laminate shear modulus	Pa
G_{fc}^1	individual ply compressive fracture toughness	kJ/m ²
G_{fc}^n	ply block compressive fracture toughness	kJ/m ²
I_{fib}	area moment of inertia of a fiber	mm ⁴
K_l	penalty stiffness in longitudinal shear direction	MPa/mm

K_n	penalty stiffness in normal direction	MPa/mm
K_t	penalty stiffness in traverse shear direction	MPa/mm
k_t^∞	stress concentration factor of a plate with infinite width	–
l_{ch}	cohesive zone length	mm
M	moment due to fiber misalignment	N × m
R_c	(only in ch 2) characteristic distance in the method of Garbo and Ognowski	m
S_L	ply longitudinal shear strength	MPa
S_T	ply traverse shear strength	MPa
$t_L^{(\varphi)}$	longitudinal shear traction on the fracture plane	MPa
$t_N^{(\varphi)}$	normal traction on the fracture plane	MPa
$t_T^{(\varphi)}$	traverse shear traction on the fracture plane	MPa
u_0	displacement at failure onset	mm
u_1	vertical displacement	mm
w_{MA}	moment arm	mm
X_c	ply longitudinal compressive strength	MPa
X_t	ply longitudinal tensile strength	MPa
\mathbf{t}	(only in ch 2) traction on a material boundary	MPa
d	hole diameter	mm
f	(only in ch 2) body force per unit volume	N/m ³
h	(only in ch 3) half laminate thickness	mm
m	fracture toughness ratio	–
N	shape function	–
n	peak stress ratio	–
t	panel thickness	mm
\mathbf{u}	(only in ch 2) displacement vector of a point	mm
v	(only in ch 2) test function	–
W	plate width	mm

Contents

Abstract	v
Nomenclature	vii
1 Introduction	1
2 Existing Approaches to the Open Hole Compression problem	5
2.1 Early approaches and theoretical concepts	5
2.2 The fiber kinking phenomenon	7
2.3 Numerical FE based concepts and tools.	8
2.3.1 Basic concepts	8
2.3.2 Continuum Damage Models	9
2.3.3 Discrete Crack Models	10
2.4 Main take-aways	11
3 Discrete Crack Models in OHC	13
3.1 Existing Simulation Capabilities	13
3.2 The Floating Node Method	16
3.2.1 Method Description	17
3.2.2 Modelling of Composite Laminates	19
3.2.3 OHC simulation with the FNM.	20
3.2.4 Discussion of results	21
4 Modelling of longitudinal compression in composites	25
4.1 Background	25
4.2 Proposed constitutive law.	26
4.2.1 Failure Onset.	27
4.2.2 Softening Behaviour	33
4.2.3 Crushing.	34
5 Verification	37
5.1 Failure Envelope	37
5.2 Cohesive Law	40
5.3 Delamination and cracks in compression.	42
5.4 Mesh dependency	42
6 Validation	47
6.1 Comparison with the maximum stress based model	47
6.2 Mesh dependency of the OHC problem.	50
6.3 Sensitivity to used time increment	53
6.4 Thickness scaling	54
6.5 In plane scaling	56
6.6 Results Summary and experimental comparison	58
7 Conclusions and Recommendations	61
7.1 Recommendations for future work	62
A Standard OHC-test setup	63
B All Panel Simulation Results	65
B.1 31.75 mm × 31.75 mm × 2 mm; Δ T=0.005 s; Mesh: Original; Failure Criterion: Maximum Stress	65
B.2 31.75 mm × 31.75 mm × 2 mm; Δ T=0.005 s; Mesh: Original; Failure Criterion: Proposed Method . . .	67
B.3 31.75 mm × 31.75 mm × 2 mm; Δ T=0.005 s; Mesh: Coarse; Failure Criterion: Proposed Method . . .	69
B.4 31.75 mm × 31.75 mm × 2 mm; Δ T=0.005 s; Mesh: Refined; Failure Criterion: Proposed Method. . .	71

B.5	31.75 mm × 31.75 mm × 2 mm; Δ T=0.025 s; Mesh: Original; Failure Criterion: Proposed Method . .	72
B.6	31.75 mm × 31.75 mm × 2 mm; Δ T=0.001 s; Mesh: Original; Failure Criterion: Proposed Method . .	74
B.7	31.75 mm × 31.75 mm × 4 mm; Δ T=0.005 s; Mesh: Original; Failure Criterion: Proposed Method . .	76
B.8	127 mm × 127 mm × 4 mm; Δ T=0.005 s; Failure Criterion: Proposed Method	77
Bibliography		79

Introduction

Background and motivation

High performance Fiber Reinforced Polymers (FRP) are a type of composite materials that are used increasingly more. The aerospace industry has been for decades the largest and arguably most important market for composite materials. Their popularity was propelled by their impressive strength to weight ratio which offered the perspective of lighter structures in a time of more and more strict environmental regulations and rising fuel costs. Being made of at least two unhomogenized materials they have a strong heterogeneous and anisotropic nature making them exhibit a multitude of failure mechanisms (damage may be specific to either constituent as well as an interaction of the two). The journey of integrating composites in aviation was long and lined with pitfalls and is far from over. The Boeing 707, launched at the end of the 50's, was the first commercial airliner to use composites, representing only about 2% of the structural weight. In 2015 the Airbus 350 was launched, containing composite materials accounting for just over 50% of the structural weight. Decades of research were needed to get here and a lot of problems still exist making aircraft manufacturers hesitant in adopting composites at a faster pace. Aside from the higher cost associated that comes with them (raw material, clear rooms, specialized repair techniques) they have problems meeting damage tolerance requirements and troubles in failure prediction. Damage tolerance means that the structural design is made such that the damage expected to occur throughout the lifetime of a structure will not result in a loss of load carrying capacity. If the force causing the damage is strong enough to penetrate through the thickness, then the appropriate term to use is a puncture or damage hole. But even without any prior damage, aircraft structures are full of holes of different sizes [48]. A short walk through the materials hall of the Aerospace Engineering faculty at the Technical University of Delft is enough to such examples eg. fuselage skin cutouts for windows presented in figure 1.1, lightening holes and cutouts for stringers (both in the fuselage frames) are both shown in figure 1.2 alongside a tube reaching out through the skin.

FRP are known to be notch sensitive and despite having some reduced load redistribution capabilities represented by the formation of a damage zone around the notch, they are generally more notch sensitive than metals. The study of open holes is divided in Open Hole Tension (OHT) and Open Hole Compression (OHC) the two being characterized by different failure mechanisms. Unlike tension, in compression the matrix plays the essential role of laterally supporting the fibers. Failure of the matrix results in local instabilities and further into complex strain fields. These cause compression failure to occur at significantly lower stresses than tension failure and makes it a more critical design factor. With the industry relying more and more on the predictive capability of modern computational tools, a high demand exists on delivering them. While OHT has seen some recent success in modelling, due to the arguably less understood compressive failure modes of FRP, OHC is lagging behind. A proof of the deficiencies and disagreements of modern failure theories for compression was provided by The World Wide Failure Exercise (WWFE) [47] which showed relatively large discrepancies between the proposed failure envelopes when axial compression was applied (eg. the LaRC's, Hashin, Hashin-Rotem, Puck, etc..). The academic world is still actively proposing new failure theories with larger physical basis [7]. State of the art Finite Element based Progressive Damage Analyses (PDA) are limited by the inaccurate modelling of compressive governing mechanisms. Using FRP efficiently in airplanes



Figure 1.1: Fuselage cutouts for windows

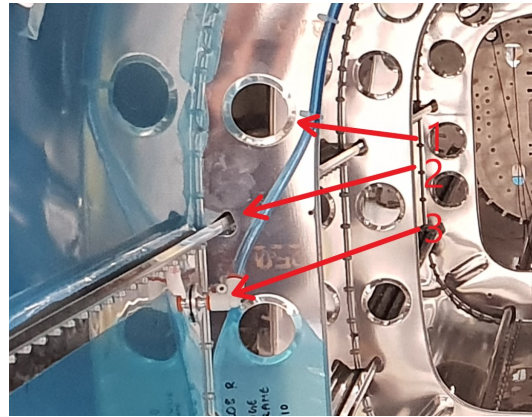


Figure 1.2: General aviation airplane: 1)Lightening Hole; 2)Stringer passing through fuselage frame; 3)Tube reaching out

requires then, among other things, a good understanding of their compressive mechanisms and behavior in the presence of holes or notches. This is what makes the problem of Open-Hole Compression so important in the industrial and academic environments.

Research Scope

The **problem statement** as resulting from the previous discussion can be written as: In an ideal scenario, the aerospace industry will have the simulation capabilities to design more efficient compressively loaded composite structures while decreasing the overall price of product development. An accurate and reliable simulation framework capable of modelling open hole compression problems of fiber reinforced polymer structures is largely unavailable. In response to this issue, the current work will investigate the possibilities to improve the current simulation methods. The proposed improvements will be implemented and tested against experimentally obtained values of open hole compression tests of fibre reinforced polymers.

A set of four **research questions** can be formulated in response to the problem statement:

1. What are the main shortcomings of the existing simulation frameworks for composites in compression?
2. How can each of these shortcomings be addressed?
3. What is the performance of a simulation framework where the shortcomings have been addressed?
 - (a) How mesh objective is the new solution to the OHC problem?
 - (b) Is the proposed method time step dependent?
 - (c) Can thickness size effects be captured?
 - (d) Can in plane size effects be captured?

The **research objective** of the thesis can then be formulated as: The aim of the current research is to create a simulation framework that can accurately model the OHC problem of fiber reinforced polymers.

The **research approach** will be here shortly described. It starts by investigating the past approaches to the Open Hole Compression problem in Fiber Reinforced Polymers from the beginning all the way to the current state of the art. The main shortcomings and conclusions obtained from the earlier investigation will be collected. A new model will be proposed addressing the main shortcomings of the discussed models and will be verified. Open Hole Compression simulations will then be performed and assessed against experimental values.

Report Layout

The report starts with a review of the relevant literature for OHC presented in chapter 2. In here concepts like stress concentration factor, damage zone and continuum damage approach are introduced and the main shortcomings of existing OHC models are identified. In short, it is concluded that two of the most important deficiencies of the existing Progressive Damage Analyses for OHC are the unsatisfactory representation of matrix cracks (and other discontinuities) as well as the insufficient physical basis behind the modelling of failure mechanisms specific to fibers in compression. Therefore Discrete Crack Models are preferred to Continuum Damage Models for modelling cracks and a more physically accurate longitudinal compressive constitutive law is has to be used. Chapter 3 is dedicated to Discrete Crack Modelling techniques. The commercially available state of the art eXtended Finite Element Modelling is used to reproduce a compressive test presented in Appendix A. Afterwards the recent Floating Node Method is introduced and used to simulate the same test and the performances of the two methods are compared. Chapter 4 focuses on the second identified issue of modelling longitudinal compression and describes a proposed Continuum Damage Model for the fiber kinking failure mode. The kinking model implementation, validity and robustness are verified in chapter 5 while the full simulation framework is used in chapter 6 to model the OHC problem and validate the results against experimental data.

2

Existing Approaches to the Open Hole Compression problem

2.1 Early approaches and theoretical concepts

Before the emergence of numerical methods in structural design, analytic methods were used to estimate stress in the surroundings of holes. These methods become mathematically challenging for anisotropic materials such as Fiber Reinforced Polymers. Only in 1963, the first successful expression for the stress around an elliptical hole in an infinite orthotropic symmetric laminate, was made by Lekhnitskii [53]. The circumferential Stress Concentration Factor (SCF) derived is presented in equation (2.1). This formulation is applicable only to laminates behaving linearly elastic at the edge of a hole. The terms E_{11}^L , E_{22}^L , G_{12}^L and ν_{12} are constants representing of the laminate (smeared ply elastic properties). FRP are not fully notch sensitive [48], meaning that the actual failure of the panel occurs significantly after the material has failed near the hole. Fracture right on the hole edge only creates a damage zone, depicted in figure 2.1, which redistributes the stress and decreases the SCF. What this means is that accurate prediction of the final failure load of a wide (infinite plate assumption) panel is not equivalent to dividing the unnotched panel strength by the SCF in equation (2.1).

$$k_t^\infty = \frac{-K \cos^2 \theta + (1 + \sqrt{2K - m}) \sin^2 \theta}{\sin^4 \theta - m \sin^2 \theta \cos^2 \theta + K^2 \cos^4 \theta} \text{ where } K = \sqrt{\frac{E_{11}^L}{E_{22}^L}} \quad m = 2\nu_{12} - \frac{E_{11}^L}{G_{12}^L} \quad (2.1)$$

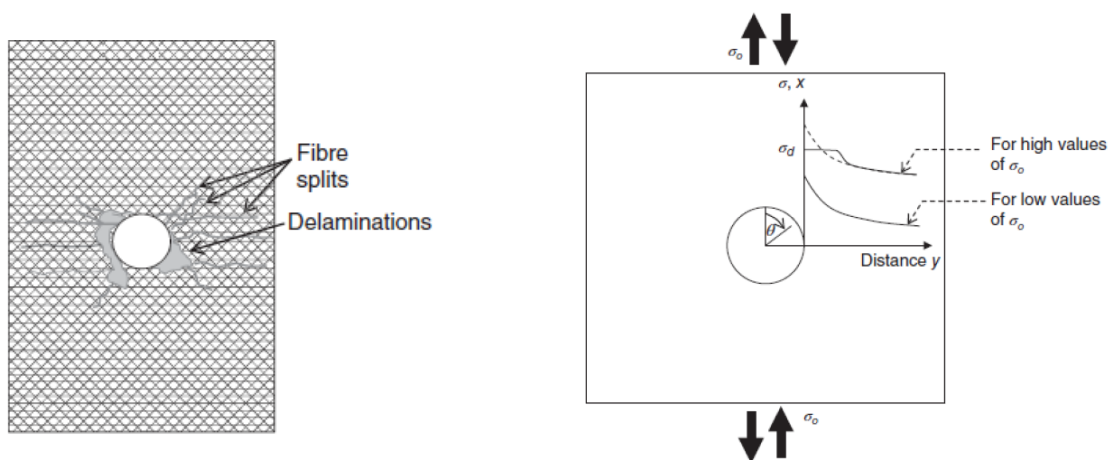


Figure 2.1: Damage zone around the edges of the hole [48] Figure 2.2: Load drop at the edges of a hole due to the damage zone [48]

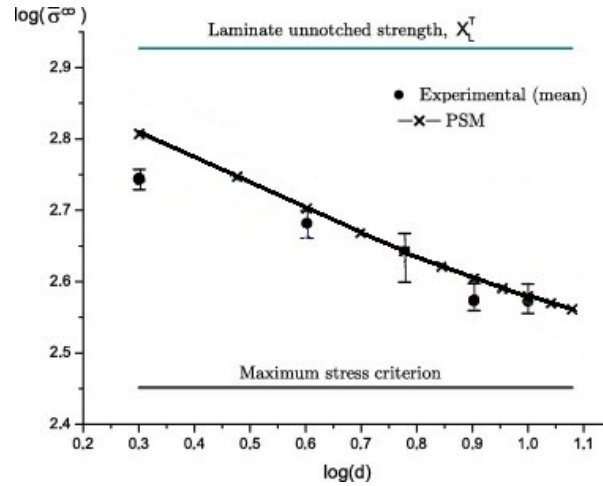


Figure 2.3: Comparison PSM with experimental data (based on [13])

The first analytic approach for estimating the strength of notched plates was proposed, more than a decade after Lekhnitskii (1963), by Whitney and Nuismer [77] (1974). This approach commonly adopted to this day, in applications where computational resources are limited, by virtue of its simplicity. The authors acknowledged the existence of the damage zone and proposed two approaches that don't require the knowledge of the redistributed stress after the damage zone is created. Both approaches require an estimation of the circumferential stress evolution away from the hole edge. Tan [72] proposed such an approximation, provided in equation (2.2) at $\theta = 90^\circ$ (see figure 2.2). The stress is given as a function of the distance from the hole center y . R represents the radius of the hole, σ_0 , the stress applied at the top and k_t^∞ is the SCF for a plate with infinite width that can be approximated using the equation of Lekhnitskii (eq. (2.1)).

$$\sigma_x(x=0, y) = \sigma_0 \left[1 + \frac{1}{2} \left(\frac{R}{y} \right)^2 + \frac{3}{2} \left(\frac{R}{y} \right)^4 - (k_t^\infty - 3) \left(\frac{5}{2} \left(\frac{R}{y} \right)^6 - \frac{7}{2} \left(\frac{R}{y} \right)^8 \right) \right] \quad (2.2)$$

In the method of Whitney and Nuismer, the stress is evaluated at a characteristic distance d_0 from the edge of the hole (eg. using (2.2) provided that the highest stress occurs at $\theta = 90^\circ$). If the stress value is superior to the strength of the un-notched panel, the has panel is deemed failed. In the second approach, the average stress over a characteristic distance a_0 is evaluated and is compared again to the un-notched plate strength to declare failure. The distances d_0 and a_0 have to be determined experimentally. They are different from each other and are different for tension and compression. At first they were thought to be material constants, but it was further determined that they vary from layup to layup, making the approach unpractical due to extensive need of experimental data [42]. The work of Whitney and Nuismer [77] can then be regarded as a failure criteria that does not capture any undergoing physical mechanism. It however represents the first endeavour to estimate the strength of OH composite panels. Due to its success, some researchers suggested improvements to this approach.

Garbo and Ognowski [31] proposed to use the Classical Laminated Plate Theory (CLPT) to determine the stress in each ply of the laminate. Then, as before, the stress would be evaluated at a characteristic distance R_c from the hole. Failure occurs if the stress there is larger than the the un-notched ply strength. The novelty of this method is that it treats the laminate not as a homogenous material, but as being made of distinct parts (plies). The method is however not any more practical than that of Whitney and Nuismer as the characteristic distance R_c is still not a material constant and depends on the layup. The problem in general with criteria not representing undergoing failure mechanisms is that they have a limited scope of applicability. They work well for specimens very similar to those used to get the inputs they needed. Camanho [13] shows the reduced envelope of applicability of the Point Stress Model (PSM) by comparing its strength predictions with experimental data for a larger set of coupon sizes. The results of the comparison can be seen in figure 2.3. As one may expect, the PSM provides accurate results only for specimens with holes of diameters similar to those used to obtain the material properties and characteristic distance.

Kassapoglou [48] proposes a variant of the PSM that aims to solve this limitation. In this work an analytic approach to estimate the characteristic length a_0 of the Whitney Nuismer method is provided, eliminating the extensive need of empirical data given that the maximum SCF around the hole is at $\theta = 90^\circ$ in figure 2.2. The characteristic length a_0 is estimated as a function of the hole radius R and the width of the panel W . From the validation performed [48], the author shows that improved results compared to the original Whitney and Nuismer could be obtained for a $[30/-30/0]_s$ layup especially. In comparisons where layups $[15/-15/0]_s$, $[45/-45/0]_s$ the correlation between estimations and experimental results diminishes, predominantly for larger holes. Finally, when a $[90]_4$ layup is used, the match with experimental data is unsatisfactory. The reason for that is because failure mechanisms are layup, geometry and size dependent and cannot all be captured. Moreover, the author explains that due to the damage accumulating in the laminate (eg. traverse matrix cracks), the traverse stiffness decreases in that ply and the location of the maximum SCF would move as well from $\theta = 90^\circ$. This discussion proves the importance of accounting for the right failure mechanisms and the changes in the panel as damage evolves when modeling holes in composite panels. For this reason Progressive Damage Analyses (PDA) based on the Finite Element Method (FEM), discussed later in this chapter, represent the current state of the art in terms of accuracy. Before jumping into discussing FE based modelling approaches one needs to understand the failure mechanism needs to be modelled.

2.2 The fiber kinking phenomenon

Studies performed on the OHC tests of fiber reinforced composites show that the dominant failure mechanism, given the matrix material is ductile, is kinking of the 0° plies [73]. The failure mode is of primary concern in FRP as it can lower the failure load of a structure significantly [69]. Therefore, an accurate representation of this failure mode is necessary for a good OHC prediction. The truth is that the fiber kinking phenomenon is not that well understood to this day. This can be attributed to the fact that experimental observations of kink bands are difficult as a result of their reduced size (only 10-20 times the fiber diameter [29][35]). Moreover, they are generally observed in materials after they have failed, so not much is known about their formation. To this day, conflicting theories still exist regarding the initiation.

At the basis of most kinking approximation models stand three hypotheses: micro-buckling theory, kinking theory and bending theory.

- The first scientific writing on micro buckling theory was performed in 1965 by Rosen [68]. According to which the fiber kinking failure mode is the result of the micro-buckling of fibres. His approximation for the critical kinking stress is $\sigma_c = G_m / (1 - v_f)$. In this last equation, the term G_m represents the effective longitudinal shear modulus of the laminate, while v_f is the fiber volume fraction. It was later discovered by Budiansky and Fleck [11] that the above formula is generally substantially overestimating the reality. Finally, Waas et. al. [76] argues against micro mechanical theories stating that if micro buckling theories would indeed describe kink band formation, the micro buckling of the fibers should occur almost simultaneously in the panel (which is not the case, as this was determined to be a progressive failure).
- Another popular hypothesis is that of Argon [4] (kinking theory) arguing that kinking is a result of local matrix failure in the kink band. An idealized depiction of the kink band can be seen in figure 2.4. In this figure, the main parameters observed are the fiber misalignment angle φ , the kink band angle β and the band width of the kink w_{kink} (or W according to other sources). The kinking theory considers that specimens contain initially misaligned fibers (misalignment angle φ_0). As the externally applied load increases, the initially misaligned fibers rotate within their initial band. The shear stress thus appearing

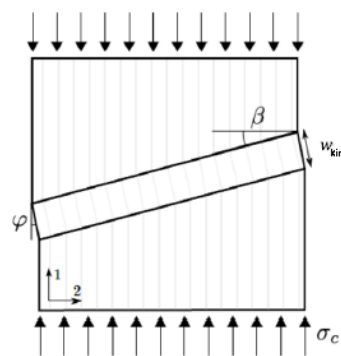


Figure 2.4: Kink band depiction [8]

damages the matrix, which softens, and further allows for fiber rotation. Upon the matrix material in the kink band reaching its maximum strength, fibers quickly fail as they lose their lateral support.

- Finally, bending theories were proposed by Fleck and Budiansky [29]. As the name suggests, the main characteristic of those theories is that they account for the bending stiffness of the fibres in the kink band. It was demonstrated however that the bending resistance of those fibers have a limited effect on the pre or early post failure behaviour in FRP failing in fiber kinking [25].

Researchers like Andrew C. et. al. [7] support the idea that the poor physical basis of the current progressive damage analysis is one of the main factors of their insufficient accuracy when modelling compressive tests. Fiber kinking is the expected dominant failure mechanism in the OHC problem, and the accuracy of such a simulation depends a lot on accurately modelling fiber kinking.

2.3 Numerical FE based concepts and tools

After the emergence of the Finite Elements Method (FEM) effort has been put into developing simulations for OHC problems using this method. The empirical dependency of the previous methods is diminished at the expense of increasing computational load.

2.3.1 Basic concepts

FEM is capable of solving the static equilibrium of a body of volume Ω , acted upon by body forces of density \mathbf{f} and traction \mathbf{t} on its boundary Γ_Ω , in its weak form (shown in equation (2.3)). Furthermore, the method can account for the evolution of loads and damage in solids. For this reasons, FEM represents a powerful tool for performing complex PDA.

$$\int_{\Omega} \boldsymbol{\epsilon}^T(\mathbf{v})\boldsymbol{\sigma}(\mathbf{u})d\Omega = \int_{\Omega} \mathbf{v}^T\mathbf{f}d\Omega + \int_{\Gamma_\Omega} \mathbf{v}^T\mathbf{t}d\Gamma_\Omega \quad (2.3)$$

Chen et al [21] states that accurately modelling discontinuities (eg. matrix cracks) is crucial for approximating the solution of OH problems. A standard FE is quite limited when it comes to modelling domain discontinuities due to its simple element formulation which cannot incorporate displacements and stress jumps. This led to the use of remeshing methods for modelling progressing damage [43]. In general, the latter uses the standard FE definition and periodically updates the geometrical description of the domain. This way it allows the discontinuities to propagate, but only along an element's boundary. For each time increment in which discontinuities have propagated, remeshing is needed such that the element boundaries can adapt to the discontinuities (the new geometry). In the case of composite laminates, where an extensive system of cracks precedes the final failure [60], remeshing methods become unpractical. Considering remeshing methods to be a special case, damage modelling in composite laminates is divided into two categories: Continuum Damage Models (CDM's) and Discrete Crack Models (DCM's). The most appropriate damage model can depend on simulation modelling scale. Currently, composite laminate models exist at three different observation scales:

- Micro-scale has the highest resolution that is commonly used in fiber reinforced composites simulations. Here, fibres and the surrounding matrix material are explicitly modelled. Local failures as well as the effects of imperfections or fiber dimensions are usually examined in this scale.
- Meso-scale considers each ply forming the laminate as an individual orthotropic and homogeneous material. The effects of micro scale phenomena need thus to be smeared throughout the homogeneous plies.
- In Macro-scale models, the entire composite laminate is considered a homogenous (anisotropic) material. These models are generally adopted for very large low fidelity simulations, where computational time must be kept within reach of available resources.

OHC simulations have been developed at all modelling scales. However, micro-scale modelling is usually avoided in the design of actual aircraft components due to the need of keeping the computational cost moderate. On top of that, despite the high resolution, to the knowledge of the author, no micro-scale OHC simulation has been proposed that accurately estimates the strength for a wide range of material parameters. Among the most notable micro-scale works on the problem of OHC is that of H.K. Lee et. al. [51], where the authors could only prove that their physically representative model is accurate only for laminates having a fiber volume fraction no higher than 45%. When factoring in the computational cost, these simulations become non attractive for direct applications on design. At the other end of the spectrum, a typical macro-scale model would not be able to capture the evolution of all failure mechanism. Therefore, most models are done at meso-scale, which will be the focus for the rest of the current work.

2.3.2 Continuum Damage Models

CDMs work by performing local decrease in properties in the regions undergoing damage, usually by implementing a material constitutive law that degrades the stiffness and Poisson ratio of the material. Consequently, CDMs are implemented as User defined MATERIAL subroutines (UMAT). An accurate meso-scale CDM can represent micro and meso-scale failure mechanisms without the computational effort associated with modelling the fiber-matrix interaction. Examples of recent, complex methods have been proposed that promise to account for micro scale phenomena such as fiber kinking [68], within a meso scale computational frame [37] [38] [7].

In order to separate the damaged and non-damaged states of the material, a trigger function (failure criteria) is required. This is a critical part in every progressive failure simulation as the failure type governing the softening behaviour is determined here. Clearly, damage evolution (eg. axial stiffness degradation) should be different if it's caused by tensile fiber failure or matrix compression. Therefore, even if there is a plethora of stress or strain based criteria available for damage initiation, in order to account for the different composite failure mechanisms, the criteria chosen must be representative to the failure mode. And while a clear trend exists now for using physically based failure criteria [75] (such as the set of LaRC criteria or the Puck criteria), those models generally come at a higher complexity and may require a greater computational effort than a mode-independent one.

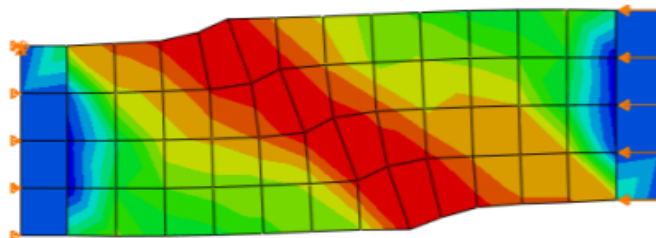


Figure 2.5: CDM representation of a crack [66]

While the CDM has previously been successfully used in modelling structural problems [57], a number of issues are typically encountered when these models are used for representing cracks. For example, the direction of crack propagation is mesh dependent [20] and the interaction between cracks is not physically captured. As an example for the latter, take delaminations that are induced by the matrix cracks exclusively (see figure 2.6). It is clear that if this phenomena occurs extensively, good estimations cannot be obtained with this approach [18]. Another problem is that sharp matrix cracks are represented by lines of softened elements, as depicted in figure 2.5. This means that the stress concentration/intensity factors are not accurately captured [21].

For these reasons Discrete Crack Models (DCM), where matrix cracks are explicitly represented, serve a better alternative for modelling matrix cracks in simulations.

Modelling other failure mechanisms, such as fiber kinking, is usually done with CDM. Creating an accurate PDA of an OHC composite plate can be done using a CDM that is physically representative to the undergoing failure mechanisms of fibers in compression.

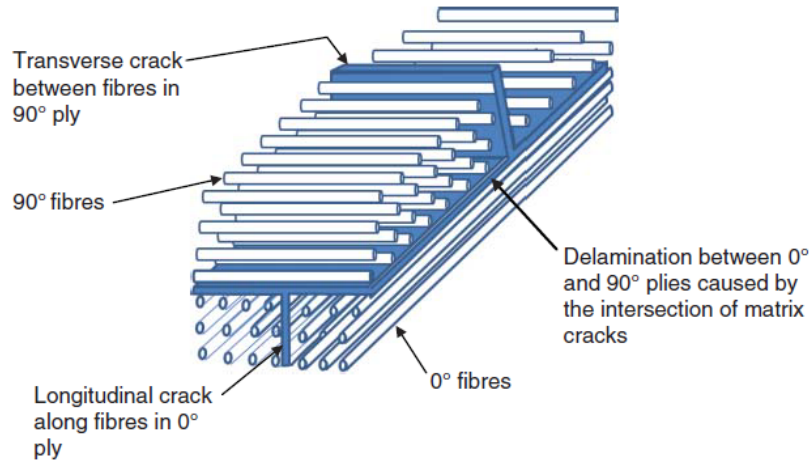


Figure 2.6: Delamination formed by intersection of cracks from different orientations [48]

2.3.3 Discrete Crack Models

The issues associated with smeared damage degradation constitutive models have led to the investigation of DCMs. The former can represent matrix cracks/delaminations and their interactions explicitly, without relying on remeshing methods.

One common way of modelling damage in composites is by introducing Cohesive Elements (CE) [33] on potential fracture paths. This approach is especially useful when modelling delaminations as they can only occur at the ply interfaces. But the location of matrix cracks is generally not known a priori [21]. Another method, called the Virtual Crack Closure Technique (VCCT) [49], is often employed and is available in standard FEM software packages (eg. Abaqus). It however functions best when modelling matrix cracks/delaminations in unidirectional laminates as the propagating crack needs to be self-similar with a predefined path. When multi-directional laminates are used however, the crack path is hard to predict (not to mention it can travel across interfaces) and the method becomes less practical [78]. Attempts have been made to use the VCCT in modelling fracture of composite laminates (not OHC) and they have not succeeded in simulating more complex simulations [78].

Another popular DCM, also available in standard FEM packages, is the eXtended Finite Element Method (XFEM) [45]. Based on the partition of unity [44], it allows for a crack to extend through a domain without knowing its path location or orientation from before. The core concept behind XFEM is to account for discontinuities by changing the displacement definition of a standard FE. Considering a simple 2D model as in figure 2.7. One can see that the nodes surrounding the crack are depicted differently. In a general form, the definition of all nodes in a simulation done with XFEM can be seen in equation (2.4). A standard node (nodes i) in this simple 2D model would have two DoF per node (one per Cartesian direction) with the standard global shape function. The nodes that are circled have two additional DoF (nodes j) whose shape functions are multiplied by the Heaviside function (or jump function) $\mathbf{H}(\mathbf{x})$ and are consequently called "Heaviside" enrichment nodes. The shape functions N_j are also related to the discontinuity at a node j . Another category of nodes (nodes k) are surrounding the crack tip. Those have eight DoF more (c_k^l) than the standard (10 in total) and are called "Crack-tip" nodes. F_l are the 4 crack tip enrichment functions while N_k are the specific shape functions.

A standard FE displacement approximation would only have the first term on the RHS of equation(2.4). One simply traversed by a crack would contain the first two terms on the RHS while one at the crack tip would have the first and last terms on the RHS.

$$u^h(x) = \sum_{i \in I} u_i N_i + \sum_{j \in J} b_j N_j H(x) + \sum_{k \in K} N_k \left[\sum_{l=1}^4 c_k^l F_l(x) \right] \quad (2.4)$$

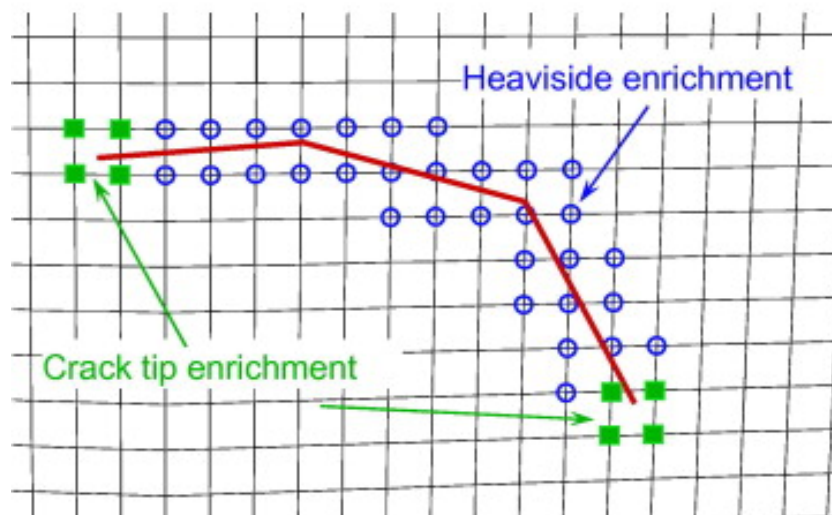


Figure 2.7: XFEM enriched elements [28]

After the emerge of XFEM, other mesh independent methods have been proposed for modelling progressive damage in composite materials. Those include the Phantom Node Method (PNM), PNM proposed by Hansbo and Hansbo [40], augmented FEM, as well as some elements with embedded discontinuities such as the cohesive segment method. Of those XFEM is commonly employed in practice and is available in standard FE software such as Abaqus.

2.4 Main take-aways

"By hand" approximation methods often have small applicable domains or are highly dependent on experimental data. FE based PDAs allow for modelling of a wide variety processes and are less reliant on empirical data. Meso-scale models are the most attractive for PDA of composite OHC problems. Depending on the failure mode (cracks, delamination, fiber kinking..), CDM or DCM may be better suited. Due to their very localized nature, matrix cracks are best modelled via DCM. Other phenomena, such as fiber kinking, can be well represented by CDM provided that physically representative constitutive laws are used. It is therefore expected that an accurate OHC simulation should address the following requirements:

1. The modelling of matrix cracks and delaminations should be done via a DCM as opposed to CDM.
2. A physically representative CDM should be used for governing compressive fiber damage initiation and propagation. Recent studies have shown that the failure mechanism governing composite longitudinal compression is fiber kinking [64].

An evaluation of the performance of the popular XFEM is done in section 3.1 while the rest of chapter 3 is dedicated to a recently proposed DCM called the Floating Node Method. Furthermore, chapter 4 proposes a CDM for fiber kinking.

3

Discrete Crack Models in OHC

3.1 Existing Simulation Capabilities

The FE software package Abaqus currently allows the use of the eXtended Finite Element Method (XFEM) as standard. The current capabilities of this FE software in simulating an OHC problem of a composite panel will be shown. For that, a 3D Finite Element model with a refined structured mesh is built. The elements of each ply are enriched with XFEM and cohesive elements are used to model each ply interface to capture delamination.

The panel geometry, layup as well as ply and inter-ply properties are presented in Appendix A together with the experimental setup. Specimen No.1 from table A.1 will be modelled as, by virtue of its reduced size and number of interfaces, it should have the smallest computational expense. To further reduce the computational effort, due to the symmetry of the stacking sequence $[45_n/90_n/-45_n/0_n]_s$, only half of the plies are physically added to the model $[45_n/90_n/-45_n/0_n]$. The remaining half is accounted for by preventing out of plane displacement on the surface of the 0° ply.

The damage initiation, evolution and stabilization properties are prescribed using a maximum stress traction-separation law. The material properties used are those of the IM7/8552 fiber epoxy system presented in table A.2. For describing the behaviour of the ply interfaces, a quadratic stress traction-separation law is used. The elastic behaviour of the cohesive elements is governed by penalty stiffness. The later aims at limiting inter-penetration of bodies by through very high stiffness. However it was determined that too high of a stiffness may result in simulation convergence issues. Since a trade-off needs to be made when choosing a penalty stiffness, a method for estimating the penalty stiffness is used. This is provided by equations (3.1), (3.2) and (3.3) from [74]. In those equations the term h represents the half laminate thickness. For a 2 mm thick laminate, $h = 1$ mm.

$$\frac{E}{E_{nn}} \approx \frac{50E_1}{h} = 7.5 \cdot 10^6 \quad (3.1) \quad \frac{G_1}{E_{ss}} \approx \frac{50G_{12}}{h} = 0.23 \cdot 10^6 \quad (3.2) \quad \frac{G_2}{E_{tt}} \approx \frac{50G_{23}}{h} = 0.17 \cdot 10^6 \left[\frac{\text{N}}{\text{mm}^3} \right] \quad (3.3)$$

Viscous regularization is used in the simulation to minimize the chances of un-convergence due to the negative tangent of the stress-displacement curve when softening (instability). The value of the viscous regularization parameter needs to be high enough to aid convergence but low enough not to pollute the results of the analysis. Unfortunately an appropriate value for the viscous parameter is hard to guess and often has to be picked by trial and error. The impact of the viscous regularization can be checked once the analysis is completed. One has to verify that the energy contribution from the viscosity (creep dissipation energy in Abaqus) is predominantly after the peak load of the analysis. For this analysis, an initial value of 10^{-4} is used for the viscosity coefficient.

Another important term for achieving convergence of the analysis is the minimum allowed time increment the solver can use. When performing a material nonlinear analysis, with viscosity, the minimum time in-

crement should be smaller than the viscous parameter defined (for the viscous regularization technique to work). To aid convergence, a very small minimum allowed time increment will be used ($\Delta T_{min} = 1.0E - 20$). The load is introduced into the panel as a negative vertical velocity of -1 mm/s as described in appendix A. The total time is chosen as such that the panel is reduced in length by 3 %.

The mesh is one of the most critical parts of a FE analysis. One generally desires a structured mesh that is refined enough to obtain accurate simulation results and coarse enough to result in a reasonable simulation time. The modelling of delamination using cohesive elements is sensitive to the size of the element [41]. For accurately capturing delamination via cohesive elements at the ply interfaces, one must make sure that the element dimensions (in critical regions) are sufficiently smaller than the size of the cohesive zone. Normally, mode I loading is the most critical (and requires a smaller cohesive element size). In the experiment reproduced however, because the plate is loaded in-plane and supported from the sides, the ply interfaces will slide upon each another in mode II shear loading. Therefore, for this analysis, mode II shear loading is considered the dominant mode producing delamination. The cohesive zone length for mode II can be estimated using equation (3.4) from [41]. In this equation, the E'_{II} and $E'_{II,slender}$ are equivalent elastic moduli. According to [41], two to three cohesive elem are required per cohesive zone. To be conservative Z.C. Su et. al. used $h=0.125$ mm (the thickness of a single ply) in their model. Sticking to the same degree of conservativeness and using the material properties in table A.2 one obtains a cohesive zone length of $l_{ch}=1.42$ mm. Assuming that two cohesive elements per cohesive zone length is sufficient a required maximum cohesive element length of 0.71 mm is determined. This is the maximum element size for which delamination is accurately captured.

$$l_{ch} = 0.5 \cdot \min(l_{ch,II}, l_{ch,slender,II}) \quad \text{where: } l_{ch,II} = E'_{II} \frac{G_s^c}{(\sigma_s^c)^2}; \quad l_{ch,slender,II} = \sqrt{\left(E'_{II,slender} \frac{G_s^c}{(\sigma_s^c)^2} \right) h} \quad (3.4)$$

Using elements of maximum 0.71 mm everywhere would result in very high computational costs, therefore it shall only be used in the delamination critical regions around the hole (near the hole the approximate element size is 0.5 mm). Experimental checks have shown a clear tendency for matrix splits in the 0° oriented plies [71] in the laminates with thicker plies (ply-level scaled). Since the model has to be able to predict the progressive failure for all laminates, the model needs to have its mesh aligned with the longitudinal splits [70]. The plies of the composite have been meshed with a C3D8, 8 node linear brick element, while the cohesive interfaces are modelled with COH3D8, 8 node 3D cohesive element. The mesh can be seen in figure 3.1. In order to minimize the computational effort, only one element per ply will be used in the thickness direction.

To account for the presence of the anti-buckling plate in the experiment, the outer surfaces of the panel are not allowed to move out of plane ($U3=0$). In order to capture the crushing (post failure) behaviour of the panel, a displacement control velocity of 1 mm/s is applied to the top of the panel while the bottom is fully clamped.

Simulation outcome

The force displacement curve in figure 3.2 presents no load drop before the end of the simulation. The simulation could converge up to a displacement of $u_1 = 0.259$ mm and an equivalent total vertical force applied of 15.32 kN. The experimentally predicted panel strength force has been exceeded by 30%.

The extent of delamination between the plies can be seen in figures 3.3, 3.5 and 3.6 (legend in figure 3.4, a value of 1 represents full delamination). Delamination is predicted via the quadratic stress criteria. As expected, delamination occurred in the regions in the vicinity of the hole. The biggest extent of the delamination is visible the interface between the -45° and 0° ply. The high quadratic stress at the edges of the panel are caused by the shear stresses between the plies. Since the plies have different orientations, they tend to deform differently upon loading, creating those shear stresses. The predicted crack network is very limited. Only the outer 45° ply has a crack, near the hole, as can be seen in figure 3.7.

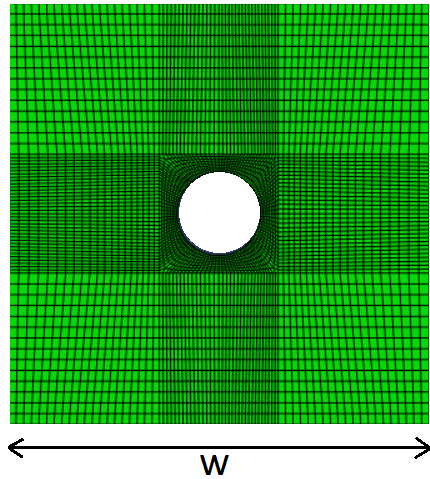


Figure 3.1: Frontal view of the meshed panel

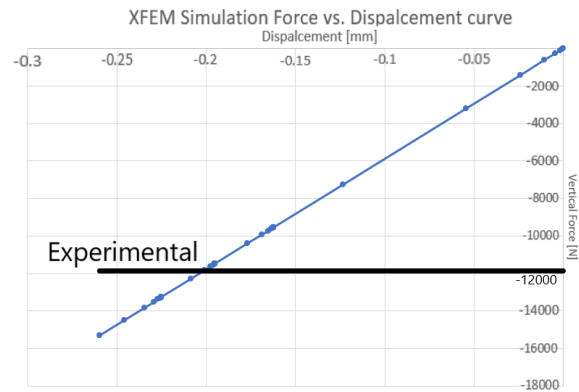


Figure 3.2: XFEM simulation Force-Displacement curve

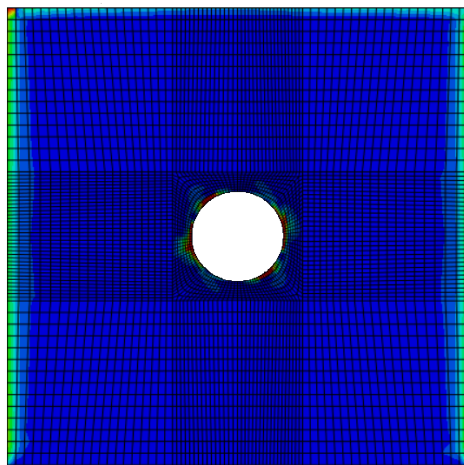


Figure 3.3: Delamination between the 45° and 90° plies

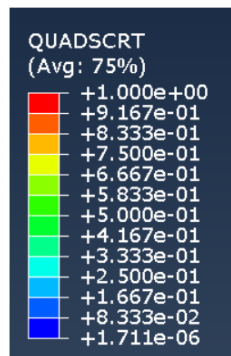


Figure 3.4: Legend quadratic stress criteria (for delamination)

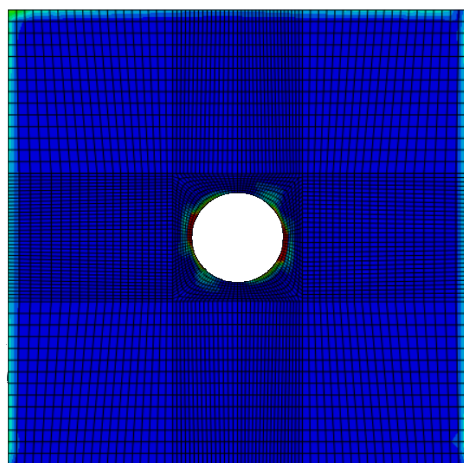


Figure 3.5: Delamination between the 90° and -45° plies

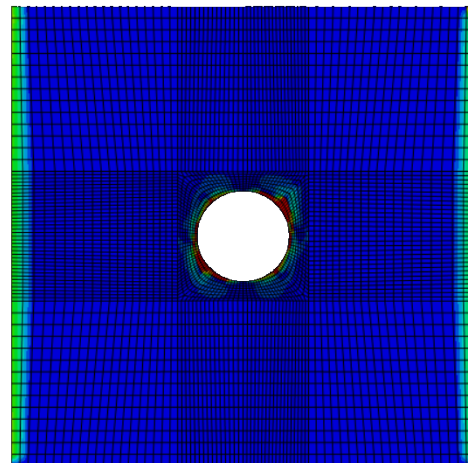


Figure 3.6: Delamination between the -45° and 0° plies

All in all, the model made using the current capabilities of Abaqus could not provide a satisfactory solution to the OHC problem. On top of this, existing literature argues that XFEM can introduce errors when mapping a discontinuity from the physical to the natural space [20]. This sparks the need for an alternative DCM to the present eXtended Finite Element Method.

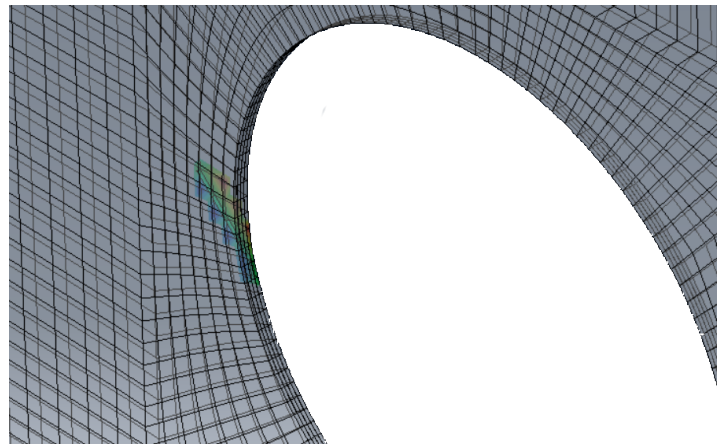


Figure 3.7: Crack on the 45° ply near the hole

A novel method for modelling multiple discontinuities within the framework of FE is mentioned in [18] and described by Chen et. al. in [20]. The floating node method (FNM), has been used successfully in modelling several challenging cases of tensile failure in composite laminates. A description of the particularities of the FNM is given in section 3.2. Among those is the capability of modelling widespread delamination and matrix cracks. Chen et. al. [21] demonstrated that the fracture mechanisms in a $[45_4/90_4/-45_4/0_4]_s$ laminate have been captured despite using a random, unstructured mesh. Figure 3.8 shows the damage extent predicted for an OHT simulation [21]. Similar to the OHT model of Chen et. al. [21], it is intended to simulate OHC problems using the FNM to model the matrix cracks. To the knowledge of the author this is the first time the FNM would be used for modelling OHC.

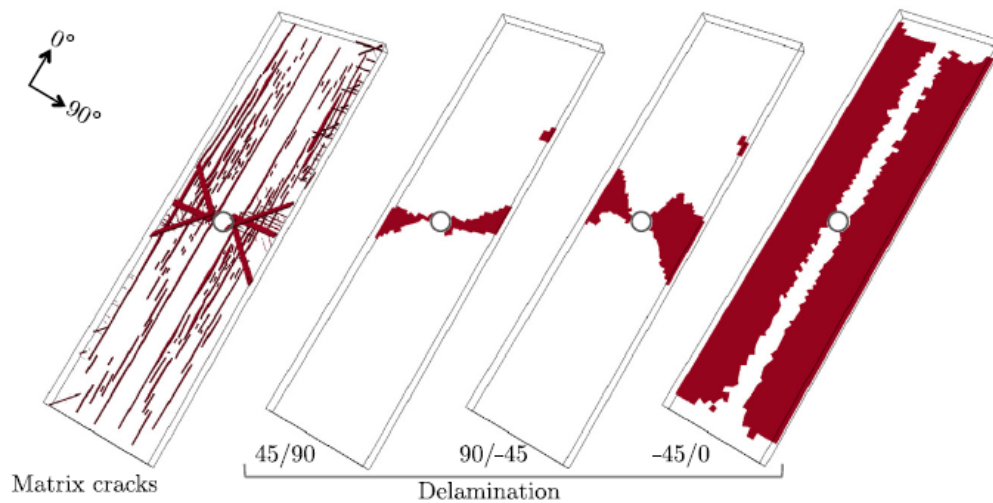


Figure 3.8: Extensive damage pattern predicted in an OHT problem using FNM [21]

3.2 The Floating Node Method

This chapter provides a concise description of the particularities of the Floating Node Model and how it is used to model composite OHC problems. Since the FNM has been previously used, all of its details as well as how it is implemented in Abaqus will not be focused on. For more information about the FNM, the reader is referred to [20] and [21].

3.2.1 Method Description

Just like XFEM, the FNM allows for explicit representation of discontinuities without relying on remeshing. This method is however different in computational architecture from XFEM. The latter, depicted in figure 3.9, works by changing the definition of the displacement approximation of an element, as explained previously. The FNM on the other hand, just like the PNM [3] [40], works by replacing a damaged element by multiple sub-elements. The main difference between the FNM and the PNM is that in the PNM the Jacobian of the transformation from physical to natural space and the vector of nodal coordinates remain the same as the element before it is partitioned. that the independent sub-element Jacobians (the transformation and the mapping of the new elements into a natural coordinate system) which uses only the Jacobian of the un-split element for the mapping. Chen et. al. [20] explains that in the PNM, because the active element formed with the phantom node is mapped into the natural coordinate system via the original transformation function, errors are introduced in the representation of its geometry.

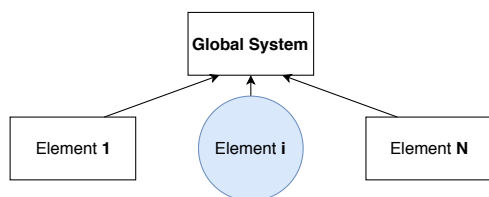


Figure 3.9: eXtended FEM computational architecture (reproduced from [20])

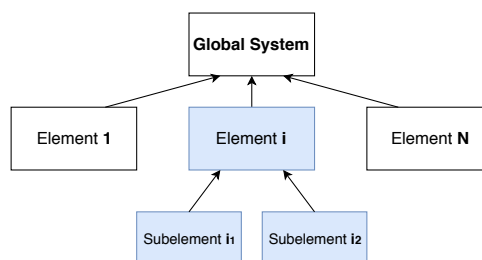


Figure 3.10: Floating Node Method computational architecture (reproduced from [20])

In the FNM, just like in standard FEM, each *real* node \mathbf{i} has its vector of nodal coordinates \mathbf{x}_i , and degree of freedom vector \mathbf{q}_i . In addition, in the FNM each element contains a number of extra DoF without any predefined nodal position, hence "floating". In the case of a simulation where no discontinuity is present, the problem is formulated identically with standard FEM (and XFEM). When a strong discontinuity occurs (eg. a matrix failure is initiated, see section 3.2.3), the intersection points of the crack and element edges, points \mathbf{X}_r and \mathbf{X}_s are determined. The map in figure 3.11 describes the vector of nodal coordinates, the Jacobian of the transformation, the DoF vector, the displacement approximation, the strain approximation, the stiffness matrix, the force vector and the equilibrium equation for an element in the FNM. In the depicted scenario, a quadrilateral element is split into two quadrilateral sub-elements, Ω_A and Ω_B . These two sub-elements will each get their own vector of nodal coordinates \mathbf{X}_{Ω_A} and \mathbf{X}_{Ω_B} as well as their own Jacobian transformation matrices \mathbf{J}_A and \mathbf{J}_B . The newly formed sub-elements behave then identically to a normal standard FE (eg. their individual stiffness matrices and force vectors have to satisfy the equilibrium relation: $\mathbf{K} \cdot \mathbf{q} = \mathbf{Q}$).

Figure 3.12 presents the ways in which a discontinuity can be represented with the FNM. From left to right, the initial element Ω may be split into:

- Two sub-elements Ω_A and Ω_B , each having their own floating DoF at the crack interface (for weak discontinuities).
- Two sub-elements Ω_A and Ω_B sharing the floating DoF at the interface (for strong discontinuities).
- Two sub-elements Ω_A and Ω_B and a cohesive surface Γ_{Ω_C} .

Weak and strong discontinuities are modeled the same essentially, the only difference is that fewer DoF are needed for the representation of a weak discontinuity (nodes can be shared between the sub-elements), as can be seen in figure 3.12. For the purpose of modeling matrix cracks however, a third approach is adopted. In this case the discontinuity representing the crack is modelled using a Cohesive Element. This scenario is depicted on the right side of figure 3.12 (for a simple case). Without the cohesive element, crack extension is assumed to take place when a fracture criterion, based on a critical stress or deformation near the crack tip is satisfied. But crack growth is also dependent on the measured fracture energy which cannot be

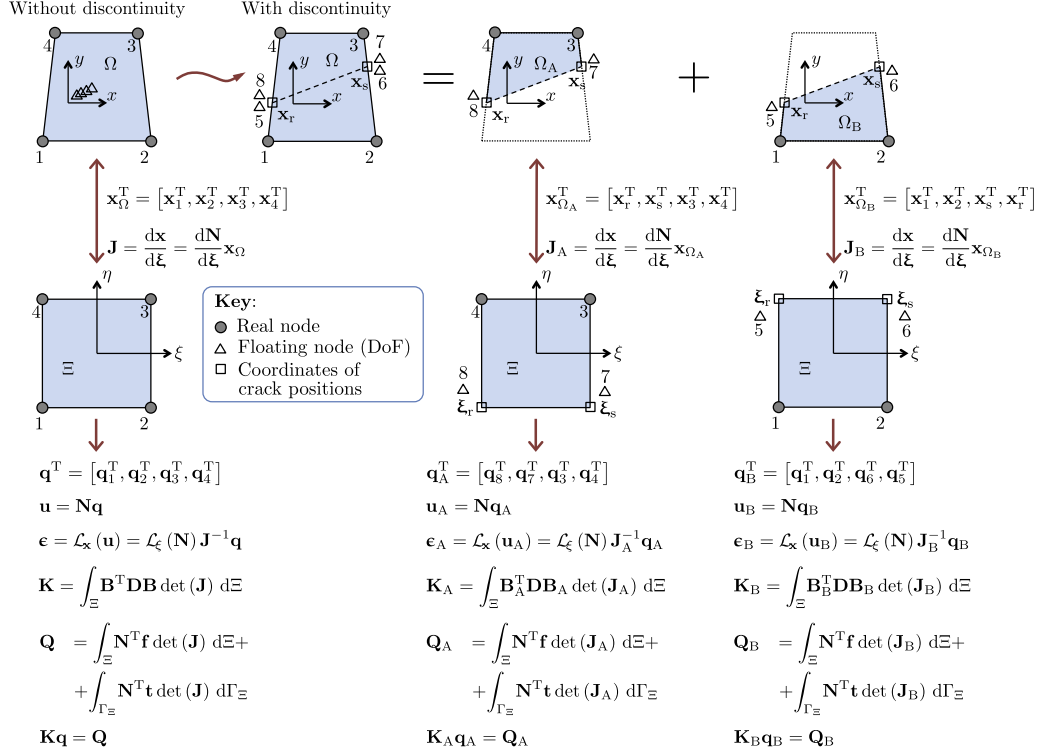


Figure 3.11: Element with a discontinuity in the Floating Node Method [20] (the element in the natural coordinate system is on the bottom)

incorporated. If a cohesive element is used, the response of the discontinuity interface can be described by a cohesive traction-separation law incorporating the effect of the fracture energy. When the cohesive element is used, the element equilibrium equation becomes different to that in equation (2.3). The new form is given in equation (3.5). Here $[[\bullet]]$ represents the jump of a function from one side to the other of the cohesive surface.

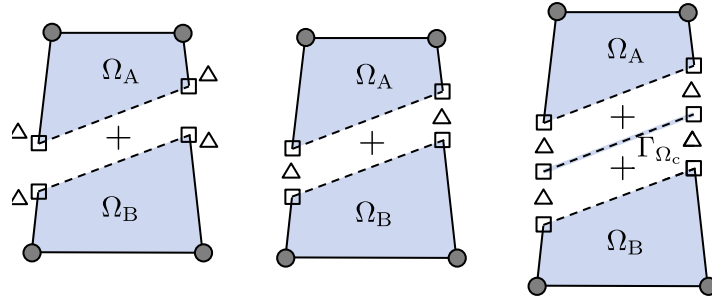


Figure 3.12: Different ways of modelling discontinuities [20]

$$\int_{\Omega} \boldsymbol{\epsilon}^T(\mathbf{v}) \boldsymbol{\sigma}(\mathbf{u}) d\Omega = \int_{\Omega_A} \boldsymbol{\epsilon}^T(\mathbf{v}) \boldsymbol{\sigma}(\mathbf{u}) d\Omega + \int_{\Omega_B} \boldsymbol{\epsilon}^T(\mathbf{v}) \boldsymbol{\sigma}(\mathbf{u}) d\Omega + \int_{\Gamma_{\Omega_c}} [[\mathbf{v}]] \boldsymbol{\tau}_c([[\mathbf{v}]]) d\Gamma_{\Omega_c} \quad (3.5)$$

The stiffness matrix of the cohesive element is calculated in a manner analogous to that of a sub-element, described by the map in figure 3.11. This time however, the shape of the element is described by the vector of nodal coordinates $\mathbf{x}_{\Gamma_c}^T = [x_r^T, x_s^T]$ and the Jacobian is $J_{CE} = \frac{d\mathbf{x}}{d\xi} = \frac{d\mathbf{N}_{CE}}{d\xi} \mathbf{x}_{\Gamma_{\Omega_c}}$. Since the traction $\boldsymbol{\tau}_c$ is related to the displacement jump via a relation $\boldsymbol{\tau}_c = \mathbf{D}_{CE} [[\mathbf{u}]]$, the stiffness matrix \mathbf{K}_{CE} can be reduced to equation (3.6). This stiffness matrix of the cohesive element is then assembled into the stiffness matrix of the entire element.

$$\mathbf{K}_{\text{CE}} = \int_{\Gamma_{\Xi_c}} [\mathbf{N}_{\text{CE}}, -\mathbf{N}_{\text{CE}}]^T \mathbf{D}_{\text{CE}} [\mathbf{N}_{\text{CE}}, -\mathbf{N}_{\text{CE}}] \mathbf{J}_{\text{CE}} d\Gamma_{\Xi_c} \quad (3.6)$$

3.2.2 Modelling of Composite Laminates

The partitioning of an element as explained above is not equivalent to the propagation of a matrix crack through that element. Different failure criteria are used for partitioning the FN element (which forms the CE) and failing the CE (cohesive law). Matrix cracks are simply represented by the cohesive elements generated at the sub-element interface (concept named Cohesive Zone Modeling). The cohesive zone is a couple of elements long and has the numerical crack tip at the edge of the cohesive zone in the direction where the crack extends. When a criterion for the propagation of cracks is satisfied the cohesive zone advances and the crack tip moves to the edge of the new element. A more in depth explanation of how matrix cracks propagate in the FNM is given in [21].

Criteria for predicting the onset of fiber and matrix failure need to be chosen. It is considered that fiber failure causes also matrix cracking, meaning that fiber failure is a sufficient requirement also for matrix failure. In the absence of fiber failure, matrix failure onset can of course be predicted independently using a dedicated failure criterion. Once either failure criteria is satisfied, the partitioning of the element is performed and a CE is placed in place of the crack. The CE will trigger the failure onset immediately while the damage evolution of this element will follow a specific cohesive law for its softening.

If fiber failure is detected first, it means that the softening behaviour of the sub-elements should reflect a fiber failure type of fracture. The softening behavior in this case is characterized by a damage variable d_f , $0 \leq d_f \leq 1$. The variable is used to define the new material properties (with [$'$]) in the following way:

$$\begin{aligned} E'_1 &= E_1(1 - d_f), \\ \nu'_{12} &= \nu_{12}(1 - d_f), \\ \nu'_{13} &= \nu_{13}(1 - d_f) \end{aligned}$$

If matrix failure were to happen first, it would happen for example when the normal and shear tractions on the matrix crack surface, τ_n, τ_t, τ_l , satisfy the matrix failure criteria. Unlike in the case of fiber failure, the softening associated with matrix cracking does not begin immediately, but only after the failure criteria in the cohesive element satisfied. Afterwards, the softening is done by degrading the material parameters at the integration points of the cohesive element (denoted by crosses \times in figure 3.13). The cohesive crack element will follow a softening curve represented by the damage variable d_m . This damage variable can be seen in equation (3.7), the relation between the traction and separation on the cohesive element. In this system of equations, the τ represent the tractions, the δ the separations and K the penalty stiffnesses. The newly modified (degraded) material parameters are updated at the cohesive element (Γ_{Ω_c}) integration points depicted in figure 3.13.

$$\begin{Bmatrix} \tau_n \\ \tau_t \\ \tau_l \end{Bmatrix} = \begin{bmatrix} K_n(1 - d_m) & 0 & 0 \\ 0 & K_t(1 - d_m) & 0 \\ 0 & 0 & K_l(1 - d_m) \end{bmatrix} \begin{Bmatrix} \delta_n \\ \delta_t \\ \delta_l \end{Bmatrix} \quad (3.7)$$

Finally, a great asset of the FNM that needs to be mentioned is that it allows for the sharing of information between the different plies and interfaces that belong to the same local (laminated) element. This represents a very powerful tool when modeling inter-ply interactions, for example matrix cracking - delamination interaction (depicted in figure 2.6).

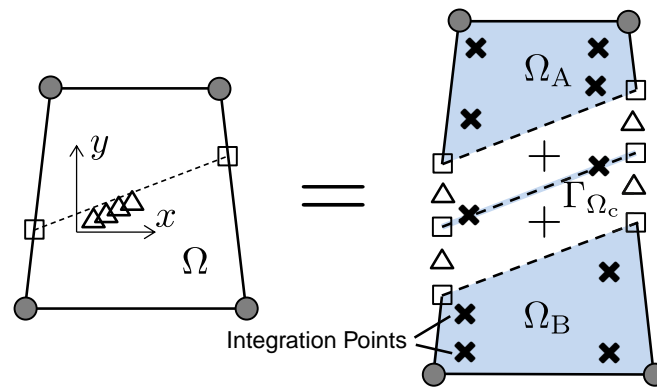


Figure 3.13: Integration points sub-elements (adapted from [21])

3.2.3 OHC simulation with the FNM

Using the same test setup as for the XFEM simulation done earlier in this chapter, the OHC problem is simulated using the FNM to demonstrate its capability (in dealing with crack-rich problems). To demonstrate the good convergence capabilities of the latter, an unstructured mesh, presented in figure 3.14, is used in the simulation. As explained earlier, fiber and matrix failure criteria are needed in order to split a FN element. Once an element is divided, as in figure 3.13, the softening behaviour of the newly created matrix crack will be governed by the cohesive law in the cohesive element (C.E.). Similarly, the softening behaviour of the sub-elements (eg. sub-elements Ω_A and Ω_B in fig 3.13) is governed by a cohesive law in these sub-elements, associated with fiber failure.

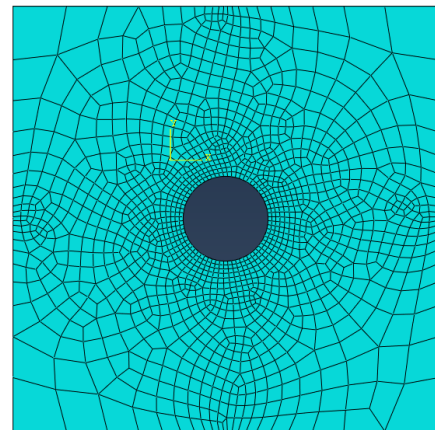


Figure 3.14: Panel with unstructured mesh used for the FNM simulation

Cohesive laws correlate the cohesive forces and displacement jumps along an interface in normal and tangential directions [32]. Mainly by virtue of their simplicity, bi-linear cohesive laws are the most popular. A large number of cohesive laws exist that are best suited for different applications (particle-matrix decohesion, solute segregation, crack growth in elasto-plastic material, peeling of adhesive joints, etc..). The crucial characteristic of cohesive laws is that they maintain a constant fracture energy dissipated for fully damaging a material point regardless of the element size or time increment used in that simulation. For this reason they are commonly adopted to ensure mesh objectivity. The failure criteria and softening behaviour characterizing the cohesive laws adopted here for fiber and matrix failure respectively will now be described.

Fiber Failure

It is assumed that the material behaves perfectly elastic up to the failure onset point. For this simulation, the Maximum Stress failure criterion is used to predict fiber failure onset. The material then reaches its maximum load carrying capability when the axial stress in the ply element is equal to the ply strength (X_t and X_c for tension and compression respectively). The criterion is given in equation (3.8).

$$\frac{\max(\sigma_{11}, 0)}{X_t} + \frac{\min(\sigma_{11}, 0)}{X_c} > 1 \text{ (for failure onset)} \quad (3.8)$$

After failure onset the material starts to soften. This part of the curve is calculated such that the fracture toughness requirement, given in equation (3.10), is satisfied. In this equation u_1 is the vertical displacement and

u_{1f} is the vertical displacement at complete failure. In other words, the area under the traction separation curve is equal to the ply fracture toughness, as in figure 5.7. In order to account for a kind of thickness size effects (ply scaling), the cohesive law that governs the ply element response is scaled as in equation (3.9). That is, the fracture toughness for a block of n plies is n times larger than that of an individual ply. This is based on the experimental observations of [59]. It should be mentioned however that the fracture toughness that will be used (given in table A.2) is the compression fracture toughness of the laminate which may contain energy dissipated also through matrix cracking, delamination, etc.. not specifically the energy dissipated by the fiber kinking mechanism in a ply. It is expected however that the energy dissipated through kinking/micro buckling is dominant [71].

$$G_{fc}^n = n \times G_{fc}^1 \quad (3.9) \quad \int_0^{u_{1f}} \sigma_1 du_1 = G_{fc}^n \quad (3.10)$$

Matrix failure

Matrix failure is predicted using a quadratic failure criteria. Since the C.E. is supposed to have its damage onset at the same time when the element is split, the matrix failure criteria described here applies both to un-split elements and the C.E. The criteria for tension and compression loads are differentiated. The failure index for tension, f_{index_t} , and for compression, f_{index_c} , are given in equation (3.11) and equation (3.12) respectively. The tractions τ_N , τ_L and τ_T are the stresses along a potential fracture angle α that maximizes the failure index. They are calculated using equation (3.13) and the maximizing angle is determined iteratively. The terms Y_t , S_t and S_L are ply properties. Finally, the terms η_L and η_T are traverse and longitudinal frictional parameters. They can be estimated using equation (3.14) and (3.15) from Pinho et. al. [62] provided the angle ϕ_0 of the fracture plane for a purely compressive load. This typical value of this angle is given in equation (3.16). The tensile criterion (equation (3.11)) is used if the normal traction on the potential fracture surface τ_n is positive, while the compression criterion is used only if the same traction is negative.

$$f_{index_t} = \sqrt{\left(\frac{\tau_N}{Y_t}\right)^2 + \left(\frac{\tau_L}{S_L}\right)^2 + \left(\frac{\tau_T}{S_T}\right)^2} \quad (3.11)$$

$$f_{index_c} = \sqrt{\left(\frac{\tau_L}{S_L - \eta_L \cdot \tau_n}\right)^2 + \left(\frac{\tau_T}{S_t - \eta_T \cdot \tau_N}\right)^2} \quad (3.12)$$

$$\begin{aligned} \tau_N &= \cos^2(\alpha)\sigma_{22} + 2\cos(\alpha)\sin(\alpha)\tau_{23} + \sin^2(\alpha)\sigma_{33} \\ \tau_T &= -\sin(\alpha)\cos(\alpha)(\sigma_{22} - \sigma_{33}) + (\cos^2(\alpha) - \sin^2(\alpha))\tau_{23} \\ \tau_L &= \cos(\alpha)\tau_{12} + \sin(\alpha)\tau_{13} \end{aligned} \quad (3.13)$$

$$\eta_T = -\frac{1}{\tan(2\phi_0)} \quad (3.14) \quad \eta_L = \frac{S_L}{S_T}\eta_T \quad (3.15) \quad \phi_0 \approx 53^\circ \pm 2^\circ \quad (3.16)$$

3.2.4 Discussion of results

Unlike the simulation performed with XFEM, presented in section 3.1, which could not converge past an incipient state of failure, when the FNM is used no convergence issue is encountered in the analysis until it is manually stopped at an applied displacement of $u_1 = -0.5$ mm. These results will be used as a reference in the assessment of the kinking constitutive law proposed in Chapter 4.

The stress - displacement curve of the laminate is presented in figure 3.15. The estimated panel strength is $\sigma \approx -430$ MPa. This result is approximately 15% larger than the experimental average stress of 373 MPa presented in table A.1. Unfortunately, the author [46] only provides the obtained panel strengths not allowing for a more detailed comparison. The first significant event that can be seen in the simulation as the load progresses is the onset of fiber damage on the 0° ply right near the hole (formation of the damage zone discussed in Chapter 2).

The displacement and far-field stress at this event can be seen $\sigma_{11} - u_1$ curve and is depicted in figure 3.16. Shortly after that, delamination occurs at the [-45/0] interface near the hole as depicted in figure 3.17, artifact predicted also by the XFEM model (which also predicted high loads at the panel edges). This damage zone, represented before in figure 2.1, increased in size without any noticeable effect on the panel stiffness until $u_1 \approx -0.25$ mm when a sudden decrease in stiffness occurs. After a short softening region the stress recovers until the strength of the panel is reached. At this moment in time, the fiber damage has propagated away from the hole as can be seen in figure 3.18. Finally, the fully propagated fiber damage pattern, occurring in the post failure state, is displayed in figure 3.19.

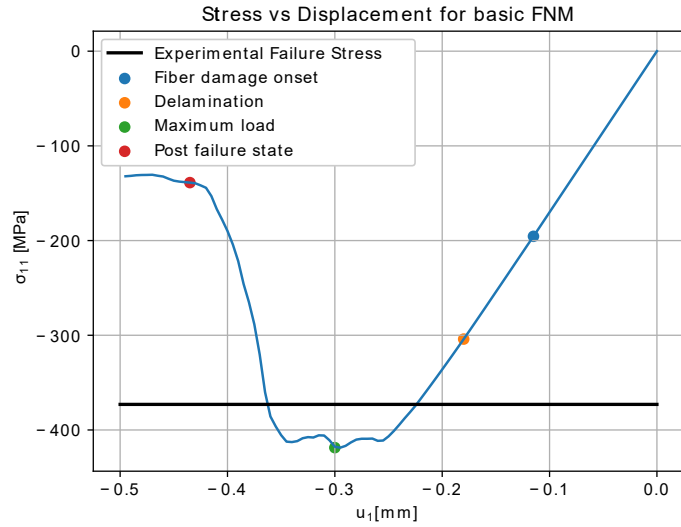


Figure 3.15: Stress - Displacement curve of the FNM based simulation with Maximum Stress criterion governing the fiber failure onset

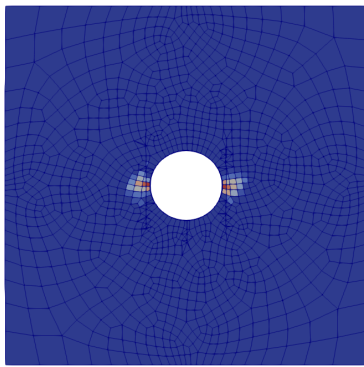


Figure 3.16: Fiber damage initiation near hole

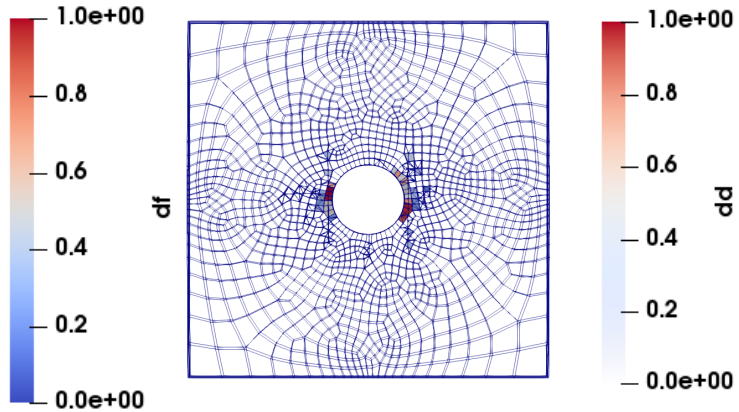


Figure 3.17: Delamination initiation near the hole

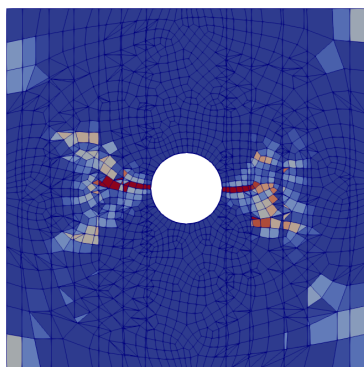


Figure 3.18: Fiber damage state at maximum load

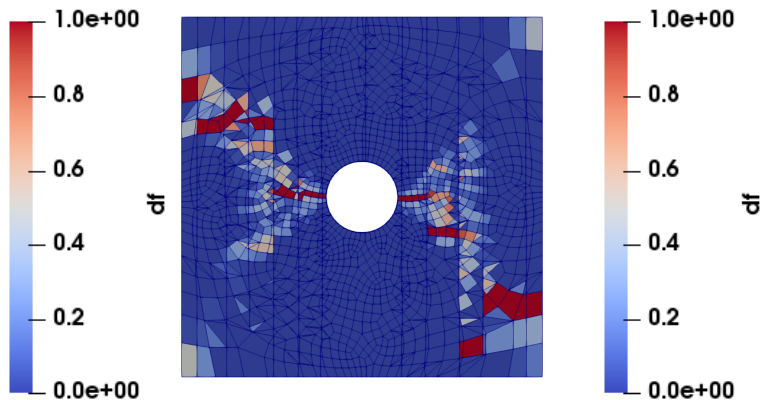


Figure 3.19: Fiber damage in post failure state

A summary of the main events that occurred during the analysis and the pictures describing them can be found in table 3.1. The full set of results obtained from this simulation can be found in Appendix B. The results of this simulation will serve as a reference in order to assess the performance of the compression constitutive law proposed in chapter 4.

Table 3.1: Critical points on the Force - Displacement diagram of the FNM based OHC simulation with the Maximum Stress failure criteria

Location	Figure	Displacement [mm]	Stress [MPa]	Note
•	Fig 3.16	-0.115	-195	Fiber damage onset
•	Fig 3.17	-0.18	-306	Delamination at 0/45 interface
•	Fig 3.18	-0.3	-429	Maximum stress
•	Fig 3.19	-0.435	-138	Post failure state

4

Modelling of longitudinal compression in composites

The investigation in Chapter 2 identifies the need for a more accurate and physically based CDM representing the failure mechanisms of fibers under compression in the Progressive Damage Analyses based on the FNM. Researchers like Andrew C. et. al. [7] support the idea that the insufficient physical basis of the current PDA is one of the main factors for their poor accuracy when modelling compressive tests. Recent studies have shown that the dominant in plane failure mechanism governing composite longitudinal compression is fiber kinking [64]. In the last decade, some new constitutive laws have been proposed for modelling longitudinal compression that consider fiber kinking as the mechanism governing the failure [1] [65] [63] [37] [38] [7].

4.1 Background

Generally, axially loaded FRP plies show a linear elastic behaviour up to failure. If the stiffness is known, the first important aspect of a compressive meso-scale model is a failure trigger function which separates the undamaged and damaged state of the material in the ply. An abundance of stress-strain based criteria exist for damage initiation having different levels of physical background. To ensure however that the current work is of actuality, only those that are more recent are investigated in this chapter to be used in the OHC simulation. To the knowledge of the author, these are: the three models of Gutkin et. al. [37], [38] and [50]; the DGD based model of Bergan et. al. [7]; two models of Pinho et. al. [63] and [65]; and the model of Cantalanotti et. al. [16].

Gutkin et. al. [37] proposed a model to predict fiber kinking and splitting in FRP under combined longitudinal compression and in plane shear. His work is based on the hypothesis that the strength associated with fiber kinking is reached when the strain energy released per unit area of crack generated (between an undamaged and a damaged state) is equal to the energy required to create a unit area of cracks (fracture energy). In depth investigation of the method reveals the need of an undetermined parameter α . The latter should account for the characteristics of the microcracks in the system, but in the absence of a more clear definition of this term and how it can be measured, this approach cannot be used in the current work. In another works, Gutkin et. al. [38] (and [36] and [9], all three are needed for a complete understanding) proposes a method that models kink-band growth and longitudinal crushing of composites under a three dimensional stress state, while accounting for frictional stresses at microcrack closure. A great advantage of this method is that, at concept level, the approach is simple and logical. The kinking response is estimated by solving simultaneously: 1) the stress equilibrium between applied global stresses and nonlinear local stresses; 2) the nonlinear constitutive law of the material contained in the kink band; 3) the strain compatibility equations. While in this work the parameter α mentioned earlier is no longer needed, the method cannot be considered for the current work. Using this method in a simulation, many non-trivial experimental parameters were needed which could not be determined accurately. For example, one requires knowledge of a shape parameter p that is found experimentally from cyclic shear tests. Furthermore, friction coefficients (μ_L, μ_T) and the internal pressures p_{0T}

and p_{0L} caused during manufacturing also need to be known. Finally, for the last of the mentioned methods of Gutkin et. al. [50] the same problem was encountered. This method makes use of the parameters β^f , β^g , and β^h which are material properties representative of the degradation of the matrix shear, fiber crushing and longitudinal fiber shear response respectively. Since an explanation on how to obtain them is missing the method cannot be used.

The next method, proposed by Bergan et. al. [7], adopts a Deformation Gradient Decomposition (DGD) technique to represent kink bands as displacement jumps in cohesive interfaces. An asset of this model is that it can objectively represent the matrix failures that occur in the misalignment frame. Another advantage is that it has already been implemented as VUMAT in Abaqus and is available online [54]. But much like the methods proposed earlier, this model requires as input non-trivial experimental data i.e.: the constants α and η (representing material properties that define the shear stress-strain curve); the constant c_l (a non-linearity coefficient), etc.. The model is also expected to have a high computational cost due to the iterative processes which it makes use of [7].

Relying on Argon's ¹ hypothesis [4], Dávila et. al. [17] used it in combination with the LaRC02/03 matrix failure criteria and proposed a 2D kinking model. The latter assumes that the fibers in a laminate are initially misaligned and, as the load increases, the misalignment angle increases. The stresses in the misalignment frame are computed and substituted in a matrix failure criterion. Different matrix failure criteria are used depending on the sign of the normal stress in the fracture plane τ_n . Pinho et. al. [63] extended the model of Dávila to three dimensions and adopted a modified matrix compression failure criterion, proposed by Puck and Schürmann [2], arguing that it is better suited for 3D applications (for matrix tensile failure a simple quadratic interaction criteria was used as it was deemed the most accurate). In the opinion of the author, Pinho's approach is very attractive for modelling by virtue of its physical basis and ease of applicability. However, a limitation should be addressed to improve the method. In the proposed model no differentiation is made between the fiber kinking and fiber splitting failure modes. The latter, being essentially a continuous and long line of matrix failure, is generally found in composite plies subjected to large shear stresses [58] and does not localize in a kink band [37]. The two phenomena mentioned are distinct and using Pinho's approach may lead to fiber kinking onset in false situations. In a later publication [65], the same author completes the model addressing this issue. It is added that fiber kinking should occur if the local axial compressive stress σ_{11} is larger in magnitude than $X_c/2$, criterion based on experimental observations. However, no underlying physical mechanism is described that may lead to this observation. Just like in the method of Whiney and Nuisemer [77] discussed in chapter 2, this criterion may hold only for the laminates where the observation was made. In the absence of a physically-based criterion to distinguish fiber kinking from fiber splitting, the prediction of fiber kinking should be adopted with care.

Other updates on Pinho's model [63] were made by both Pinho [65] and Cantalanotti [16]. The new approaches both account for *in situ* effects (increase of a ply shear strength when used in a multi-directional laminate). These will however not be adopted as the procedure used to determine the *in situ* strengths is based on a fracture mechanics analysis of an idealized crack in a unidirectional ply, method proposed by Dvorak and Laws [26]. The derivation of the *in situ* strengths is based on Linear Elastic Fracture Mechanics (LEFM) [61]. This is an alternative method to the already employed Cohesive Zone Modelling (CZM) used for crack propagation by the FNM. Using a LEFM based term would represent an inconsistency of the simulation framework proposed for OHC.

In conclusion, Pinho's approach [63] to model fiber kinking is physically based and easy to implement but has a limitation in distinguishing between fiber kinking and fiber splitting. An improved model for fiber kinking will now be proposed, build on top of Pinho's [63] original model.

4.2 Proposed constitutive law

The next section will detail how Pinho's kinking initiation works and how will it be supplemented by the proposed improvements. After that, in sections 4.2.2 and 4.2.3 the proposed constitutive law for softening is discussed.

¹Kink bands are triggered by localized matrix failure in the vicinity of misaligned fibers. This is due to the loss of support that the matrix would otherwise provide to the fibers.

4.2.1 Failure Onset

Pinho [63] considered, like Argon [4] proposed, that fiber kinking is initiated when the matrix around the kinked fibers fails. In addition to this condition, two additional requirements are proposed to assure that the undergoing failure mechanism can indeed be associated with fiber kinking and not another failure mode (such as fiber splitting).

For fiber kinking to occur, the matrix around the kinking fibers needs to have failed.

The first part of the criteria requires for kinking onset that the tractions on the fracture plane $t_N^{(\varphi)}$, $t_L^{(\varphi)}$ and $t_T^{(\varphi)}$, given in equation 4.1, cause the matrix failure index ϕ_{KM} (in equation (4.2)) to exceed 1. The fracture plane is the plane in the misalignment frame where the tractions mentioned maximize the failure index ϕ_{KM} . The fracture plane depicted in figure 4.1 (c) and one can see that it is determined by the angle α .

$$\begin{aligned} t_N^{(\varphi)} &= \cos^2(\alpha)\sigma_{22}^{(\varphi)} + 2\cos(\alpha)\sin(\alpha)\tau_{23}^{(\varphi)} + \sin^2(\alpha)\sigma_{33}^{(\varphi)} \\ t_T^{(\varphi)} &= -\sin(\alpha)\cos(\alpha)(\sigma_{22}^{(\varphi)} - \sigma_{33}^{(\varphi)}) + (\cos^2(\alpha) - \sin^2(\alpha))\tau_{23}^{(\varphi)} \\ t_L^{(\varphi)} &= \cos(\alpha)\tau_{12}^{(\varphi)} + \sin(\alpha)\tau_{13} \end{aligned} \quad (4.1)$$

The fracture plane where the failure criteria are applied is not known apriori. Angles θ , φ and α need to be determined such that the components of the traction vector in equation (4.1) are determined after making the necessary stress transformations. In a standard FE simulation, the stresses available at integration point level are the standard stresses acting on the (1-2-3) coordinate system depicted in figure 4.1(a): σ_{11} , σ_{22} , σ_{33} , τ_{12} , τ_{13} and τ_{23} . As it will be explained later in this section, two successive stress transformations need to be performed before the tractions acting on the fracture plane can be determined.

Depending on the sign of the normal traction component $t_N^{(\varphi)}$, a matrix failure criteria specific to tension (Quadratic Stress criterion) or to compression (Puck criterion [2]) is used to deem matrix failure. These are given in equations (4.3) and (4.4) respectively.

$$\phi_{KM} = \begin{cases} \phi_{KMT}, & \text{if } t_N^{(\varphi)} > 0 \\ \phi_{KMC}, & \text{if } t_N^{(\varphi)} < 0 \end{cases} \quad (4.2)$$

$$\phi_{KMT} = \left(\frac{t_N^{(\varphi)}}{Y_T} \right)^2 + \left(\frac{t_L^{(\varphi)}}{S_L} \right)^2 + \left(\frac{t_T^{(\varphi)}}{S_T} \right)^2 \quad (4.3)$$

$$\phi_{KMC} = \left(\frac{t_L^{(\varphi)}}{S_L - \eta_L t_N^{(\varphi)}} \right)^2 + \left(\frac{t_T^{(\varphi)}}{S_T - \eta_T t_N^{(\varphi)}} \right)^2 \quad (4.4)$$

The terms S_L , S_T and Y_T are known ply material strength properties presented in table A.2 for the IM7/8552 material system used throughout this report. Furthermore η_L and η_T represent the longitudinal and traverse angle of internal shear, friction like parameters that can be obtained from a 15° off-axis compression test. Pinho [63] however provides an estimation method for η_L and η_T given in equations (4.5) and (4.6), avoiding thus the need for any test. The only parameters that need to be known in the last two equations are actually exactly the ply shear strengths S_L , S_T and the fracture plane angle for pure compression ϕ_0 (typically $\phi_0 \approx 53^\circ$).

$$\eta_L = S_L \frac{\eta_T}{S_T} \quad (4.5)$$

$$\eta_T = -\frac{1}{\tan(2\phi_0)} \quad (4.6)$$

The stress matrix σ in equation (4.7) represents the loading on a material point in the (1-2-3) coordinate system. It is formed using the known stresses σ_{11} , σ_{22} , σ_{33} , τ_{12} , τ_{13} and τ_{23} acting at that point.

$$\sigma = \begin{bmatrix} \sigma_{11} & \tau_{12} & \tau_{13} \\ \tau_{12} & \sigma_{22} & \tau_{23} \\ \tau_{13} & \tau_{23} & \sigma_{33} \end{bmatrix} \quad (4.7)$$

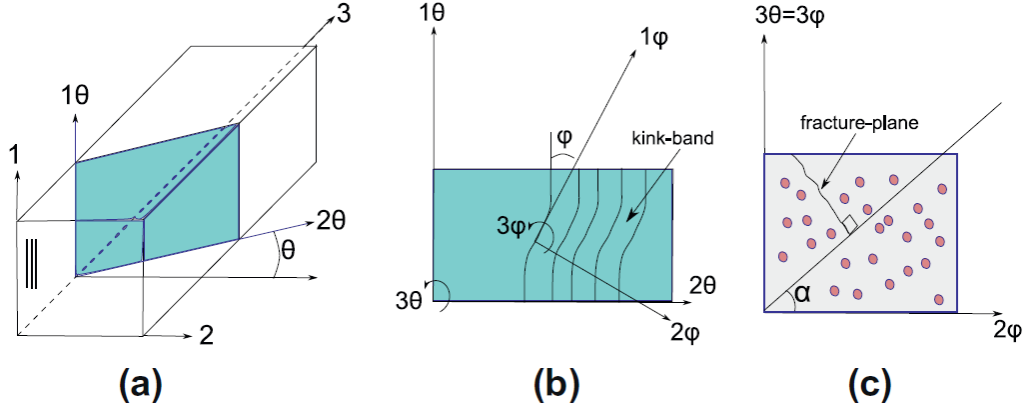


Figure 4.1: Transformation planes [16]

Following the depictions in figure 4.1, the first necessary stress transformation turns stresses from the material coordinate system into the kinking plane, from σ to $\sigma^{(\theta)}$, over the angle θ . This is done using relation (4.8). Since the rotation is done around the vertical axis 1 (in the fiber direction), the rotation matrix $\mathbf{R}^{(\theta)}$ is given by equation (4.9).

$$\sigma^{(\theta)} = \mathbf{R}^{(\theta)} \cdot \sigma \cdot \mathbf{R}^{(\theta)T} \quad (4.8) \quad \mathbf{R}^{(\theta)} = \begin{bmatrix} 1 & 0 & 0 \\ 0 & \cos(\theta) & \sin(\theta) \\ 0 & -\sin(\theta) & \cos(\theta) \end{bmatrix} \quad (4.9)$$

The angle θ is the angle that will eventually maximize the failure index ϕ_{KM} for a given set of stresses σ . Some estimation methods for the rotation angle θ exist [16], but the most accurate way is to follow an iterative approach and manually search for the optimal value.

The second transformation, from $\sigma^{(\theta)}$ to $\sigma^{(\varphi)}$ (from the kinking plane to the kink band angle), is done by rotating via the angle φ around the third axis of the kinking plane (3θ). The transformation is done using equation (4.10) where the transformation matrix $\mathbf{R}^{(\varphi)}$ is given in equation (4.11). Determining the misalignment angle φ is less straightforward than θ and requires a bit of explanation. The method for its finding was first proposed by Dávila et al. [17].

$$\sigma^{(\varphi)} = \mathbf{R}^{(\varphi)} \cdot \sigma \cdot \mathbf{R}^{(\varphi)T} \quad (4.10) \quad \mathbf{R}^{(\varphi)} = \begin{bmatrix} \cos(\varphi) & \sin(\varphi) & 0 \\ -\sin(\varphi) & \cos(\varphi) & 0 \\ 0 & 0 & 1 \end{bmatrix} \quad (4.11)$$

The total misalignment angle is defined as the sum of an initial misalignment angle φ_0 and an angle γ_m that varies with the shear loading. This is written in equation (4.12).

$$\varphi = \text{sgn}(\tau_{12})(\varphi_0 + \gamma_m) \quad (4.12)$$

For the initial misalignment fiber, consider in a 2D problem a misalignment coordinate frame denoted with the superscript (m), as depicted in figure 4.2. The stresses in this coordinate frame can be estimated as in equation (4.13). Under a purely axial compression load, the failure is expected to occur when $\sigma_{11} = -X_c, \sigma_{22} = \tau_{12} = 0$.

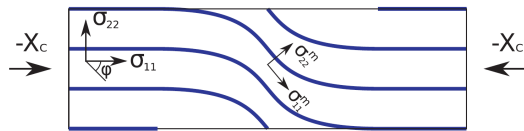


Figure 4.2: Stresses in a 2D misalignment frame [16]

$$\begin{aligned} \sigma_{11}^{(m)} &= \cos^2(\varphi)\sigma_{11} + \sin^2(\varphi)\sigma_{22} + 2\sin(\varphi)\cos(\varphi)|\tau_{12}| \\ \sigma_{22}^{(m)} &= \sin^2(\varphi)\sigma_{11} + \cos^2(\varphi)\sigma_{22} - 2\sin(\varphi)\cos(\varphi)|\tau_{12}| \\ \tau_{12}^{(m)} &= \sin(\varphi)\cos(\varphi)(\sigma_{22} - \sigma_{11}) + (\cos^2(\varphi) - \sin^2(\varphi))|\tau_{12}| \end{aligned} \quad (4.13)$$

Under such a loading, equation (4.13) can be rewritten as equation (4.14), where φ_c represents the misalignment angle at failure.

$$\begin{aligned}
\sigma_{11}^{(m)} &= -\cos^2(\varphi_c) X_c \\
\sigma_{22}^{(m)} &= -\sin^2(\varphi_c) X_c \\
\tau_{12}^{(m)} &= \sin(\varphi_c) \cos(\varphi_c) X_c
\end{aligned} \tag{4.14}$$

Substituting these stresses in the LaRC03 [17] failure criterion for matrix failure (shown in equation (4.15)) and rearranging, equation (4.16) for φ_c is obtained.

$$S_L = X_c(\sin(\varphi_c) \cos(\varphi_c) - \eta_L \sin^2(\varphi_c)) \quad (4.15) \quad \varphi_c = \arctan \left(\frac{1 - \sqrt{1 - 4 \left(\frac{S_L}{X_c} + \eta_L \right) \frac{S_L}{X_c}}}{2 \left(\frac{S_L}{X_c} + \eta_L \right)} \right) \tag{4.16}$$

Considering again only an axial compression being applied and assuming the material exhibits a linear behaviour up to failure, the shear strain at failure γ_{mC} can be written as relation (4.17).

$$\gamma_{mC} = \frac{\sin(2\varphi_c) X_c}{2G_{12}} \approx \frac{\varphi_c X_c}{G_{12}} \tag{4.17}$$

The initial misalignment angle can now be determined by replacing equations (4.16) and (4.17) into equation (4.18).

$$\varphi_0 = \varphi_c - \gamma_{mC} \tag{4.18}$$

With the initial misalignment fiber determined, only the shear strain γ_m is still needed for finding the total misalignment fiber φ . This is done considering a generic load (not exclusively axial compression) applied. The strain γ_m can be found by solving equation (4.19). If small angle approximation is assumed, equation (4.19) can be rearranged to the form in equation (4.20). In the latter, Pinho et al. [63] suggested using the stresses in the kinking plane $\sigma_{11}^{(\theta)}, \sigma_{22}^{(\theta)}, \tau_{12}^{(\theta)}$ instead of $\sigma_{11}, \sigma_{22}, \tau_{12}$

$$f(\gamma_m) = -\sin(\varphi) \cos(\varphi) (\sigma_{11} - \sigma_{22}) + (\cos^2(\varphi) - \sin^2(\varphi)) |\tau_{12}| \tag{4.19}$$

$$\gamma_m = \frac{\varphi_0 G_{12} + |\tau_{12}|}{G_{12} + \sigma_{11} - \sigma_{22}} - \varphi_0 \tag{4.20}$$

The misalignment angle φ can now be determined by replacing φ_0 and γ_m into equation (4.12) and following the stress transformation in equation (4.10) the stress matrix $\sigma^{(\varphi)}$ is found.

The last angle to be found before the tractions on the fracture plane $t_N^{(\varphi)}, t_L^{(\varphi)}$ and $t_T^{(\varphi)}$ can be determined is α . The latter is needed to transform the stresses $\sigma^{(\varphi)}$ from the misalignment fiber frame (φ) in figure 4.1(b) to the fracture plane in figure 4.1(c). Similar to the determination of the kink plane angle θ , no specific procedure is used for determining the fracture angle α . An iterative approach will be again employed. Therefore, the angles θ and α are those which together maximize the value of the failure index ϕ_{KM} . The traction components in the misalignment frame are found applying equation (4.1) and the matrix fails if $\phi_{KM} > 1$, thus satisfying Argon's hypothesis and the first requirement in the here-proposed kinking onset criterion.

The second part of the failure criterion (which represents an addition to the work of Pinho [63]) is here presented. To reduce computational expense, this requirement will only be checked after the former has been satisfied.

A micrograph of the kink band in a T300/913 specimen is presented in figure 4.3 and another of a IM-7-12K/411-C50 specimen in figure 4.4. The following observation may be made: possibly helped by the matrix cracks formed in the region of the kink band, fibers in the presented images have bent to a point where, due to the bending stresses, they broke at one end of the kink band and then at the other. The following kinking requirement may be proposed based on the observation made:

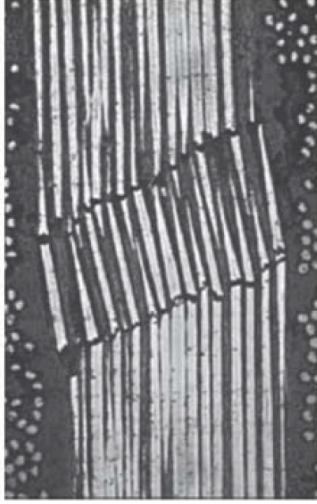


Figure 4.3: Kink band failed T300 fibers [56]

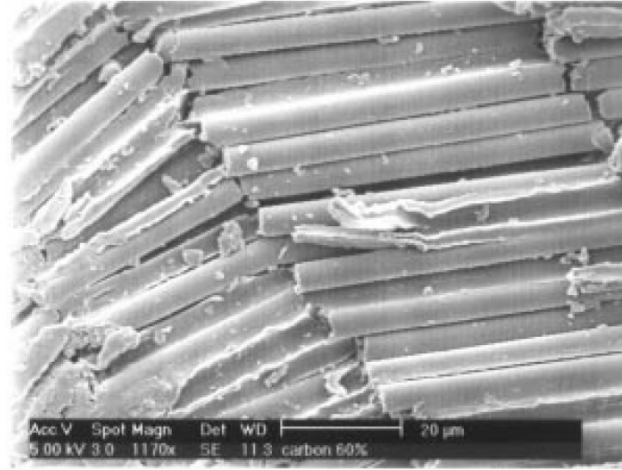


Figure 4.4: Kink band failed IM7-12K fibers [52]

For fiber kinking to occur, the maximum bending stress in a fiber should be large enough to break it

$$|\sigma_{b_{max}}| > \sigma_{fib_{max}}.$$

To explain how the second requirement works consider the kinking plane in figure 4.1(b) which is extracted here for convenience and placed on the left side figure 4.5. The kinking plane is acted upon by the stresses $\sigma_{11}^{(\theta)}$, $\sigma_{22}^{(\theta)}$ and $\tau_{12}^{(\theta)}$ from $\sigma^{(\theta)}$ (obtained previously from equation (4.8)). If an individual fiber is to be examined, as on the right side of figure 4.5, one can see that it is acted upon by the same longitudinal normal stress $\sigma_{11}^{(\theta)}$ (which is in fact always equal to σ_{11}). The other stresses in the kinking plane, $\sigma_{22}^{(\theta)}$ and $\tau_{12}^{(\theta)}$, are indirectly acting on the fiber by influencing the misalignment angle φ .

Due to the angle φ , an offset w_{MA} exists between vertical forces acting on the fiber (follow figure 4.5). It can be written as $w_{MA} = w_{kink} \cdot \sin \varphi$ where φ is known and w_{kink} is the kink band width. A plethora of experimental data suggests that the kink band width is between 10 to 20 times the fiber diameter w_{kink} [10] [29][35]. It will be assumed here that the kink band width is the averaged $w_{kink} = 15d_{fib}$. The moment created by the stresses can be calculated as in equation (4.21). In this equation d_{fib} represents the diameter of a single fiber, a material parameter always provided by the manufacturer.

$$M = F \cdot w_{MA} = \sigma_{11} A_{fib} w_{kink} \cdot \sin \varphi = \sigma_{11} \frac{d_{fib}^2 \cdot \pi}{4} \cdot 15d_{fib} \cdot \sin \varphi = \frac{15}{4} \sigma_{11} d_{fib}^3 \pi \cdot \sin \varphi \quad (4.21)$$

Due to this moment, a bending stress $\sigma_b(y)$ is expected to arise in the fiber as depicted in figure 4.5. Assuming the fiber can be modelled according to Euler-Bernoulli beam theory, the maximum bending stress $\sigma_{b_{max}}$ is at a distance $y = d_{fib}/2$ from the neutral axis. The expression for the absolute value for the maximum bending stress in the fiber is given in equation (4.22). The term I_{fib} represents the area moment of inertia of a single fiber. Since the fiber is expected to have a circular cross section with uniform material distribution, the I_{fib} can be calculated with equation (4.23).

$$|\sigma_{b_{max}}| = \frac{M \cdot y}{I_{fib}} = \frac{M \cdot d_{fib}}{2I_{fib}} = 120|\sigma_{11} \cdot \sin \varphi| \quad (4.22) \quad I_{fib} = \frac{\pi \cdot d_{fib}^4}{64} \quad (4.23)$$

Remembering the hypothesis of the second requirement: for kinking to onset, the fiber must break under the bending stress. This can now be written as in equation (4.24). The only extra data needed for this criterion is therefore the fiber strength $\sigma_{fib_{max}}$, always supplied by the manufacturer.

$$|\sigma_{b_{max}}| > \sigma_{fib_{max}} \equiv 120|\sigma_{11}| \cdot |\sin \varphi| > \sigma_{fib_{max}} \quad (4.24)$$

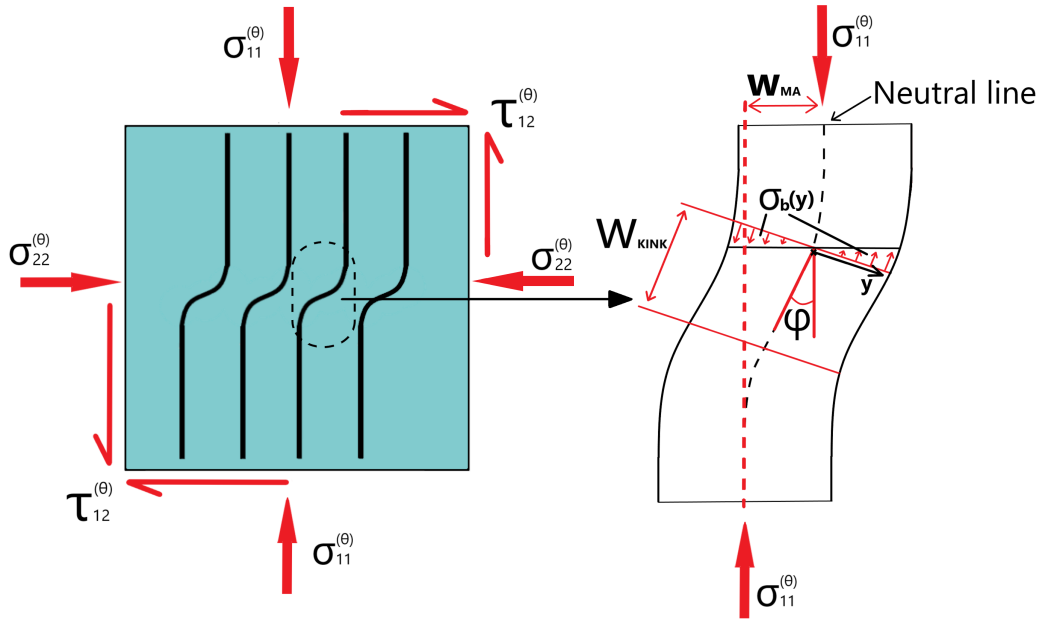
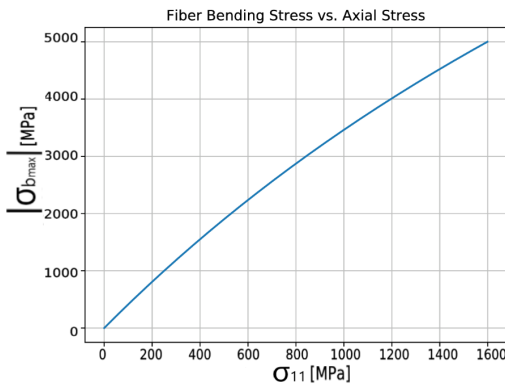
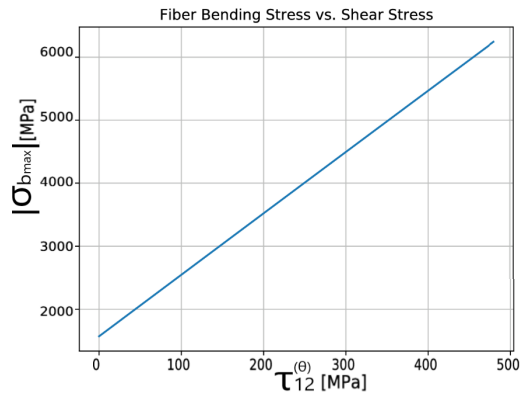


Figure 4.5: Kinking plane and with fiber bending stresses depicted

Equation (4.22) for $|\sigma_{b_{max}}|$ can be expanded using equations (4.12), (4.20) and (4.24) to obtain the relation presented in equation (4.25). Examining the latter shows that $|\sigma_{b_{max}}|$ increases with $\tau_{12}^{(\theta)}$ and with σ_{11} (since the latter is less straightforward, it was plotted for proof in figure 4.6 for generic values of σ_{22} and τ_{12}).

$$|\sigma_{b_{max}}| = 120 \cdot \left| \sigma_{11} \cdot \sin \left(\frac{\varphi_0 G_{12} + |\tau_{12}^{(\theta)}|}{G_{12} + \sigma_{11} - \sigma_{22}^{(\theta)}} \right) \right| \quad (4.25)$$

Figure 4.6: For $\sigma_{22} = 200$ MPa, $\tau_{12} = 0$ and $\varphi_0 = 2^\circ$ Figure 4.7: For $\sigma_{22} = 50$ MPa, $\sigma_{11} = 400$ MPa and $\varphi_0 = 2^\circ$

The fact that $|\sigma_{b_{max}}|$ increases with $\tau_{12}^{(\theta)}$ is what sparks the need for the next and final kinking criterion. Analysis of the graph in figure 4.7 shows that $|\sigma_{b_{max}}|$ can attain relatively large values for relatively low σ_{11} , provided $\tau_{12}^{(\theta)}$ is sufficiently large. For example, consider the IM7 fiber used so far in this report, it has a strength of $\sigma_{fib_{max}} = 5516$ MPa [22], meaning that under the conditions of figure 4.7 the second requirement for fiber kinking would be satisfied despite the axial stress σ_{11} being only 400 MPa in magnitude. Of course the $\tau_{12}^{(\theta)}$ values in figure 4.7 are quite large, larger than a typical ply shear strength S_t . To prevent kinking from occurring in these shear dominated scenarios, the obvious solution would be not allowing kinking to occur if $\tau_{12}^{(\theta)} > S_t$ (as it is expected to result in fiber splitting). This approach is however ill fated if meant to be used in a complex FE simulation. To demonstrate this consider an element of the plate that was modelled before with the FNM. This is depicted in figure 4.8.

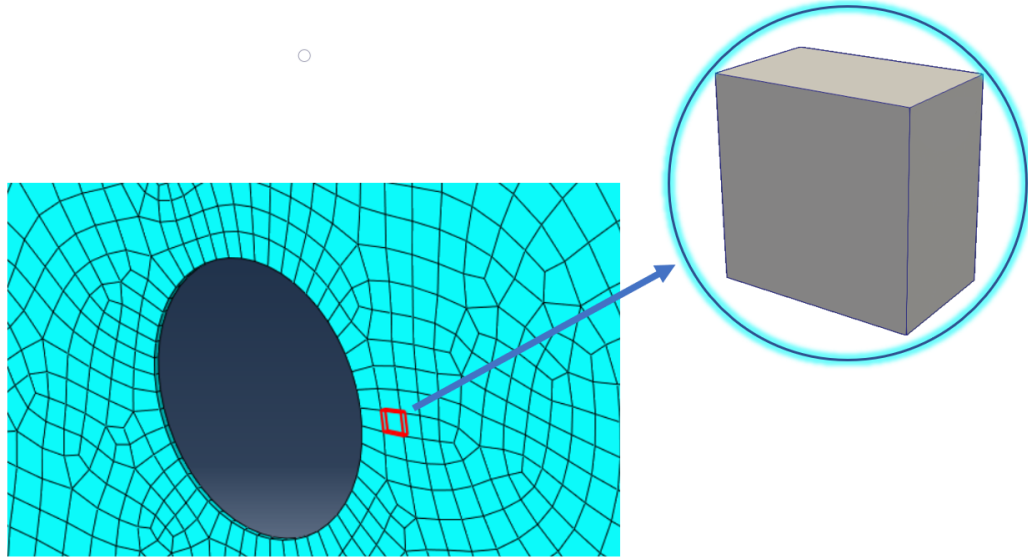


Figure 4.8: Generic FE element in an OHC plate simulation

The element is acted upon by stresses σ_{11} , σ_{22} , σ_{33} , τ_{12} , τ_{13} and τ_{23} . After the kink plane angle θ is determined (as described earlier in this section), the stresses $\sigma_{11}^{(\theta)}$, $\sigma_{22}^{(\theta)}$ and $\tau_{12}^{(\theta)}$ in the kink plane can be determined. The kinking plane is depicted in figure 4.5. Using equation (4.25) the stresses in the kink plane can be related to the maximum bending stress $|\sigma_{b_{max}}|$. Assuming that $\sigma_{22}^{(\theta)}$ has a negligible contribution to $|\sigma_{b_{max}}|$, the latter can be plotted against the kink plane shear stress $\tau_{12}^{(\theta)}$ for a number of σ_{11} values as in figure 4.9. In the same graph a horizontal black line indicates the IM7 fiber strength of $\sigma_{fib_{max}} = 5516$ MPa while a vertical black line indicates the traverse shear strength S_t . If the requirement for kinking is that $\tau_{12}^{(\theta)} < S_t$ as mentioned earlier, the quadrant representing the region of allowed kinking would be the top left one in figure 4.9. The $|\sigma_{b_{max}}| > \sigma_{fib_{max}}$ and $\tau_{12}^{(\theta)} < S_t$.

Now, consider that at certain time step i the axial stress in the element is $\sigma_{11} = 850$ MPa and the shear stress in the kinking plane is $\tau_{12}^{(\theta)} = 25$ MPa. For the IM7/8552 material system the described scenario can be represented like in figure 4.9. At time step i clearly the second kinking criterion is not satisfied as the axial bending stress in the fiber is not sufficiently large to break it ($|\sigma_{b_{max}}| < \sigma_{fib_{max}}$). Even if until time step $i+1$ only the shear stress $\tau_{12}^{(\theta)}$ increases while σ_{11} stays constant, the stress would go through the region of allowed kinking depicted, to arrive in a region which, perhaps due to a too large time increment, is outside the allowed kinking zone. This is of course because the kinking zone is limited by $\tau_{12}^{(\theta)} < S_t$. Clearly the element should have been deemed failed by the kinking criteria, but kinking was not allowed because at time increment $i+1$ the shear stress was too large.

Instead of not allowing kinking to initiate if $\tau_{12}^{(\theta)} > S_t$, a better approach in practice would be to impose a minimum axial stress magnitude for kinking to occur. This results in the third and last criterion for fiber kinking initiation in the current proposed method.

For kinking to occur, the minimum applied longitudinal stress σ_{11} should be large enough such that the maximum bending stress $|\sigma_{b_{max}}|$ can be larger than the fiber strength $\sigma_{fib_{max}}$ for a kink plane shear stress

$$\tau_{12}^{(\theta)} < S_t$$

Taking equation (4.25) and replacing $|\sigma_{b_{max}}|$ with $\sigma_{fib_{max}}$, $\tau_{12}^{(\theta)}$ with S_t and assuming that $\sigma_{22}^{(\theta)}$ is negligible compared with G_{12} and σ_{11} , equation (4.26) is obtained for the minimum axial stress $\sigma_{11_{min}}$. This equation has to be solved for $\sigma_{11_{min}}$ iteratively.

$$\sigma_{fib_{max}} = 120 \left| \sigma_{11_{min}} \sin \frac{\varphi_0 G_{12} + S_t}{G_{12} + \sigma_{11_{min}}} \right| \quad (4.26)$$

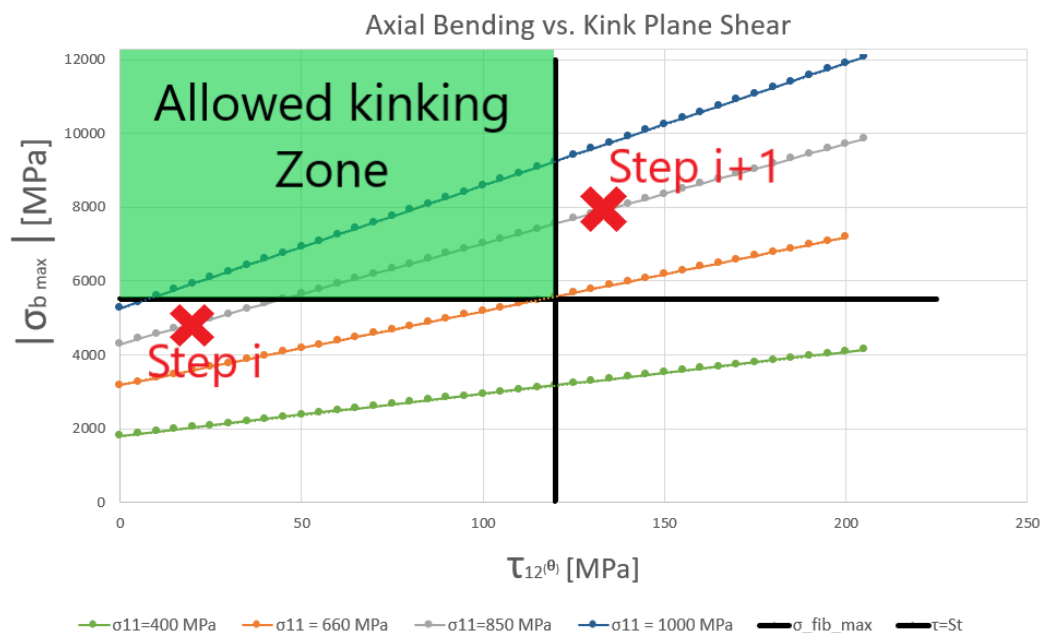


Figure 4.9: Justification kinking condition

Taking again the IM7/8552 material system, this criterion means that kinking should be allowed if and only if $\sigma_{11} < -660$ MPa, that is, if step $i+1$ is above the orange line in figure 4.9. In section 4.1 it was stated that Pinho [65] has suggested that fiber kinking should occur if $\sigma_{11} < -0.5X_c$. For the IM7/8552 material system $X_c = 1690$ MPa according to table A.2, meaning that the requirement would be $\sigma_{11} < 845$ [MPa]. The proposal of Pinho, based on experimental observations, is seen as supporting the criterion proposed here as the requirements proposed are close. But through the procedure presented here it was shown that the requirement proposed can provide an otherwise missing physical basis for the criterion.

To summarize the current section, the fiber kinking onset criteria proposed consists of three requirements. The first was proposed by Argon [4] and solved in the adopted form by Pinho [63]. The latter two are proposed in this thesis. All three are enumerated:

1. For fiber kinking to occur, the matrix around the kinking fibers needs to have failed
2. For fiber kinking to occur, the maximum bending stress in a fiber should be large enough to break it $|\sigma_{b_{max}}| > \sigma_{fib_{max}}$
3. For kinking to occur, the minimum applied longitudinal stress σ_{11} should be large enough such that the maximum bending stress $|\sigma_{b_{max}}|$ can be larger than the fiber strength $\sigma_{fib_{max}}$ for a kink plane shear stress $\tau_{12}^{(\theta)} < St$

4.2.2 Softening Behaviour

Once fiber kinking has initiated in a material point, the load carrying capacity of that point decreases. This phenomenon is called softening. The most common approach to include softening in cohesive laws is to linearly decrease the load carrying capacity at that point such that when the load carrying capacity is lost completely, the area under the stress - displacement curve is equal to the fracture toughness G_{fc}^c of that material. A typical cohesive law is depicted with red in figure 4.10.

The kink-band physics could be better captured if a multilinear softening curve is used. Dávila et. al. [27] proposed a method of superimposing two bilinear cohesive laws to obtain a trilinear law, like depicted in figure 4.10. For the case of fiber kinking one can see the two cohesive laws as modelling different undergoing phenomena. For example, the red curve could model the failure of the fibers while the blue curve could be modelling the frictional stresses at microcrack closure like the aforementioned model of Gutkin [38].

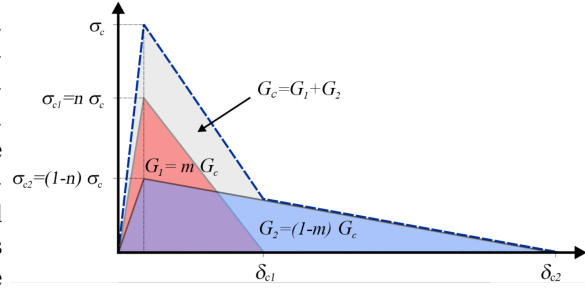


Figure 4.10: Superimposition of Cohesive Laws

The two bilinear laws can be related to a trilinear one using the parameters m and n depicted in figure 4.10. These parameters represent ratios of the fracture toughness and the peak stress respectively. The exact procedure for determining them is beyond the scope of this work, but the most popular way is to use a crack growth resistance curve from a compact compression test of the material system used. For a detailed explanation on how to determine these parameters, the reader is referred to [27] [14]. The m and n for the IM7/8552 material system in longitudinal compression are $m=0.375$ and $n=0.75$, provided by Leone Jr. et. al. [54].

With the m and n determined, the displacements at the traction free state δ_{c1} and δ_{c2} (shown in figure 4.10) of the two bilinear curves can be calculated using equations (4.27) and (4.28) respectively.

$$\delta_{c1} = 2 \frac{m G_{fc}^c}{n E_{11} \varepsilon_0} \quad (4.27)$$

$$\delta_{c2} = 2 \frac{(1-m) G_{fc}^c}{(1-n) E_{11} \varepsilon_0} \quad (4.28)$$

Where ε_0 represents the strain at failure onset. With the help of δ_{c1} and δ_{c2} , the damage parameters d_1 and d_2 can be defined. Those damage parameters are equivalent to the fiber damage parameter d_f defined in section 3.2.2. They are given in equations (4.29) and (4.30) respectively.

$$d_1 = \min \left(1, \frac{\delta_{c1}(u_1 - u_0)}{u_1(\delta_{c1} - u_0)} \right) \quad (4.29)$$

$$d_2 = \min \left(1, \frac{\delta_{c2}(u_1 - u_0)}{u_1(\delta_{c2} - u_0)} \right) \quad (4.30)$$

In equations (4.29) and (4.30), the term u_1 represents the instantaneous longitudinal displacement while u_0 is the displacement at failure onset. The strains and displacements are related via $u = \varepsilon \cdot c_{len}$, where c_{len} represents the characteristic element length (a quantity provided by Abaqus at each integration point). Depending on the relative size of the displacements u_0 , δ_{c1} and δ_{c2} , the assembly into the final d_f is done as shown in equation (4.31), where d_f is the damage parameter prescribing the fiber degradation of the final cohesive law.

$$d_f = \begin{cases} n(d_1 - d_2) + d_2 & \text{if } u_0 < \delta_{c2} \\ 1 & \text{if otherwise} \end{cases} \quad (4.31)$$

4.2.3 Crushing

Most PDAs representing fiber kinking have a governing cohesive law that after failure onset decreases until a traction free state is achieved [7]. Such a traction free state is not specific to compression as the two sides of the kink band will still be in contact even after its complete collapse [7]. Typically, when under compression, after reaching the failure stress, FRPs soften until a stable crush zone is reached [12], as illustrated in figure 4.11. This section will investigate when and how should a residual crushing stress be enforced on the kinking constitutive law. The discussion starts by investigating figure 4.12 which presents a fractographic image of a 0° ply undergoing kinking. Next to it, figure 4.13 presents similar kink band in an advanced state of failure.

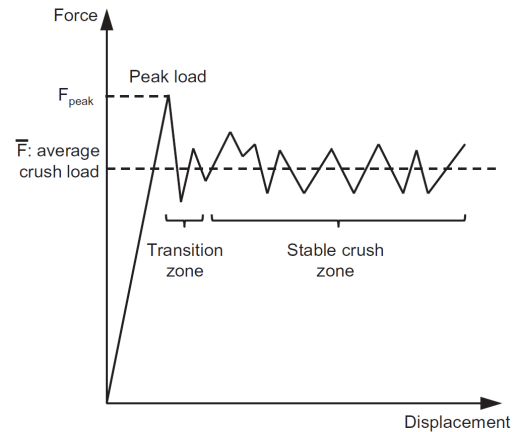


Figure 4.11: Illustration stable crushing zone in composites [12]

It can be seen in the later figure that after the misalignment angle has increased by a lot, the two sides of the kink band are pushed into one another while they try to escape on the sides. Clearly in figure 4.13 the edges of the kink band do not have space to escape. They are thus forced into one another, causing a contact force. If a delamination would be present near the kink band or the same kink band would be on a ply at the edge of the laminate, the sides would be free to escape. The following hypothesis is then proposed:

If a kink band is supported on both sides by an undamaged ply interface, the stress in the material will converge towards the crushing stress of that material system σ_{crush} , otherwise it will go to a traction free state.

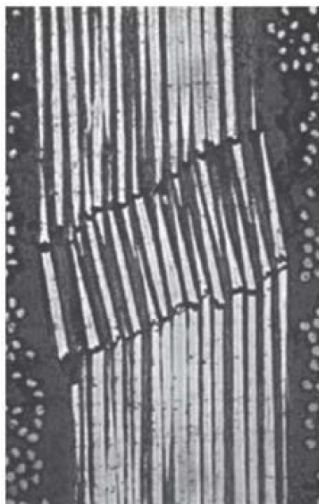


Figure 4.12: Kink band early failure [56]

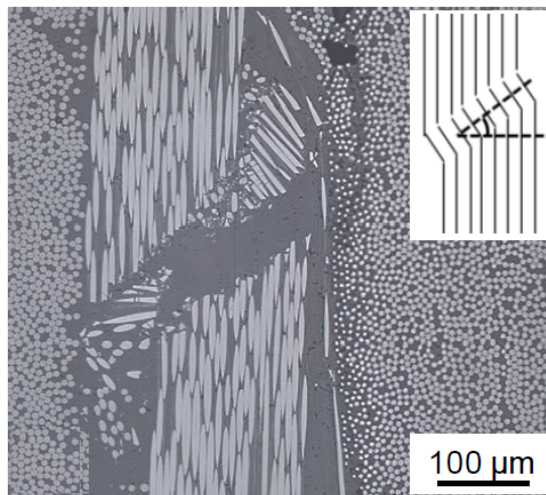


Figure 4.13: Kink band crushing state [23]

The Floating Node Method is perfectly suited to implement this hypothesis numerically. As mentioned in section 3.2, the FNM allows for the sharing of information between the different plies and interfaces that belong to the same local (laminate) element.

The crushing stress σ_{crush} has to be determined experimentally. For the IM7/8552 material system the σ_{crush} is estimated from the crushing tests of composite tubes of the same material. A quasi-static Specific Sustained Crushing Stress (SSCS) of 46.8 kJ/kg is measured for a quasi-isotropic layup [24]. The SSCS is equal to the mean crushing stress σ_{mean} divided by the material density ρ . The obtained mean crushing stress for a material density of $\rho = 1.6$ [g/cm³] is $\sigma_{mean} = \sigma_{crush} \approx 75$ MPa. The crushing stress is enforced by changing the definition of the fiber damage variable d_f previously defined in (4.31). If lateral support exists and the d_f defined in equation (4.31) is larger than the d_f in equation (4.32), the d_f adopts the value from equation (4.32).

$$d_f = 1 - \frac{\sigma_{crush}}{E_{11}\epsilon} \quad (4.32)$$

5

Verification

A short summary of the proposed simulation framework for OHC:

It was concluded that some of the most important deficiencies of the previous PDAs representing OHC are the CDM representation of matrix cracks and the insufficient physical basis behind the modelling of the failure mechanisms specific to fibers in compression. The suggested simulation framework makes use of a relatively recent DCM, named the FNM to model matrix cracks and delaminations while a new CDM for fiber kinking is developed chapter 4.2 and used.

At this point, all aspects of the proposed simulation framework have been discussed. Before jumping into modelling complex problems, the material model proposed in section 4.2 shall be tested in this chapter on smaller scales to verify its validity, robustness and implementation. The FNM has been verified before [21]. The results presented in this chapter have been generated using the properties of the IM7/8552 material system.

5.1 Failure Envelope

A complete evaluation of the fiber kinking initiation criteria discussed in section 4.2.1 can be done by generating and evaluating the failure envelope. These show the interactions between the longitudinal compressive σ_{11} and other stresses. The three independent kinking onset requirements are plotted on the same graph. The change from one criteria being the limiting factor to another is characterized by a change of trend in the envelope. The three requirements for kinking initiation are repeated here for convenience:

1. For fiber kinking to occur, the matrix around the kinking fibers needs to have failed
2. For fiber kinking to occur, the maximum bending stress in a fiber should be large enough to break it $|\sigma_{b_{max}}| > \sigma_{fib_{max}}$
3. For kinking to occur, the minimum applied longitudinal stress σ_{11} should be large enough such that the maximum bending stress $|\sigma_{b_{max}}|$ can be larger than the fiber strength $\sigma_{fib_{max}}$ for a kink plane shear stress $\tau_{12}^{(\theta)} < S_t$

Because the third kinking onset requirement, the maximum axial compressive stress σ_{11} needed for kinking onset for the IM7/8552 material system is -660 MPa, obtained by solving equation (4.26). For this reason, the kinking region can only exist for $\sigma_{11} > -660$ MPa for all envelopes.

As one may expect from a transversely isotropic material, the normal stresses σ_{22} and σ_{33} have the same effect on an element. For this reason the $\sigma_{11} - \sigma_{22}$ and $\sigma_{11} - \sigma_{33}$ interactions are identical and are presented in figure 5.1. The green zone in the envelope represents the region where all the kinking onset requirements are satisfied. One can immediately notice that the first kinking requirement dictates the shape of the envelope for larger magnitudes of σ_{11} . Also, the plot representing this requirement is asymmetric with respect to

$\sigma_{22} = 0$, suggesting the existence of different failure mechanism for tensile and compressive traverse stresses. This behavior will now be explained. As mentioned in section 4.2.1, the kink plane angle θ maximizes the matrix failure index ϕ_{KM} in equation (4.2). A positive $\sigma_{22}^{(\theta)}$ promotes a tension related failure, maximizing ϕ_{KMT} and thus the traction $t_N^{(\varphi)}$ (from equation for ϕ_{KMT}). The latter traction component is maximized for larger positive $\sigma_{22}^{(\varphi)}$, which is in turn highly dependent on $\sigma_{22}^{(\theta)}$. The kink plane angle θ is then chosen such that $\sigma_{22}^{(\theta)}$ is maximized. Therefore if only σ_{22} is applied alongside σ_{11} , $\theta = 0^\circ$. Similarly, when σ_{33} is applied alongside σ_{11} , $\theta = 90^\circ$. The angle θ does not change for the entire upper part of the matrix associated failure envelope. A negative σ_{22} on the other hand maximizes ϕ_{KMC} , where the traction components $t_L^{(\varphi)}$ and $t_T^{(\varphi)}$ play a greater role. The latter traction components are dependent on both $\sigma_{22}^{(\varphi)}$ and $\tau_{12}^{(\varphi)}$ which are in turn are highly related to the values of $\sigma_{22}^{(\theta)}$ and $\tau_{12}^{(\theta)}$. The choice of kink band angle θ when one lateral compressive stress is applied is not straightforward. Moreover, θ changes for different applied negative σ_{22} trying to maximize either $t_L^{(\varphi)}$ or $t_T^{(\varphi)}$. Finally, when $\sigma_{11} = -X_c = -1690$ MPa, no other stresses are needed to satisfy the first kinking requirement. If however σ_{11} is applied simultaneously with σ_{22} and σ_{33} the failure envelope in figure 5.2 is obtained. One can see that if both σ_{22} and σ_{33} are applied (and are negative), the axial stress needed to induce kinking increases in magnitude above X_c . This is due to the lateral support provided to the kink plane by σ_{22} and σ_{33} , not allowing the misalignment angle φ to grow. Since the matrix failure criterion is the one that is not being satisfied, the same behavior can be seen in Pinho's [63] model in figure 5.5. When positive $\sigma_{22} = \sigma_{33}$ are applied however, the envelope stays identical to that of figure 5.1.

When it comes to the plot representing the second requirement it can be seen that an axial compressive stress of $\sigma_{11} = -1040$ MPa is sufficient to meet the criterion when no other stresses are applied. The asymmetry of the plot is also attributed to the different values of the kink plane angle θ for tensile and compressive σ_{22} . A positive σ_{22} induces a $\theta = 0^\circ$, as stated above, meaning that $\sigma_{22}^{(\theta)} = \sigma_{22}$. In this case $\tau_{12}^\theta = 0$ therefore $|\sigma_{b_{max}}|$ in equation (4.25) increases slightly for increasing positive σ_{22} . When a negative σ_{22} is applied, no noticeable effect can be seen on the maximum bending stress $|\sigma_{b_{max}}|$. No negative σ_{22} can satisfy the second kinking requirement for $\sigma_{11} > 1040$ MPa. The characteristic just described occurring in figure 5.1 can be physically justified. Imagining the kinking plane depicted in figure 4.5, located at an angle θ relative to the 1-2-3 plane in which σ_{22} is acting. Regardless of the kink plane angle θ , there is no physical way in which a compressive σ_{22} can increase the bending of the fibers in the kink plane, meaning that indeed no negative lateral stress should be able to initiate the failure of the fibers. Positive lateral stresses on the other hand may promote the bending of the fibers as they can increase the misalignment of the fibers.

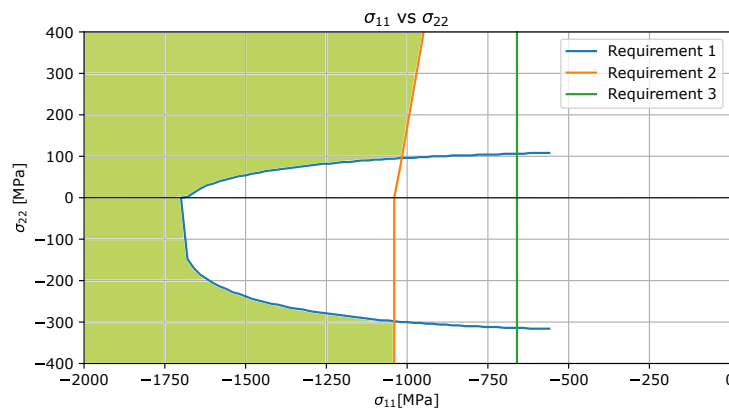


Figure 5.1: Failure Envelope when only σ_{22} and σ_{11} are applied

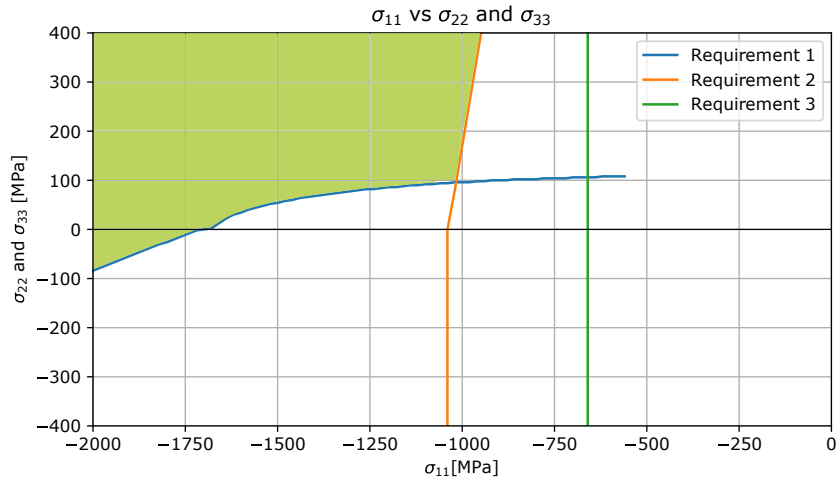


Figure 5.2: Failure Envelope when $\sigma_{22} = \sigma_{33}$ and σ_{11} are applied

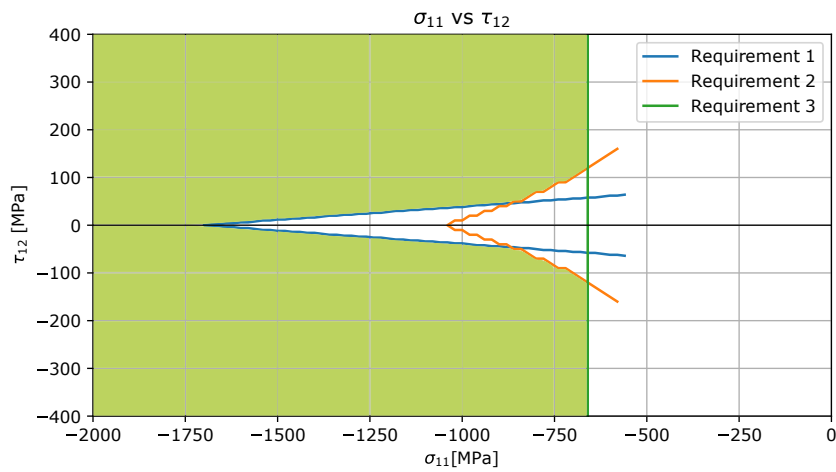


Figure 5.3: Failure Envelope when only τ_{12} and σ_{11} are applied

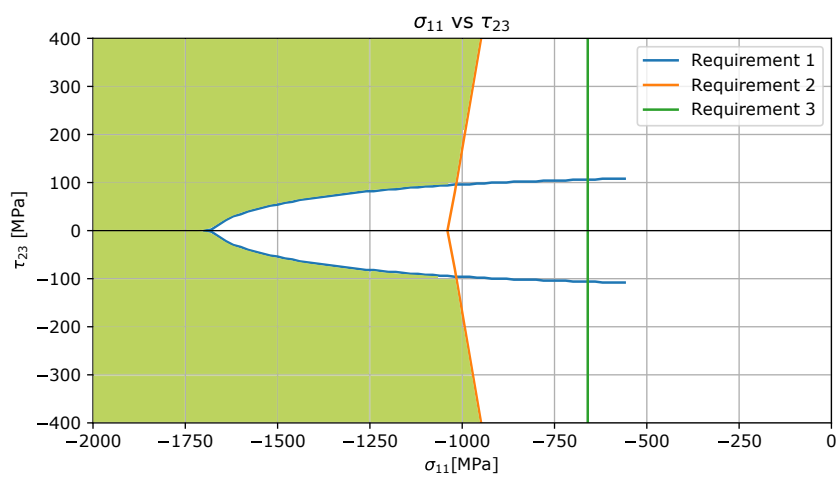


Figure 5.4: Failure Envelope when only τ_{23} and σ_{11} are applied

Figure 5.3 displays the failure envelope for when σ_{11} is applied together with the shear stress τ_{12} or τ_{13} (identical effect). As expected the curves are symmetrical to $\tau_{12} = 0$ MPa since kinking onset should not be affected by the direction of the shear stress. Since the kink plane angle θ is chosen iteratively to minimize the kinking load, when only a shear stress is applied, the kink plane rotates such that $\tau_{12} = \tau_{12}^{(\theta)}$. As expected, since the minimum σ_{11} is calculated such that fibers fail for a kink plane shear stress $\tau_{12}^{(\theta)} < S_t$, the envelope endings are at shear stresses equivalent to $S_t = 120$ MPa.

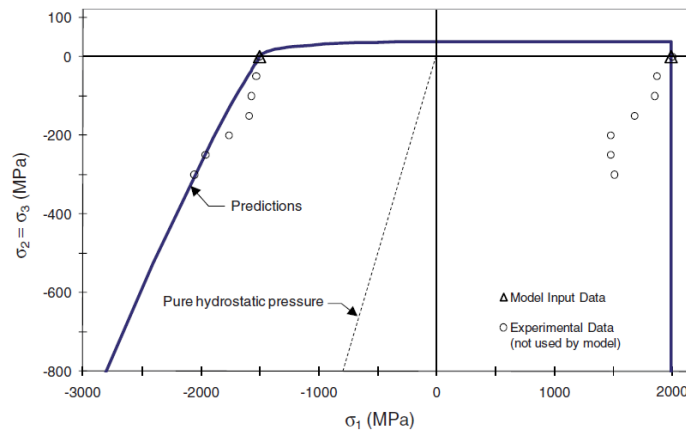


Figure 5.5: Strengthening effect from side support by Pinho [65]

Finally, the failure envelope when σ_{11} and τ_{23} are applied is displayed in figure 5.4. Like in figures 5.1 and 5.2, when the fiber failure requirement can no longer be satisfied by a large in magnitude σ_{11} , large values of τ_{23} become needed for kinking to initiate, due to the reduced effect τ_{23} has on the second requirement.

5.2 Cohesive Law

The shape of the implemented cohesive law as well as the area underneath it can best be checked by running one element simulations. The example element used here is depicted in figure 5.6 with its dimensions. The material has an orientation of 0° (fibres in the direction of the loading).

At first, only a negative vertical displacement is applied at the top while the bottom is constrained from moving. The stress-displacement curve can be seen in figure 5.7. One can immediately verify that the peak load is equal in magnitude to the axial compressive stress X_c in table A.2. The stiffness of the element can be calculated by determining the strain in the element at failure: $\varepsilon = u_1/0.2 = -0.0023/0.2 = -0.0115$ and then dividing the failure stress X_c by it: $E = X_c/\varepsilon = -1690/-0.0115 \approx 150$ GPa (as in table A.2). Since only one element exists in the thickness direction (one ply), no crushing behaviour is present (as there is no lateral support from other plies). Therefore, the area under the cohesive law should be equal to the compressive fracture toughness G_{fc}^c . The numerically calculated area under the curve in figure 5.7 is approximately 26, which matches the fracture toughness $G_{fc}^c = 25.9$ kJ/m².

Figure 5.8 presents the (axial) stress-displacement curve for an element identical to the one used before, but where an axial shear stress of $\tau_{12} = 20$ MPa is also applied. One can see that the critical axial stress is now $\sigma_{11} = -1290$ MPa, which matches the result of the failure envelope 5.3. As expected, despite the lower peak stress, the area under the curve in figure 5.8 remains equal to G_{fc}^c . Since in the model depicted in figure 5.6 the element has no neighbouring plies, no lateral support is provided and therefore no crushing behaviour can be observed.

In order to verify the implementation of the crushing behaviour in the material, the model depicted in figure 5.9 is implemented. This model consists of 3 elements stacked in the thickness direction, each of them representing a ply, the layout is $[90^\circ/0^\circ/90^\circ]$. To make sure no delamination occurs at any of the two interfaces (allowing material to escape), the normal and two shear strengths of the interface cohesive material (τ_{nc}, τ_{lc} and τ_{tc}) have been set to the very high value (90 GPa) to prevent any separation between the plies. In this way, the failed material in the 0° ply will not be able to escape and will be crushed. Being interested only in the behaviour of the 0° ply (where kinking should occur), figure 5.10 shows the stress-displacement curve of only the top nodes of the middle 0° ply. One can see that the stress does no longer decrease to 0 MPa, but instead converges to the crushing value of $\sigma_{crush} \approx 75$ MPa. Note also that the peak stress is bigger than X_c . This is caused by the lateral support provided by plies and requirement no.1 on kinking onset (see figure 5.2).

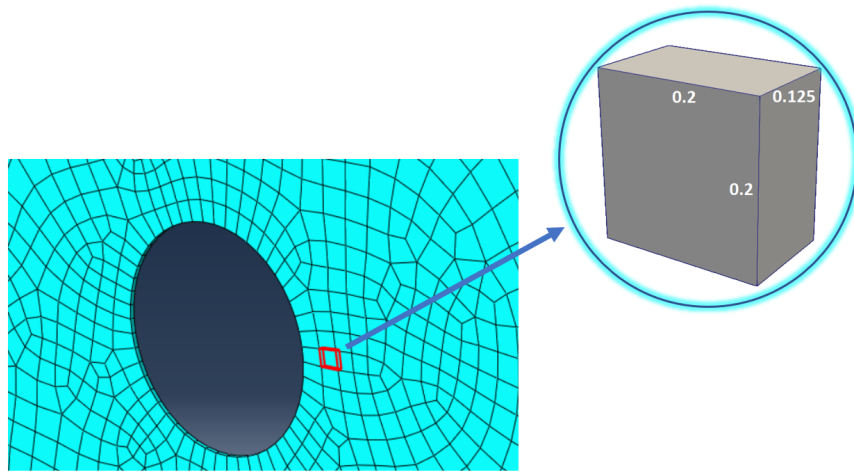


Figure 5.6: Single element geometry

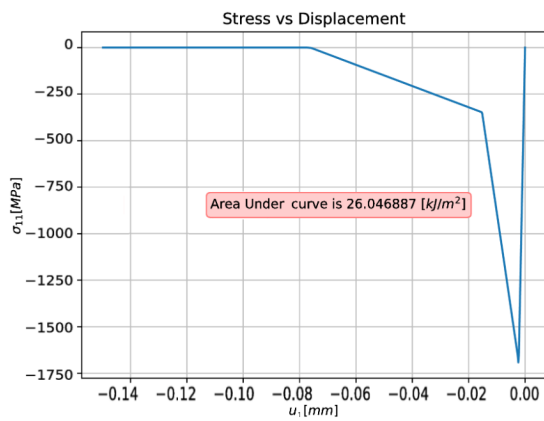


Figure 5.7: Single Element Compression

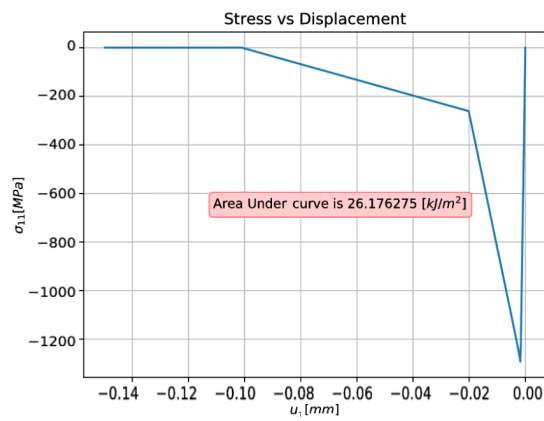


Figure 5.8: Single Element Compression when $\tau_{12} = 20$ MPa

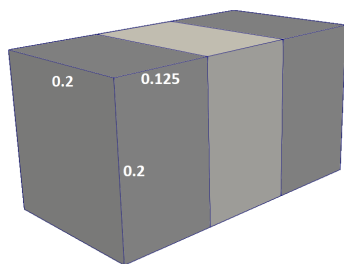


Figure 5.9: Three plies laminate element

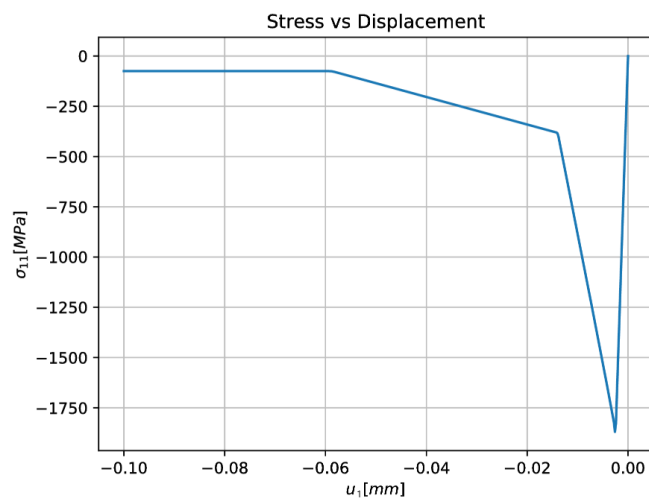


Figure 5.10: Stress-Displacement curve of supported 0 deg ply

5.3 Delamination and cracks in compression

In order to see the interaction of the axial compression method with other failure modes, such as delamination, a coupon like model is tested. The geometry of the coupon is presented in figure 5.11. This shape was chosen in the detriment of a rectangular one in order to control the failure onset location (which is the necked region).

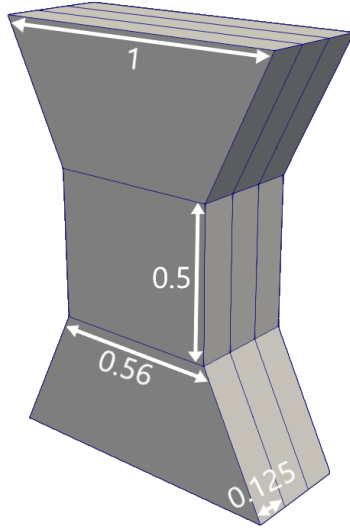


Figure 5.11: Coupon model with [0/90/0] layup

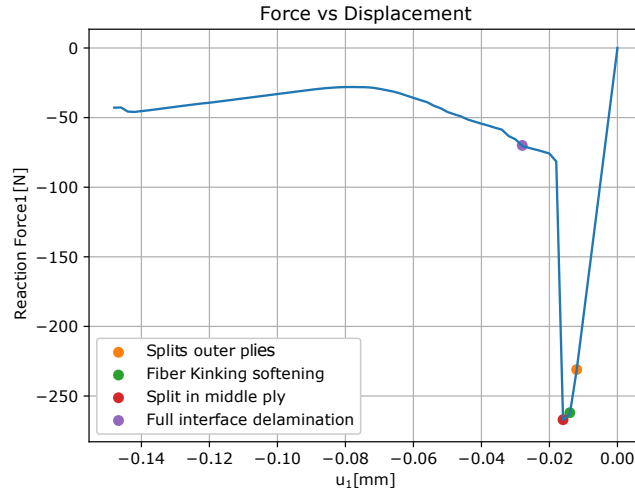


Figure 5.12: Force-Displacement curve for the coupon model

A simple vertical velocity is applied like in the case of the single element. The layup used is a [0/90/0]. The load-displacement curve is shown in figure 5.12. The first point on the graph corresponds to the formation of the matrix splits traversing the entire height of the coupon (suggesting matrix failure criterion has been satisfied), depicted in figure 5.13. Around the peak load, fiber kinking initiates in the 0° plies in the necked region, a mild softening can be seen in figure 5.14. The structural strength is almost entirely lost between the third and fourth points. The stiffness degradation factors for the 0° ply elements in the necked region increases from a range of $df=0.27-0.285$ to $df=0.915-0.917$. The strength left after the load drop is associated with the 90° ply which tries to move laterally into the outer plies. The load increase after the -0.08 mm displacement is thought to be caused by the penalty stiffness preventing sides of 90° ply above and below the crack to overlap each other.

Table 5.1: Critical points on the coupon Force-Displacement curve

Step	Depiction	Displacement [mm]	Force [N]	Note
•	Figure 5.13	-0.012	-231	Matrix cracks appear in the 0° plies
•	Figure 5.14	-0.014	-262	The 0° plies in the necked region start softening
•	Figure 5.15	-0.016	-267	Last step before load drop. Crack in the middle ply
•	Figure 5.16	-0.028	-70	Clear full delamination

5.4 Mesh dependency

The proposed model should show no mesh dependency in the energy absorbed as long as the element size is not large enough to cause "brittle failure". To understand how brittle failure can occur, consider the two elements in figure 5.17.

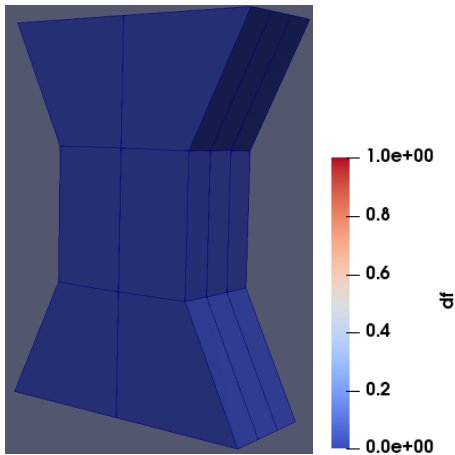


Figure 5.13: Matrix splits in the 0° plies

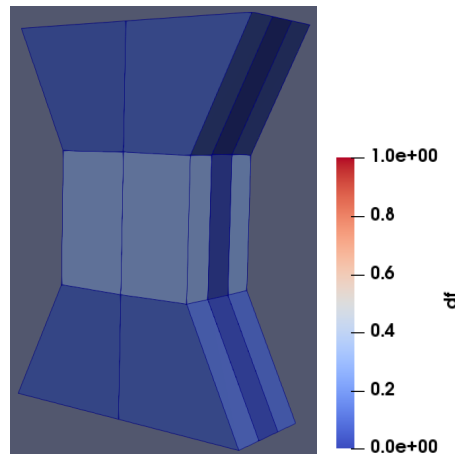


Figure 5.14: Fiberkinking softening

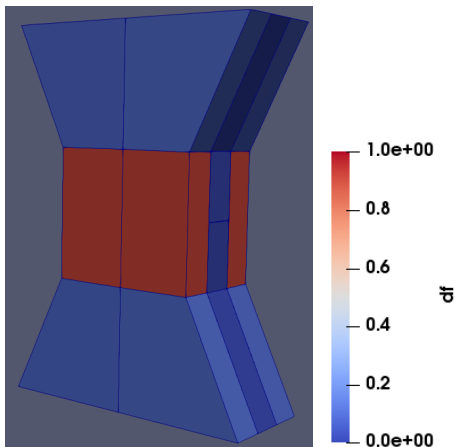


Figure 5.15: Crack in the 90° ply

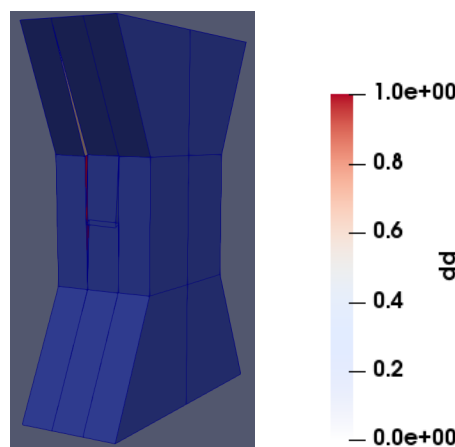


Figure 5.16: Full interface delamination

These elements have the same width and depth but the height of the second element is twice that of the first element. At the failure stress X_c , the strain ϵ_0 for both elements should be given by:

$$\epsilon_0 = \frac{X_c}{E_{11}}$$

While the failure strain is the same for both elements, since the height of the second element is twice that of the first, the displacement at failure initiation for the big element should also be double, thus $2u_0$. Examining again the cohesive law for a single element in figure 5.7, once can imagine that if the magnitude of u_0 is sufficiently large, there comes a point when the area under the stress displacement curve is larger than G_{fc}^c , at failure initiation.

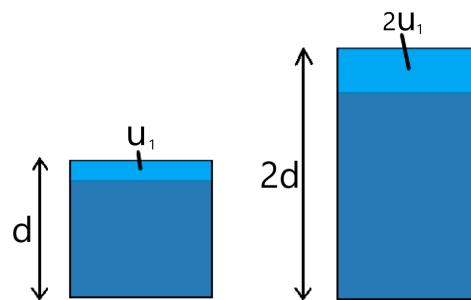


Figure 5.17: Element size and brittle failure

Since the G_{fc}^c has been exceeded, no softening is permitted and the element jumps to a traction-free state (unless a crushing state exists). This is called a brittle failure of an element.

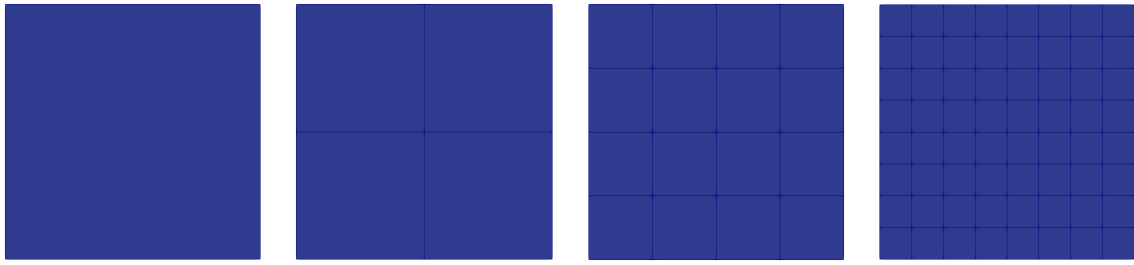


Figure 5.18: One element plate Figure 5.19: Four elements plate Figure 5.20: 16 elements plate Figure 5.21: 32 elements plate

For the case when the element size d is smaller than the critical value inducing brittle failure, the mesh sensitivity can be checked. For this, a square specimen $10\text{ mm} \times 10\text{ mm} \times 2\text{ mm}$ (equivalent thickness of 16 unidirectional plies oriented at 0°) is meshed with 1, 4, 16 and 32 elements. The panel is depicted in figures 5.18, 5.19 5.20 and 5.21 respectively. Those panels are loaded vertically uniformly in compression via an applied velocity. Figures 5.23, 5.24 5.25 and 5.21 show the final failure pattern of those models. The stress-displacement curves can be seen in figure 5.22. The curves are nearly identical when 1, 4 and 16 elements are used, the very small variations being probably caused by the small differences in the onset stress: -1699.5 MPa , -1694 MPa and -1692.6 MPa (in turn caused by the time step used since all models overshoot the $X_c = 1690\text{ MPa}$ in table A.2). The slight offset of the plot representing the 32 elements model is probably associated with the unusual failure pattern presented in figure 5.26, where the top elements are clearly experiencing shear loading. The unusual failure pattern occurred because no artifice is used to trigger failure at any particular location in the panel, therefore random elements failed simultaneously throughout the panel. Nevertheless as expected the failure pattern is predominantly in bands perpendicular to the direction of loading and the stress displacement curves are practically identical.

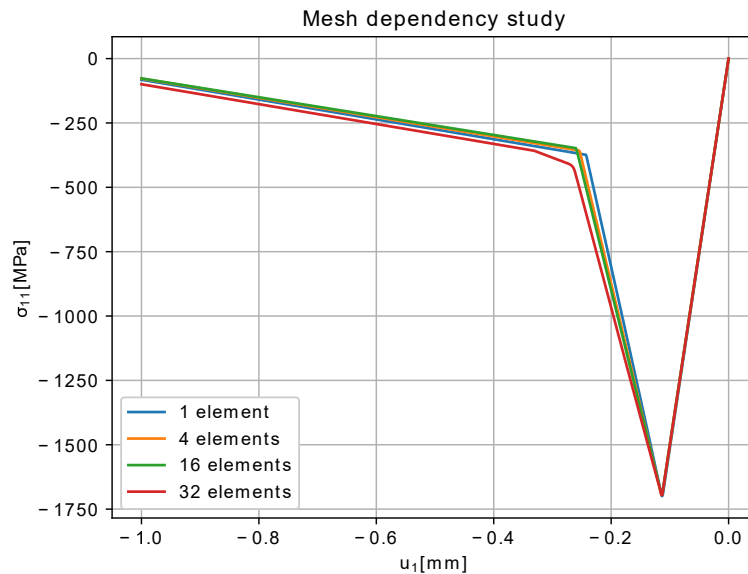


Figure 5.22: Stress-displacement curve for 4 mesh refinement levels

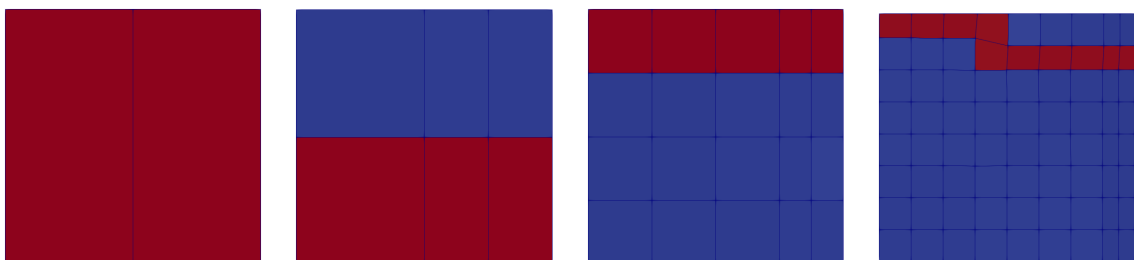


Figure 5.23: Failed plate 1

Figure 5.24: Failed plate 2

Figure 5.25: Failed plate 3

Figure 5.26: Failed plate 4

Finally, the demonstration in this section only goes to show that the current method does not suffer from a pathological mesh dependency in the energy absorbed. However, more complex simulations, such as OHC, are expected to suffer from mesh dependency. The latter is because the volume of damaged material is still mesh dependent in CDMs and because of the mesh specific spatial discretization of the continuum. For this reason, another mesh dependency investigation will be performed for the OHC panel in chapter 6.

6

Validation

In this chapter the proposed simulation setup will be used to model some of the notched plate specimens described in appendix A. This is a considerably more complex simulation than what was presented in chapter 5. The results obtained from these simulations will be compared with the results of the FNM based simulation presented section 3.2.4 (where fiber damage was predicted by the Maximum Stress failure criterion). Furthermore, this chapter will test the convergence capabilities of the model, its mesh dependency, sensitivity to the used time increment as well as its ability to capture thickness size effects and in plane size effects. Unstructured meshes, with one element per ply in the thickness direction are used. No damage trigger function is needed as the central hole acts as a stress raiser. Because the author of the experimental analysis [46] only provided the strengths of the tested panels, no detailed comparison of the Load-Displacement curves is possible. For the sake of fluency only the most important simulation results are mentioned in this chapter. A complete set of results is however provided in Appendix B.

6.1 Comparison with the maximum stress based model

Experiment no. 1 from table A.1 was reproduced in section 3.2.4 with a simulation setup which relied on the Maximum Stress criterion to capture fiber compressive failure. The same experiment was reproduced with a simulation relying on the constitutive model for fiber kinking proposed in Chapter 4 instead of the Maximum Stress. The exact same mesh, time step and material parameters are used. The mesh is depicted in figure 3.14, the time increment used is $\Delta T=0.005$ s, an applied vertical velocity of -1 mm/s is adopted and the material properties used for both simulations are that of the IM7/8552 system, given in table A.2.

The load-displacement curves for the two simulations are compared in figure 6.1. The graphs look identical until in the vicinity of the crushing onset point. The simulation relying on the proposed kinking constitutive law predicts a panel strength of 404 MPa, about 26 MPa below the other simulation. Both simulations overshoot the experimental strength, but the new simulation is closer, only 31 MPa above the experimental value. A possible reason for the Maximum Stress based simulation having predicted a higher panel strength is that fiber failure can only be triggered by the longitudinal stress σ_{11} acting at a point. In reality, other stresses would be acting at the same point, lowering the failure initiation load of that point. Another reason may be associated with the Maximum Stress based simulation having a more extensive damage zone around the hole at the panel maximum load, decreasing the stress concentration factor produced by the hole. The most important aspects of the damage zones will now be described.

Due to its higher relative longitudinal stiffness, the 0° ply will absorb most of the load applied. This means that the state of the 0° ply dominates the panel response. At the maximum applied load, the fiber damage state in the 0° ply for the two simulations can be seen in figures 6.2 and 6.3. The kink band length in both simulations is about the same, however in the simulation where the maximum stress failure criterion was used (in figure 6.2), a significant amount of failed elements exist scattered outside the kink band. No physical explanation can be found for this scatter.

The delamination predicted by the two models at the [-45/0] interface can be seen in figures 6.4 and 6.5 (the grip to grip splits appearing in the figures so far do not represent matrix cracks but just cohesive elements where cracks may occur, an artifact of the FNM). Clearly a more extensive delamination is present in the Maximum Stress based simulation. This can be caused by the delayed final load drop or by the effect fiber failure has on delamination. It is interesting to point out, from the perspective of the new model, that fiber failure advances faster from the hole towards the edges than delamination of the [-45/0] interface (see figures 6.3 and 6.5). This means that elements are initially "supported" from the sides, not allowing a traction-free state to occur as discussed in section 4.2.3. The [90/-45] interfaces are depicted in figures 6.6 and 6.7. Lastly, the [45/90] interfaces are shown in figures 6.8 and 6.9. The matrix cracks occurring in each simulation are depicted in figures 6.10 and 6.11. Since the matrix cracks in each ply are parallel to the fibers in that ply, they can all be illustrated in a single figure without creating any confusion about the ply they are located on. One can see that the amount of delamination as well as its location at each interface is closely related to the matrix cracks in the adjacent plies. From the fiber damage, delamination and matrix cracks presented it is clear that the damage zone at failure onset is more developed in the Maximum Stress based simulation.

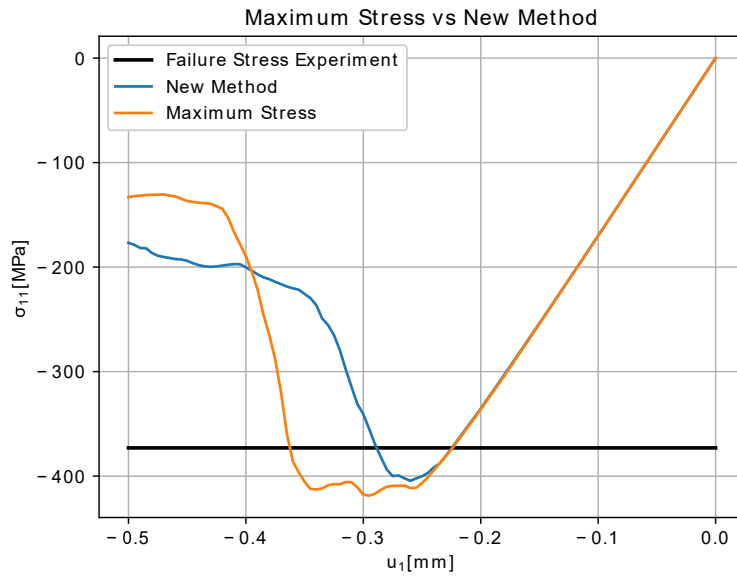


Figure 6.1: Comparison of stress-displacement curves of simulations based on the Maximum Stress and the proposed kinking constitutive law to model fiber failure

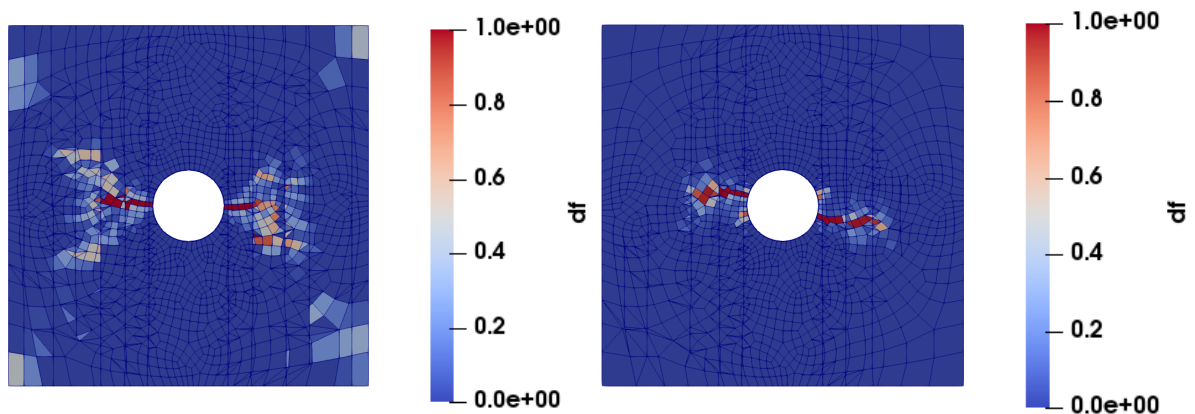
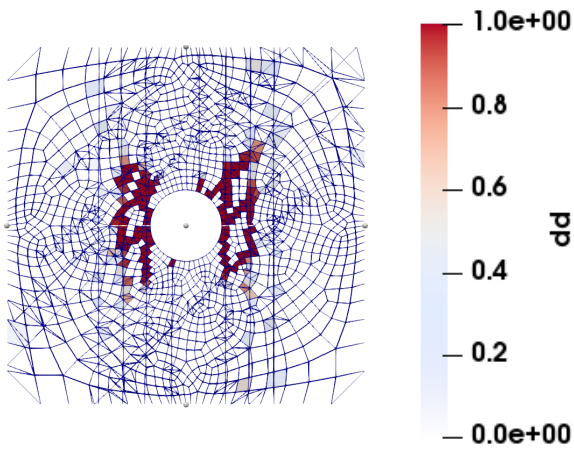
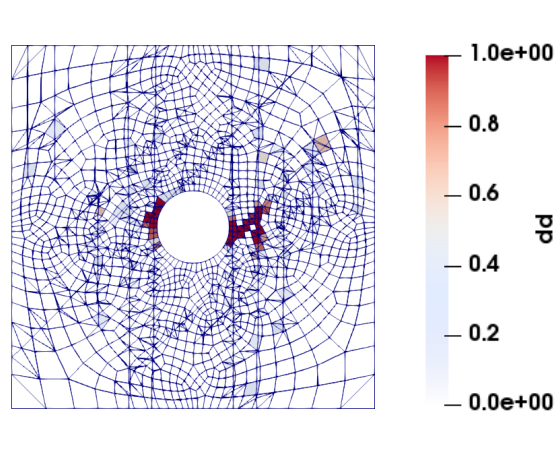
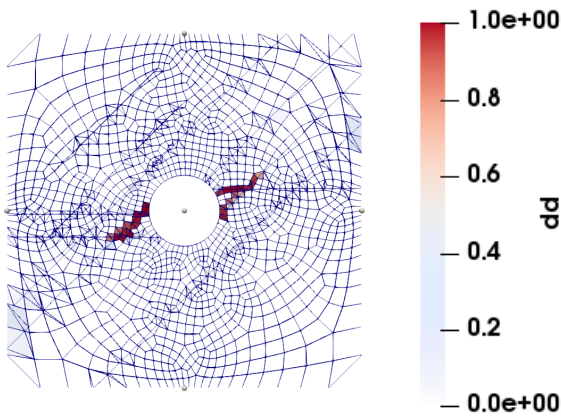
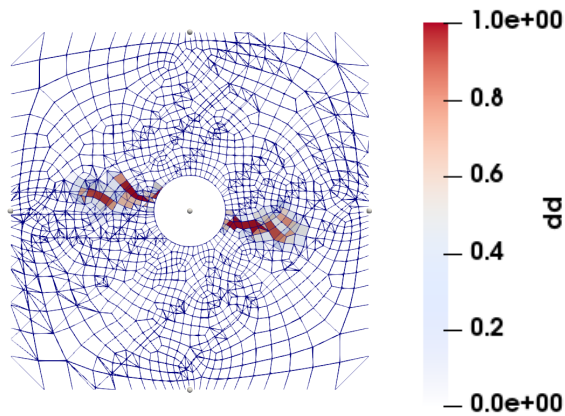
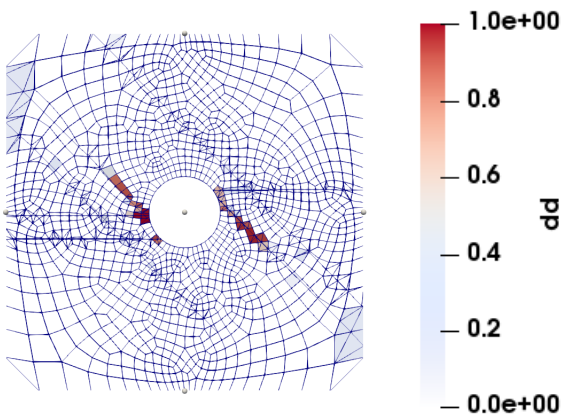
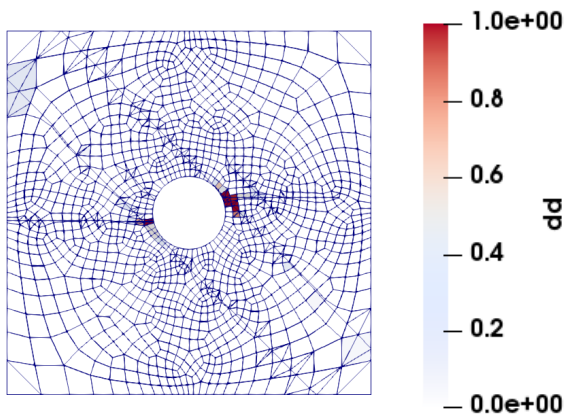


Figure 6.2: Max Stress simulation fib. dam. at max load

Figure 6.3: New Method simulation fib. dam. at max load

Moving past the failure onset point, one can see that no oscillation is present in figure 6.1 around the peak load for the simulation based on the proposed kinking law. Furthermore, the now descending line follows a less abrupt path than the other simulation. The reason for this is associated with the fact that the final load drop in the Maximum Stress simulation occurs at an applied displacement almost 0.1 mm bigger than that

Figure 6.4: Max Stress simulation: $[-45^\circ/0^\circ]$ interfaceFigure 6.5: New Method simulation: $[-45^\circ/0^\circ]$ interfaceFigure 6.6: Max Stress simulation: $[90^\circ/-45^\circ]$ interfaceFigure 6.7: New Method simulation: $[90^\circ/-45^\circ]$ interfaceFigure 6.8: Max Stress simulation: $[45^\circ/90^\circ]$ interfaceFigure 6.9: New Method simulation: $[45^\circ/90^\circ]$ interface

of the new simulation. Because of this, a lot more energy has been put into the panel when the final load drop starts, meaning that the softening of the elements, governed by a cohesive law, need to follow a steeper softening curve (keep the dissipated energy constant). If the final load drop of the two simulations would occur simultaneously, it is expected that the new simulation would initially soften faster. This is because the cohesive law in the new simulation (shown in figure 5.7) displays a more abrupt softening just after failure than a simple linear softening law (which would connect the failure onset and traction free points).

Figures 6.12 and 6.13 provide the failure pattern of the 0° ply in the two simulations at an applied displacement of $u_1 = -0.5$ mm. The failure lines have begun at the edges of the hole and have progressed towards the side edges of the panel. It can be seen that the simulation based on the proposed kinking law predicts a

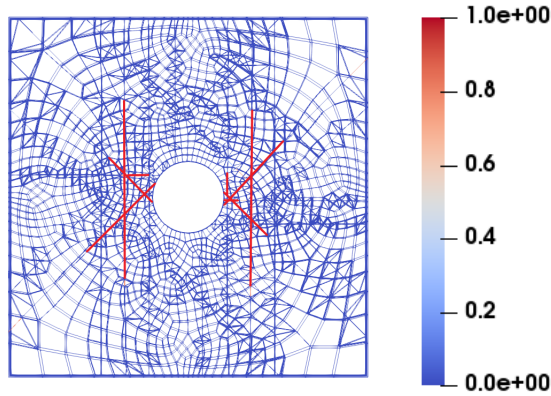


Figure 6.10: Max Stress simulation matrix cracks

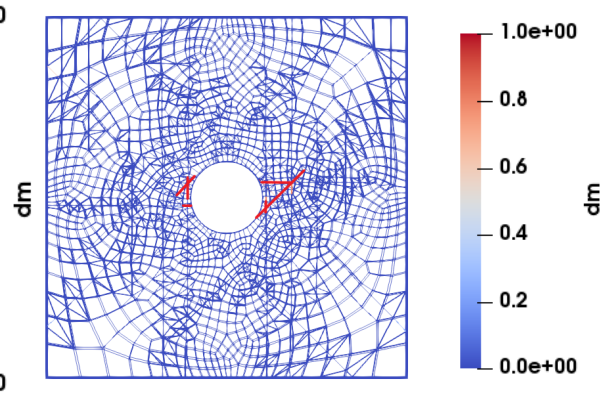


Figure 6.11: New Method simulation matrix cracks

fiber damage pattern that is almost continuous and horizontal, just like a kink band. At $u_1 = -0.5$ mm, delamination (and thus also the matrix cracks) away from the hole (where the elements size is the smallest) is not expected to be accurate as it will be explained in the next section. The fiber failure in the 45° ply as well as the delamination and the matrix cracks for the two simulations at $u_1 = -0.5$ mm can be found in appendix B.

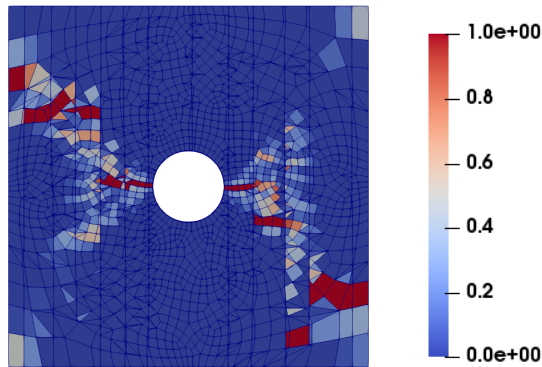


Figure 6.12: Max Stress Sim. late damage state

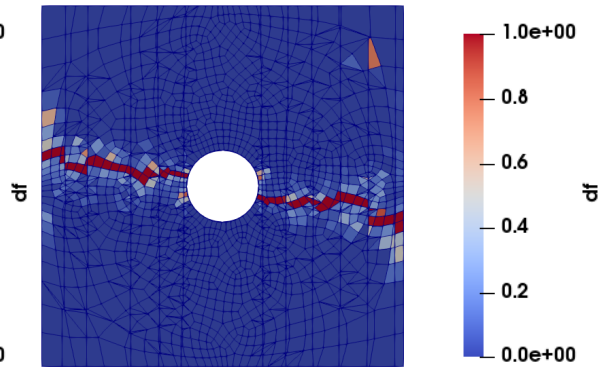


Figure 6.13: New Method Sim. late damage state

6.2 Mesh dependency of the OHC problem

As with most FEM models, the shortcoming of mesh dependency is expected to play a role in the current model. The main reason is that the damaged area depends on the elements orientation and size. Another limitation that comes with using an unrefined mesh is that the minimum allowed spacing between two cracks increases. This minimum spacing is artificially imposed to prevent crack arrest due to an insufficient density of floating nodes [15]. The mesh sensitivity study is done by performing three panel simulations using meshes of three different refinement levels, shown in figures 6.14, 6.15 and 6.16. In the coarse mesh element size varies from 0.7 mm near the hole to 4 mm at the corners, in the (original) medium refined mesh they vary from 0.35 mm to 3 mm while in the refined mesh, the element size varies from 0.2 mm to 2 mm.

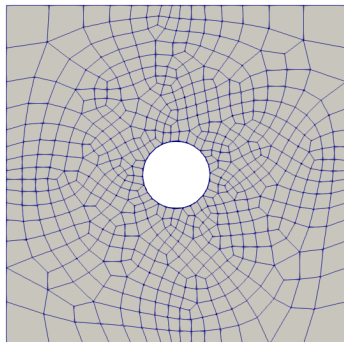


Figure 6.14: Coarse Mesh

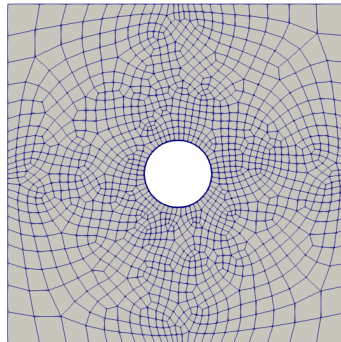


Figure 6.15: Original Mesh

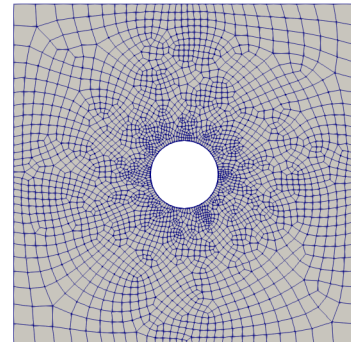


Figure 6.16: Refined Mesh

The force-displacement curves obtained from the 3 simulations are presented in figure 6.17. One can see that the model with the coarse mesh predicts the smallest panel strength and is overall situated beneath the other two curves. The simulation with the original mesh predicts the highest panel strength and is overall above the other two curves. Finally, the simulation with the most refined mesh is situated between the other two, suggesting the method converges towards a strength located in between that obtained with the coarse and normal meshes.

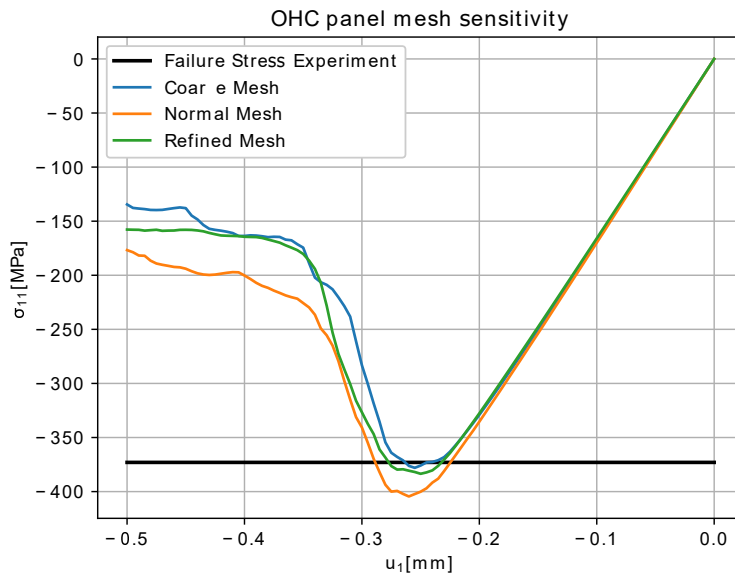


Figure 6.17: Force displacement curve for 3 mesh refinement levels and an applied time step of $\Delta T = 0.005$ s

As a purely theoretical discussion, in this model, delamination should be affected by a large extent by the element size in the mesh as it is modelled via cohesive elements placed at the ply interfaces. The latter are sensitive to the element size since a sufficient refinement level is required to capture the stress gradient in the wake of the delamination/crack. While this discussion goes beyond the scope of this thesis, a general rule when cohesive elements are sized for capturing delamination (mainly affected by mode II loading in this case as the sides are supported), at least two elements should exist per cohesive zone length l_{cz} [71]. For the IM7/8552 material system, with the currently used ply thickness of 0.125 mm, the cohesive zone length $l_{cz} \approx 1.42$ mm, meaning that elements should not exceed 0.71 mm. When choosing the three mesh refinement levels, the elements size near the hole and along the horizontal were kept below this size. Meanwhile at the corners larger elements could be placed as no significant delamination was expected up until a very late post failure state. But this means that the delamination depiction in post failure states are not expected to be completely accurate and will generally not be included in this chapter unless otherwise stated. They can however be visualized in appendix B.

At failure onset the fiber failure in the 0° ply for the simulations with the three mesh refinement levels are depicted in figures 6.18, 6.3 and 6.19. It can be seen from these images that when the original mesh is used, the amount of CE modelling matrix cracks is more abundant than when the coarse and refined meshes are used. Consequently, also less matrix cracks are present at failure onset as it can be seen in figures 6.20 and 6.21 (as compared to figure 6.11). Since there are less matrix cracks, delamination is also less spread in the simulations with coarse and refined meshes, as presented in figures 6.22 and 6.23 respectively (all interfaces can be represented by a single figure). The reason for the difference in the number of cohesive elements representing cracks should still be investigated. Since the 0° ply has the greatest influence on the results of these open hole compression tests the effect of delamination and cracks is reduced as it can be seen from the comparison in figure 6.17. On the other hand, if buckling would not be prevented in the experiment by the anti-buckling plates, as explained in appendix A, then delamination prediction would be crucial for an accurate strength prediction.

The fiber failure at $u_1 = -0.5$ mm for the coarse and refined meshes can be seen in figures 6.24 and 6.25 respectively while for the standard mesh it was already presented in figure 6.13. It can be seen that the kink band size relative to the panel varies significantly because of the mesh element size.

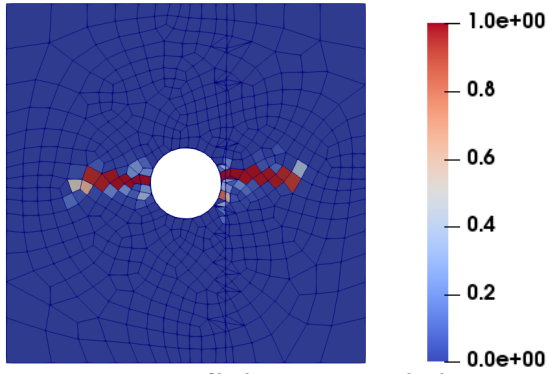


Figure 6.18: Coarse M. fib. dam. at maximum load

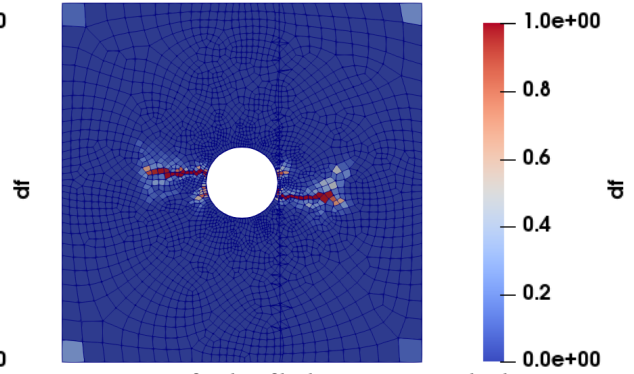


Figure 6.19: Refined M. fib. dam. at maximum load

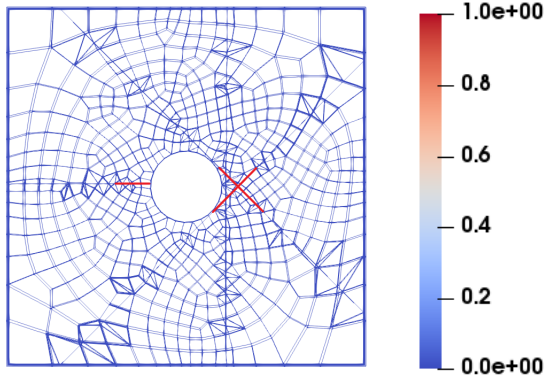


Figure 6.20: Coarse M. matrix cracks at maximum load

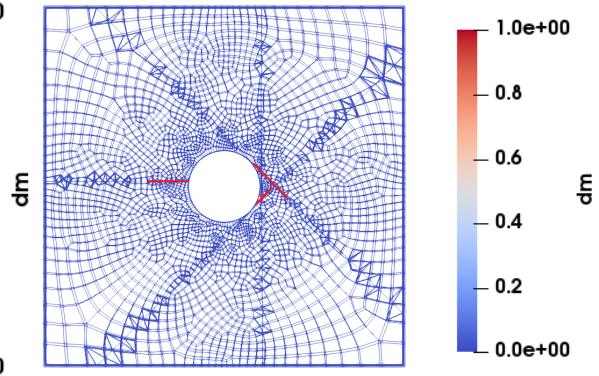


Figure 6.21: Refined M. matrix cracks at maximum load

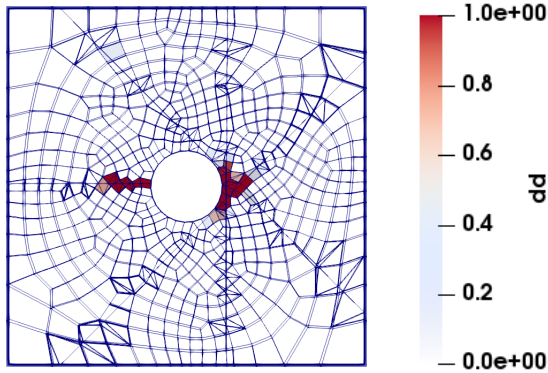


Figure 6.22: Coarse M. delamination at maximum load

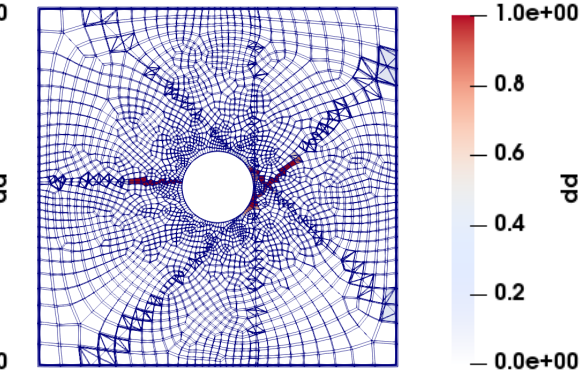


Figure 6.23: Refined M. delamination at maximum load

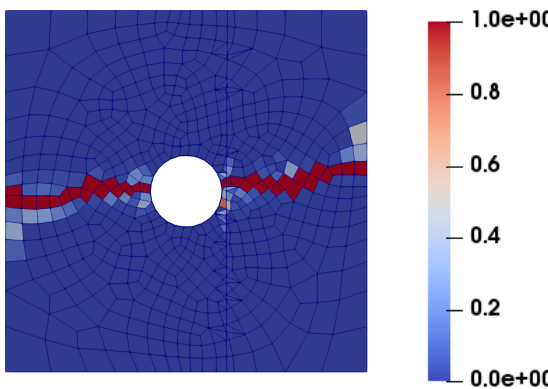


Figure 6.24: Coarse M. Fib. dam. at late dam. state

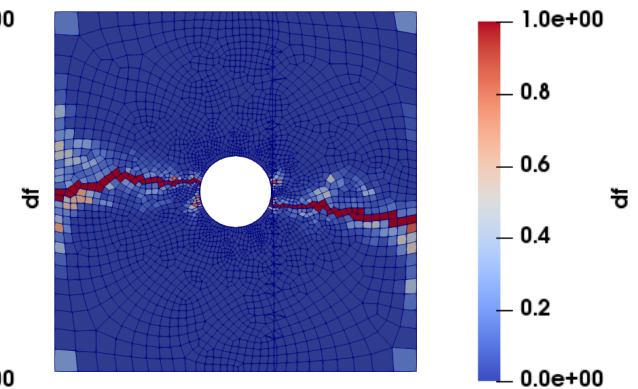


Figure 6.25: Refined M. Fib. dam. at late dam. state

6.3 Sensitivity to used time increment

Large time increments can have a significant negative effect on the results of FE simulations. To explain why, imagine the panel being compressed by a vertical velocity like it was done so far. At time increment i , the stresses in a hypothetical element near the hole are not large enough to onset kinking ($\phi_{KM} < 1$ or $|\sigma_{b_{max}}| < \sigma_{fib_{max}}$). At time increment $i+1$ however, due to the large step, the stresses may have overshoot the minimum necessary ones for kinking by a large value. Since no artifact is used to account for this overshoot, the stresses at time increment $i+1$ become the kinking initiation stresses. Because the false initiation stresses are larger than the real ones and because these may further cause "brittle failure" (defined in section 5.4), the panel will have a higher overall strength as more energy is being dissipated into it.

Studying the plot in figure 6.26 it can be seen that indeed the larger the used time step, the larger the predicted panel strength is. Another effect of the large increment is the extensive spread of damaged elements at the peak load depicted in figure 6.27 as opposed to when a smaller time increment is used as in figures 6.3 and 6.28. Due to the large increment non-critical elements fail together with the critical ones before the latter fail and absorb a larger portion of the applied displacement. Another contributor for the significant difference in the damage pattern is attributed to the significantly larger displacement u_1 at which the maximum load is reached in the three simulations, as it can be seen in figure 6.26 (more energy put into the system). This effect is not observed on the matrix cracks and delamination as it can be seen in sections B.5 B.2 and B.6.

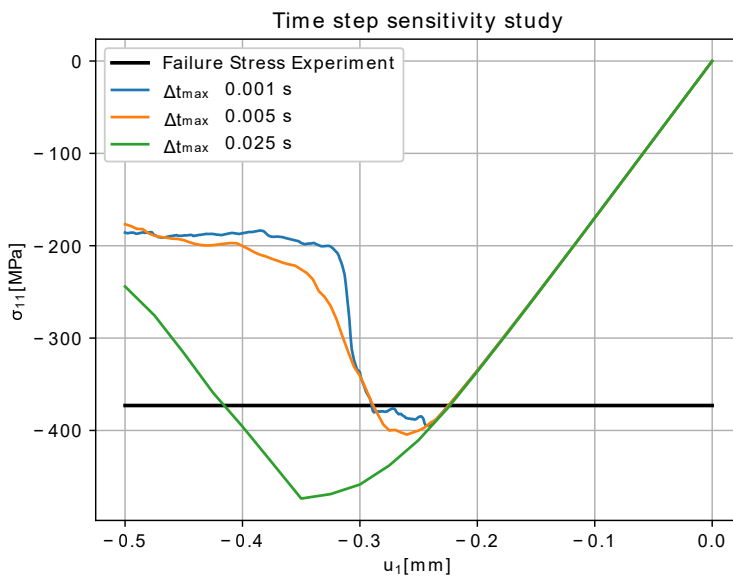


Figure 6.26: Stress-displacement curves for the standard panel using 3 different time steps

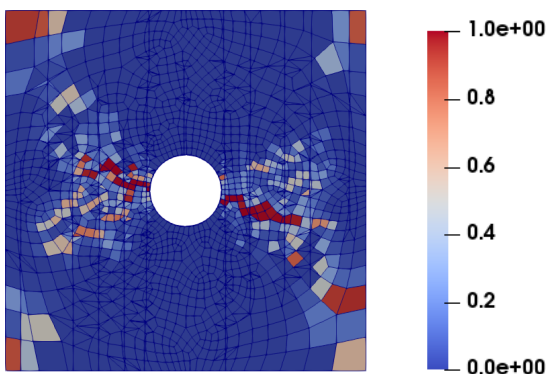


Figure 6.27: Fiber damage at max load for large time increment model

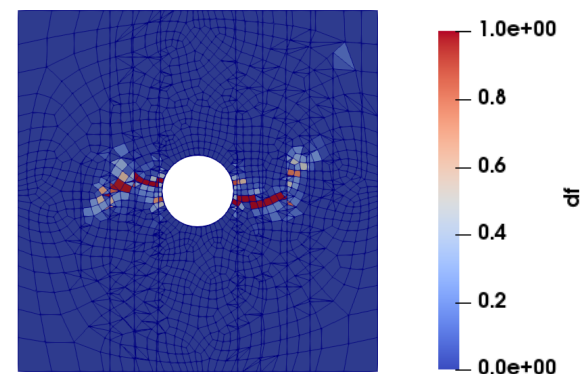


Figure 6.28: Fiber damage at max load for small time increment model

The damage pattern at $u_1 = -0.5$ mm for the simulations with $\Delta T_{max} = 0.025$ s and $\Delta T_{max} = 0.001$ s can be seen in figures 6.29 and 6.30 respectively. Despite the very large number of damaged elements visible in the

large time increment simulation, the kink band can still be distinguished. It is clear however that the proposed simulation is greatly affected by the maximum allowed time increments in the simulation.

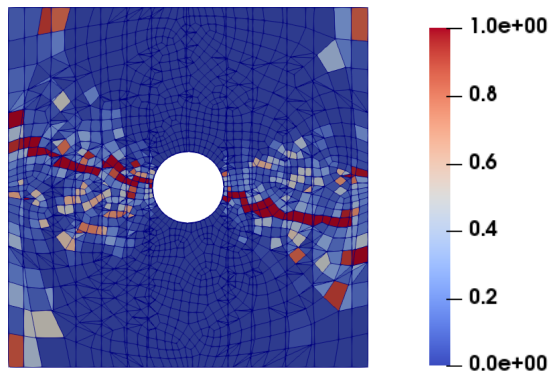


Figure 6.29: Fib. dam. for large time increment model in late damage state

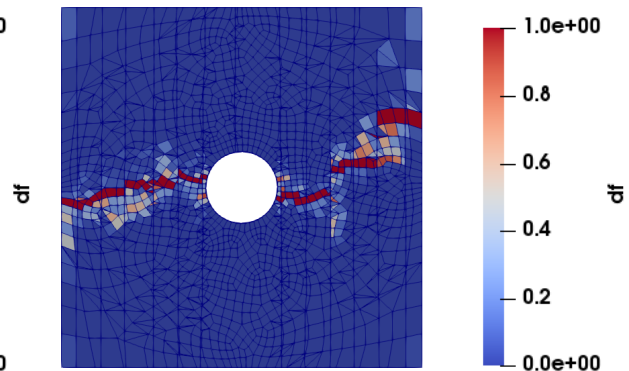


Figure 6.30: Fib. dam. for small time increment model in late damage state

6.4 Thickness scaling

This section aims to assess whether thickness size effects can be captured by the simulation framework proposed. Two types of thickness scaling exist, sublaminar scaling and ply-level scaling, both are depicted in figure A.1. Only ply-level thickness scaling will be checked here. That is because, first of all, no significant size effect has been captured for sublaminar scaling in the experiments of Lee et. al. [46] as can be seen in table A.1 (e.g. comparing experiments 2 and 4). Secondly, due to the increased number of interfaces, a larger number of elements would have to be used in the thickness direction, making the analysis more computationally restrictive. Lastly, it is generally believed that thickness size effects are harder to capture in ply level scaling [71] [19] [67].

To reduce the possibility of mesh size effects or effects caused by the time step affecting the results, the same mesh and time increment are used as with the standard panel. The only difference is that in the thickness direction the elements are larger due to the ply thickness doubling. The stress displacement curve of the simulation of the ply scaled panel can be seen alongside that of the standard panel (introduced in section 6.1) in figure 6.31. It can be seen that a strength increase has been predicted for the thicker panel and this strength is just above the experimentally determined one. One of the driving factors for the strength increase in the scaled laminate is the increase in fracture toughness G_{fc}^c of each ply, as described in section 3.2.3. The toughness increase means that more energy will have to be dissipated to produce the same amount of damage. This is confirmed by the delayed crushing onset of the thicker laminated as shown in figure 6.31.

The 0° ply fiber damage at the maximum panel load can be seen in figures 6.32 and 6.33 for the standard and for the thick laminates respectively. The failed elements at the corner of the ply scaled laminate are probably a result of: 1) the clamping of the upper and lower edges; 2) the higher shear stresses that come as a result of having a stiffer adjacent -45° oriented ply.

The significant difference in the amount of matrix cracks predicted by the two simulations is visible comparing figures 6.34 and 6.35, at an applied displacement of $u_1 = -0.5$ mm. As expected, the thicker plies of the ply scaled laminate are more resistant to the formation of matrix cracks. The delamination estimation in late crushing stage is depicted in figures 6.36 and 6.37. It can be clearly seen that the ply scaled panel sees much less delamination. This is an unexpected result as usually, because ply blocked plies carry larger loads than thinner plies, the interfaces are responsible for transferring more load. This should cause a more spread delamination pattern. It appears however that the simulation only captures delamination related to matrix cracks. A more spread out delamination was expected in the ply scaled laminated.

The final fracture pattern for the standard and ply scaled laminate simulations are presented in figures 6.38 and 6.39. From the latter it can be seen that failure is represented via a continuous band of damage. On the other hand, the reason why a single cohesive element for matrix crack representation is present in the 0° ply still needs to be understood.

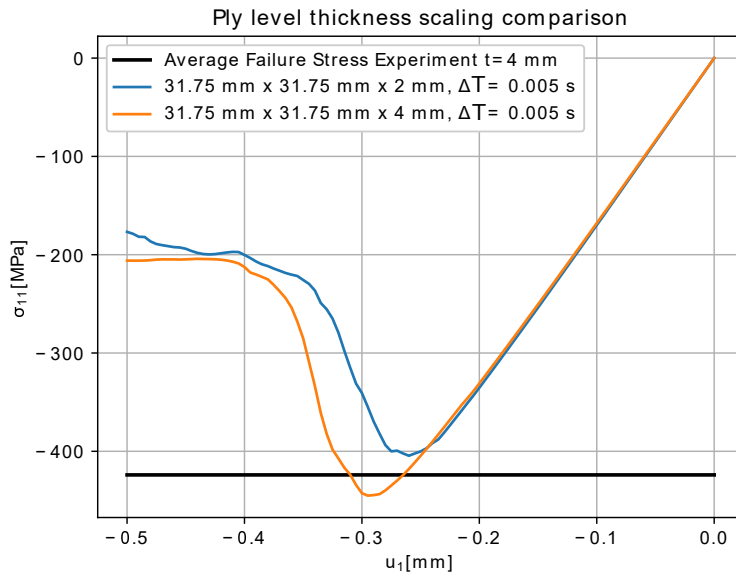


Figure 6.31: Force displacement comparison when ply-level scaling is performed

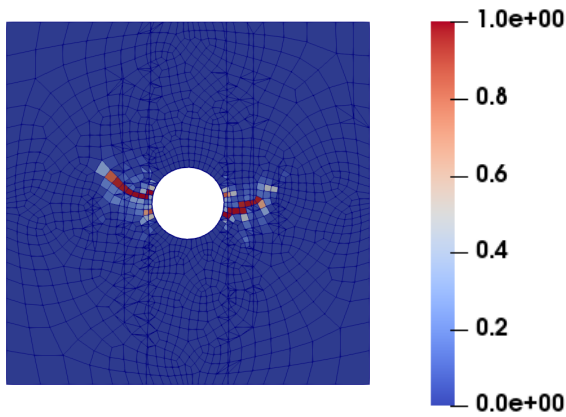


Figure 6.32: Fiber damage at maximum load

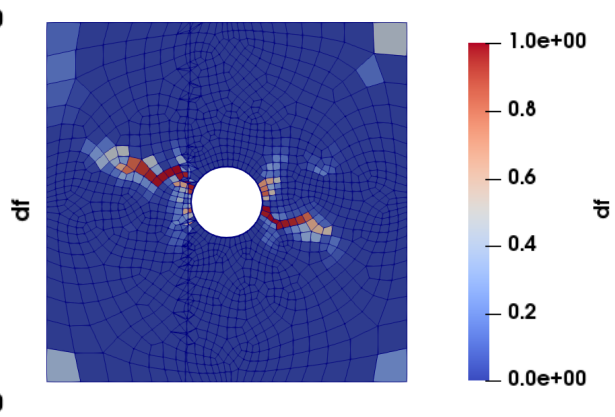


Figure 6.33: Thick laminate damage at maximum load

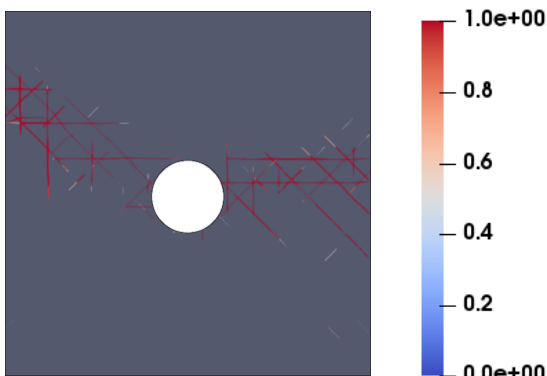


Figure 6.34: Dense matrix cracks in normal laminate

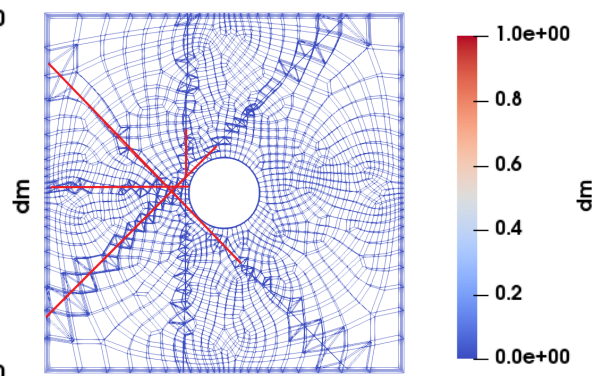


Figure 6.35: Sparse matrix cracks in thick laminate

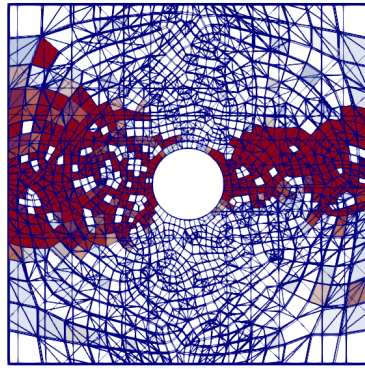


Figure 6.36: Delamination in normal laminate

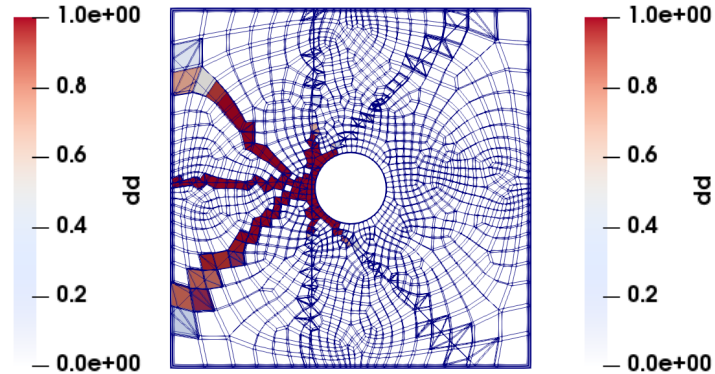


Figure 6.37: Little delamination in thick laminate

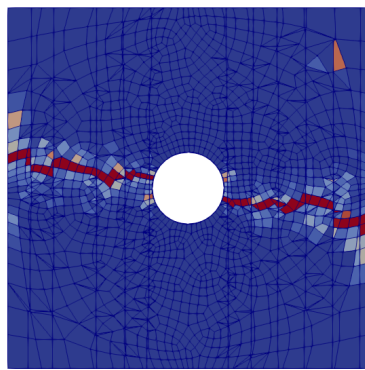


Figure 6.38: Fib. dam. thin panel in late damage state

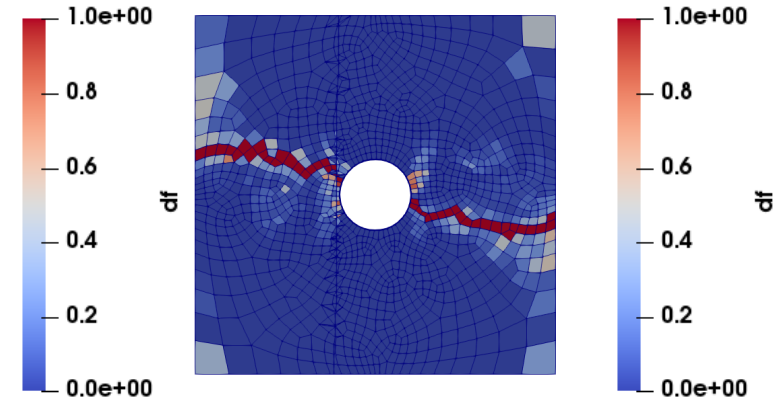


Figure 6.39: Fib. dam. thick panel in late damage state

6.5 In plane scaling

Finally, the in plane size effects are investigated by modifying the in plane dimensions of the panel while maintaining a ratio between the panel width and the diameter of 5. The large panel has a width of 127 mm compared to 32 mm. Since it has a thickness of 4 mm, it will be compared with the thick panel described in the previous section, which also had a thickness of 4 mm. The element size in the mesh varies from 0.7 mm, near the hole and along the horizontal, to 4 mm at the panel corners. The displacement rate is kept the same (as opposed to keeping the strain rate the same) in order to reproduce the experiment exactly.

Since the displacements that need to be applied on the larger panel to fail it are much larger, the σ_{11} vs u_1 curve that was shown until now has been transformed in σ_{11} vs $u_1/(\text{width})$ such that the two plots can be compared. The graph is displayed in figure 6.40. It can be immediately spotted that the larger panel has a much lower strength (lower by 30%).

Due to the presence of the notch, the region of crushing initiation is limited to the vicinity of the hole, meaning that the size effect weakest link theory does not play any significant role. On top of that, since the in plane geometry is scaled and the layup is identical, the stress concentration factor near the hole stays the same. The problem of in-plane size effects for quasi-brittle materials, such as carbon-fiber epoxy systems, under compression has been investigated by Bažant et. al. [6]. He could prove that materials that undergo a progressive propagation of damage before final failure are affected by deterministic energetic size effects. For a better understanding of this concept the reader is referred to [5] [6].

The obtained simulation results are in relatively good agreement with the experiment, suggesting that the in plane size effects have been captured. The experiments show a decrease in strength of 32% for the larger panel. Figures 6.41 and 6.42 present the fiber damage at crushing onset. It can be observed that the fiber failure fracture pattern is more restrained for the large panel, due to the lower longitudinal stress at which crushing is onset. On top of that, the elements at the corners have not failed as they did for the smaller panel.

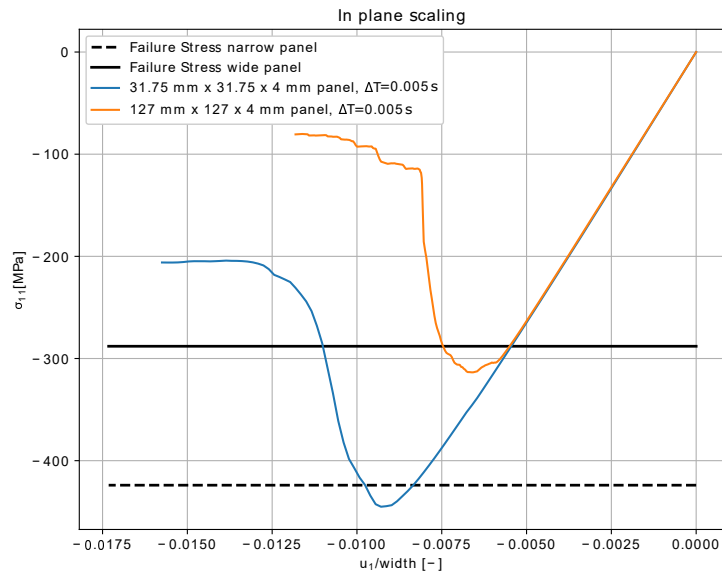


Figure 6.40: Stress-relative displacement curve showing in plane scaling size effects

The latter is probably associated with having a larger area to transmit the shear stresses from the -45° ply to the 0° ply. Delamination is still limited to the regions where matrix cracks are present as it can be seen in figures 6.43 and 6.44. The fully propagated fiber failure bands are illustrated in figures 6.45 and 6.46.

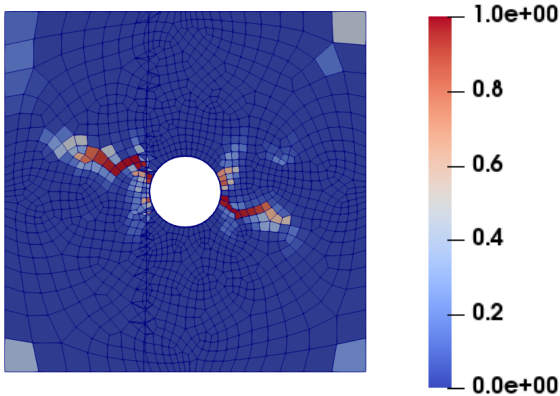


Figure 6.41: Fib. dam. in 4 mm thick panel at maximum load

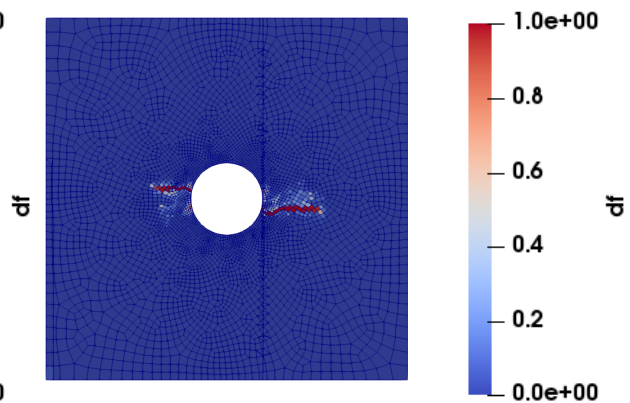


Figure 6.42: Fib. dam. of large panel at maximum load

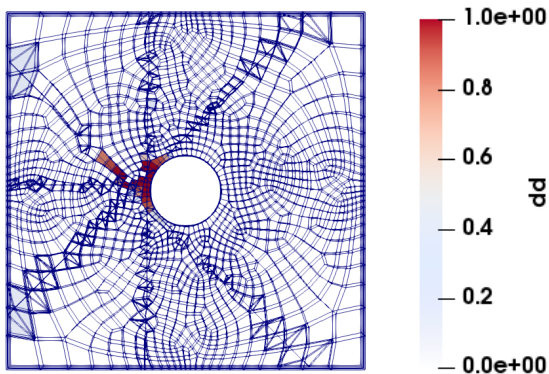


Figure 6.43: Delamination in 4 mm thick laminate

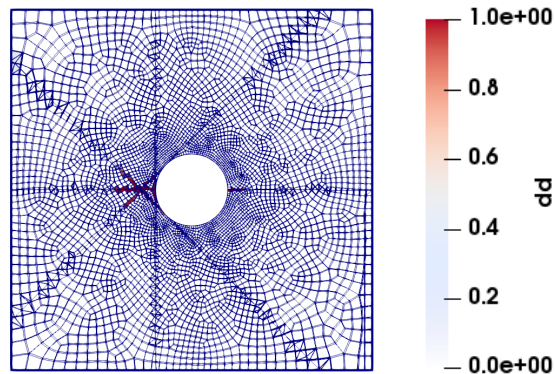


Figure 6.44: Delamination in large panel

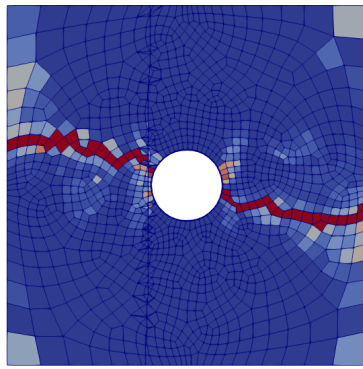


Figure 6.45: Fib. dam. of 4 mm thick panel in late damage state

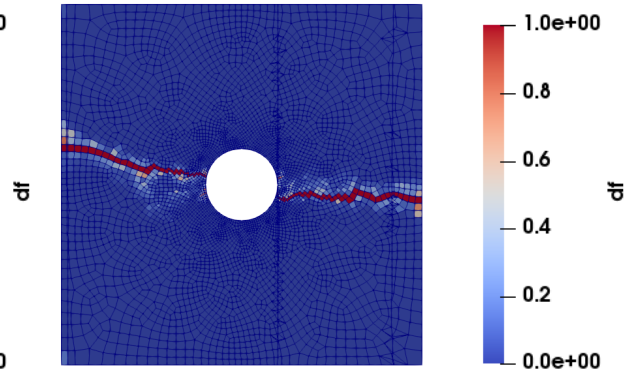


Figure 6.46: Fib. dam. of large panel in late damage state

6.6 Results Summary and experimental comparison

An overview of the simulated panel dimensions and their predicted strengths put in comparison with the experimentally obtained ones is given in figure 6.47. The predicted panel strength is always larger by about 20-30 MPa than the experimental value. The predicted panel strength is more accurate when the proposed kinking constitutive law is adopted instead of the maximum stress failure criterion, as shown in section 6.1.

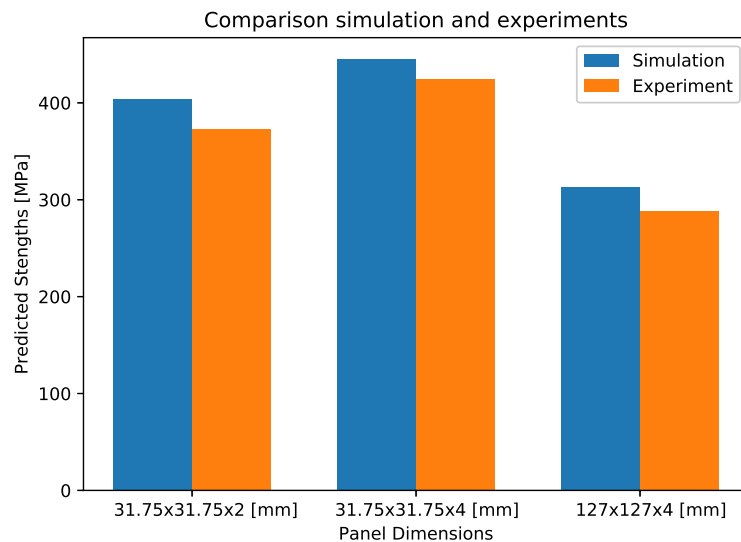


Figure 6.47: Comparison simulation and experimental results

One should keep in mind however that stability issues were encountered by Lee et. al. [46] when testing the 32 mm x 32 mm x 2 mm panel. Bending stresses were detected by back to back strain gauges near the hole. An exact quantification of the effect this had on the experimental values is not possible. These issues were not encountered in the thicker lamiantes probably due to the higher resistance the plies have against out of plane displacement. Lee et. al. [46] indicates that the observed failure mode for the panels simulated in this chapter is push-out (caused by fiber kinking of the 0° plies). A depiction of the push-out failure mode on the outer 45° ply can be seen in figure 6.48.



Figure 6.48: Push-out failure of the 45° ply [46]

The simulation framework currently cannot model the push out failure explicitly. However since the latter is

a consequence of fiber kinking, it is not needed for making a physically accurate strength prediction. The 32 mm x 32 mm x 4 mm panel test was interrupted at 75-80% and 90-95% of the failure load and scanned with X-Ray. At 75-80% of the failure load, matrix cracks are present around the hole, but no delamination, as can be seen in figure 6.51. The simulation using the proposed compression model does predict matrix cracks on the 0° ply, but not as large as the experiments (see figure 6.49). Furthermore, an additional crack in the 45° ply is predicted which is not visible in the experiment. Finally, from figure 6.50 it can be seen that delamination is predicted by the simulation at the edge of the hole. This delamination is not visible in the X-Ray. Extensive delamination can be seen around the hole in the experiment at 90-95% of the failure load as in figure 6.54. The predicted delamination is however smaller and located to the side of the hole as can be seen in figure 6.53.

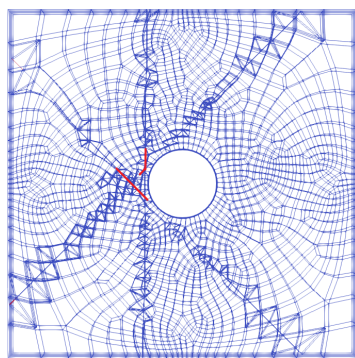


Figure 6.49: Matrix cracks

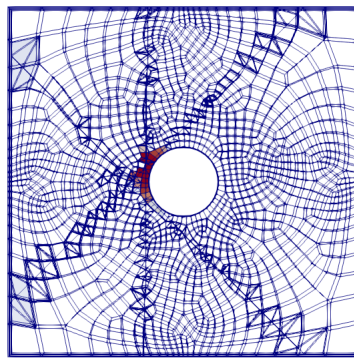


Figure 6.50: Delamination

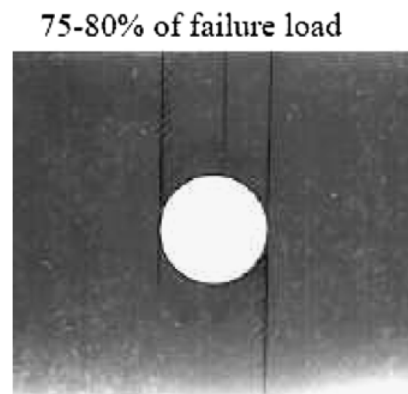


Figure 6.51: Experimental damage-zone in thick laminate [46]

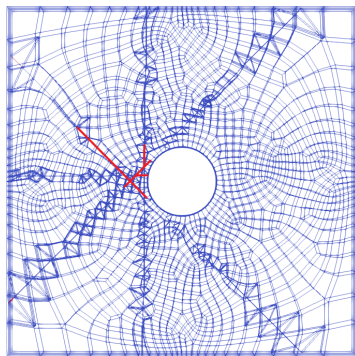


Figure 6.52: Matrix cracks

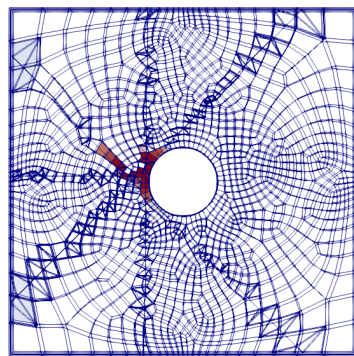


Figure 6.53: Delamination

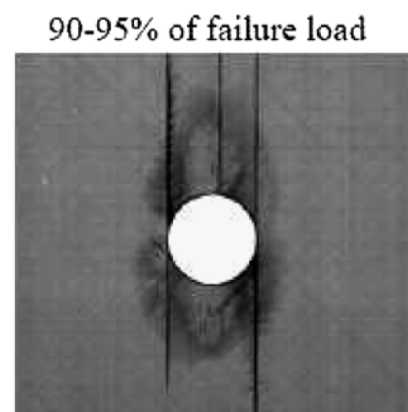


Figure 6.54: Experimental damage-zone in thick laminate [46]

It appears that the current modelling of matrix cracks and delamination is not in agreement with the experiments of Lee et. al. [46]. This issue may be connected with the problem pointed out in section 6.2 where it was observed that the spread of matrix cracks was severely affected by the mesh used. Moreover it is concluded that while the solution of the simulation is not very sensitive to the element size in the mesh, the maximum allowed time increment is crucial. That is because non-critical elements fail and because no function has been implemented to account for the overshoot of the imposed kinking requirements. Moreover, more accurate simulations may be obtained if the assumption of perfect materials is removed, a structured mesh and a small time increment are used.

All the simulations discussed in this chapter have been performed using a computer board containing 2x Intel Xeon CPU E5-2640 v4 @ 2.40GHz (10 cores). The CPU time of the Maximum Stress based simulation and the simulation based on the proposed kinking law are shown in figure 6.55. It can be seen that the simulations based on the proposed fiber failure constitutive law reached panel strength load faster than the simulation based on the maximum stress criterion. That is however caused by the oscillations around the peak load that were present when the maximum stress is used, as can be seen in figure 6.1. The simulation time of T=0.5

s (where the simulations were stopped) was reached faster by the Maximum Stress based simulation. That is expected as the proposed method makes use of two iterative procedures for determining the failure onset point. The effect on computational time of using more refined meshes can be seen in figure 6.56. Similarly, the decrease in computational time associated with using a larger time increment can be seen in figure 6.57.

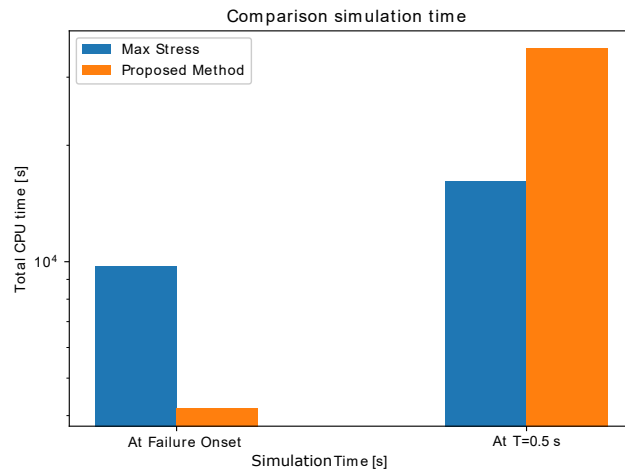


Figure 6.55: Comparison CPU time simulations based on Maximum Stress and based on the proposed kinking method

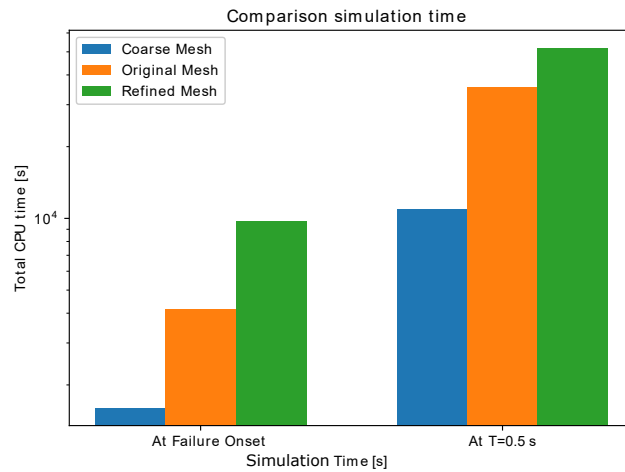


Figure 6.56: Effect of mesh refinement on CPU time

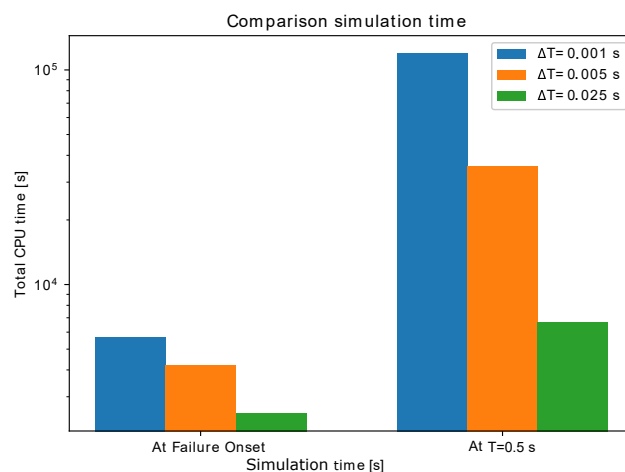


Figure 6.57: Effect of time increment on the CPU time

Conclusions and Recommendations

Conclusions

Previously adopted approaches to model Open Hole Compression of Fiber Reinforced Polymers have been investigated and basic Finite Element Modelling concepts have been introduced. It was determined that meso-scale finite element based Progressive Damage Analyses have the highest potential of providing a reasonably accurate and fast solution to the OHC problem. Two main shortcomings common in PDAs modelling OHC have been identified: 1) The Continuum Damage Models used in Progressing Damage Analyses fail at accurately representing cracks in complicated problems (such as OHC); 2) The lack of sufficient physical basis of the constitutive laws governing compressive fiber damage initiation and propagation in the analysis.

Discrete Crack Models are a better alternative to CDMs for crack and delamination representation within a finite element domain. The capabilities of the state of the art eXtended Finite Element Method as implemented in Abaqus are assessed by trying to reproduce an OHC experiment. Convergence issues were however encountered before the panel reached its maximum load. A more recent approach, called the Floating Node Method, is found to be a better suited alternative.

For modelling longitudinal compressive fiber failure, a physically based 3D Continuum Damage Model for kink band initiation and crushing is proposed in this thesis. Taking the form of a trilinear cohesive law this material model incorporates the microscale bending stress of a fiber, under the assumptions of the Euler-Bernoulli beam theory, while accounting for neighboring delamination in the softening behavior. Three kinking onset requirements are necessary: 1) the matrix around the kinking fibers needs to have failed; 2) the maximum bending stress in a fiber should be large enough to break it $|\sigma_{b_{max}}| > \sigma_{fib_{max}}$; 3) the minimum applied longitudinal stress σ_{11} should be large enough such that the maximum bending stress $|\sigma_{b_{max}}|$ can be larger than the fiber strength $\sigma_{fib_{max}}$ for a kink plane shear stress $\tau_{12}^{(\theta)} < S_t$. The first requirement represents Argon's hypothesis [4] and is implemented in the form by proposed by Pinho [63]. The second is based on fractographic investigation of kink bands. Finally, the third requirement, supported by experimental results, is meant to distinguish fiber kinking from the similar shear dominated fiber splitting phenomenon. After kinking onset, a bilinear curve obtained via superimposition, as proposed by Dávila et. al. [27], is used to more accurately represent the physics behind softening and assure a mesh objective dissipation of fracture energy. Finally, In the last softening stage, the proposed material model assumes that a traction free state can only be achieved if the kink band endings are able to escape out of plane on either side of the kinked ply through existing delaminations.

A finite element based simulation framework that uses the FNM to represent cracks and the fiber kinking constitutive law proposed above to model fiber kinking. The described simulation framework is used to simulate a number of OHC problems in laminates of [45/90/-45/0]s layup having a width to hole diameter ratio of 5. The panel is modeled with an unstructured mesh and the ply material used is IM7/8552. The proposed simulation framework is validated against experimental OHC tests of different sized [45/90/-45/0]s laminates. In

all cases, the predicted panel strengths do not exceed experimental data by more than 8% while both thickness and in plane size effects are captured. The predicted and experimental panel strengths are shown in table 7.1. Compared to a simulation where longitudinal compression was modelled using the maximum stress method, the proposed simulation could predict the panel strength more accurately by 7%. However, the proposed simulation was 2.2 times more computationally demanding. Both simulations have been performed using a computer board containing 2x Intel Xeon CPU E5-2640 v4 @ 2.40GHz (10 cores).

Table 7.1: Comparison simulation results with experimental data for laminate layup of $[45/90/-45/0]_s$

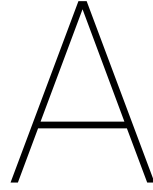
Width [mm]	Thickness [mm]	Hole diameter [mm]	σ_{test} [MPa]	$\sigma_{\text{simulation}}$ [MPa]
31.75	2	6.35	373	404
31.75	4	6.35	424	445
127	4	25.4	288	313

Since the results of the simulations are dominated by the fiber failure of the 0° ply, the strength predictions made are in good agreement with experimental results. It was determined however that the simulations did not accurately capture the matrix cracks and delaminations encountered in the experiments. If out of plane displacement was permitted, delamination could become the critical failure mode, in which case the strength predictions would no longer be accurate. It was determined also that an unusual correlation exists between the number of matrix cracks in a simulation and the mesh used. This issue represents a topic for further investigation.

7.1 Recommendations for future work

This thesis has been focused on delivering a computational framework capable of simulating Open Hole Compression problems of Fiber Reinforced Polymers. The framework proposed was validated against OHC tests. The studies undertaken by this thesis have identified a number of additional areas of future work for the proposed simulation framework as well as suggested subjects of investigation:

- Imagine the stresses at a certain time step i are not large enough to satisfy the proposed kinking onset requirements. At time step $i+1$ the requirements may be satisfied by a sufficient margin. The method then decides that the kinking onset stress is equal to the stress at time step $i+1$: $\sigma_0 = \sigma_{i+1}$. But in reality σ_0 is always smaller than σ_{i+1} , meaning that an error will accumulate in the simulation making the material stronger than it actually is. A method to knock down the stresses σ_{i+1} is needed. Since the kinking onset criteria is 3D, all stresses acting at that point have a contribution to satisfying the kinking onset criteria, it is not straightforward by how much should each stress be knocked down. An investigation should be made and an appropriate knock down method implemented.
- The simulations performed show that matrix cracks and delamination are highly dependent on the mesh used and they have been inaccurately captured. This issue needs to be further investigated.
- The constitutive law proposed accounts for the delamination at the neighbouring interfaces when a crush state is reached. It is expected however that matrix cracks in the neighbouring plies may also interact with kink bands. This possibility should be investigated and if relevant discoveries are made, they should be implemented into the kinking model.
- Finally, because kink bands are only about $100 \mu\text{m}$ wide, an accurate representation at their size in a FE model using a CDM would require a very refined mesh. It would be interesting to investigate the possibility of using a similar approach for modelling kink bands as the FNM uses to model matrix cracks. Namely, when kinking is initiated in an element, that element is split and a CE added representing the kink band.



Standard OHC-test setup

To aid a possible future validation stage as well as the comparison of results with different methods, standard geometry, material parameters and boundary conditions will be used. These are taken from the experiments on OHC performed by Lee et. al. [46].

The plies used are common carbon/epoxy pre-preg tapes of 0.125 mm thickness. The ratio between the hole diameter and the plate width is always five. The base stacking sequence used is $[45/90/-45/0]_s$ which is scaled up at both ply and sub-laminate level ($[0_4]_{ms}$, $[45_n/90_n/-45_n/0_n]_s$ and $[45/90/-45/0]_{ms}$). The two scaling means are depicted in figure A.1. The dimensions and layups of the tested plates can be seen in table A.1.

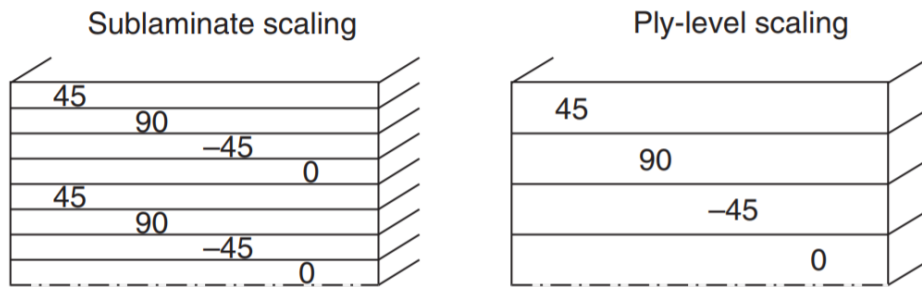


Figure A.1: Sublaminates and ply-level scaling [34]

Table A.1: Description of Experimentally tested Notched Panels

No.	Width [mm]	Layup [°]	Ply t [mm]	n	m	Lamin t [mm]	Hole D [mm]	Strength [MPa]
1	31.75	$[45_n/90_n/-45_n/0_n]_{ms}$	0.125	2	1	2	6.35	373
2	31.75	$[45_n/90_n/-45_n/0_n]_{ms}$	0.125	1	2	2	6.35	338
3	31.75	$[45_n/90_n/-45_n/0_n]_{ms}$	0.125	4	1	4	6.35	424
4	31.75	$[45_n/90_n/-45_n/0_n]_{ms}$	0.125	1	4	4	6.35	351
5	127	$[45_n/90_n/-45_n/0_n]_{ms}$	0.125	4	1	4	25.4	288
6	127	$[45_n/90_n/-45_n/0_n]_{ms}$	0.125	1	4	4	25.4	285
7	127	$[45_n/90_n/-45_n/0_n]_{ms}$	0.125	8	1	8	25.4	263
8	127	$[45_n/90_n/-45_n/0_n]_{ms}$	0.125	1	8	8	25.4	284

The ply properties correspond to that of the **IM7/8552** unidirectional laminate and the material parameters. The properties are collected from [46] [59] are given in table A.2. Note that the strength and stiffness properties in table A.2 are slightly lower than those provided by the manufacturer Hexcel Composite Ltd. [55] but higher than the average values provided by Wichita State University [30].

Table A.2: Ply material properties [46]

E_1	$E_2=E_3$	$G_{12}=G_{13}$	G_{23}	$\mu_{12}=\mu_{13}$	μ_{23}	X_t
150 GPa	11 GPa	4.6 GPa	3.4 GPa	0.3	0.45	2400 MPa
X_c	Y_t	Y_c	$S_{12}=S_{23}$	G_{fc}^t	G_{fc}^c	G_{nc}
1690 MPa	111 MPa	250 MPa	120 MPa	112.7 kJ/m ²	25.9 kJ/m ²	0.2 kJ/m ²
G_{sc}	σ_n^c	$\sigma_s^c = \sigma_t^c$	G_n^c	$\sigma_{fib_{max}}$	η	ρ
1.0 kJ/m ²	40 MPa	50 MPa	0.2 kJ/m ²	5516 MPa	1.0	1.6 [g/cm ³]

The specimens are loaded vertically in compression via a displacement control system progressing with 1 mm/min [46]. For stability concerns, specimens no. 1,2,5,6,7 and 8 have been tested with anti-buckling plates. No side support is used, therefore, with the exception of the top and bottom sides of the panel (that are clamped and only allowed to move vertically), the panel is allowed to move laterally. A depiction of the test setup can be seen in figure A.2. For more information about the test setup, the reader is recommended to read about the ICSTM test fixture [39].

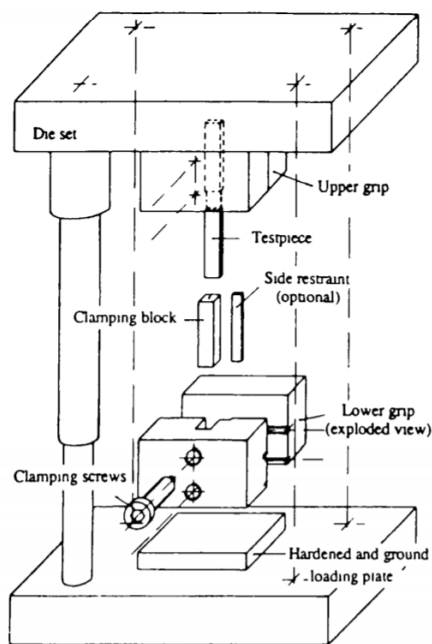


Figure A.2: ICSTM test fixture exploded view [39]

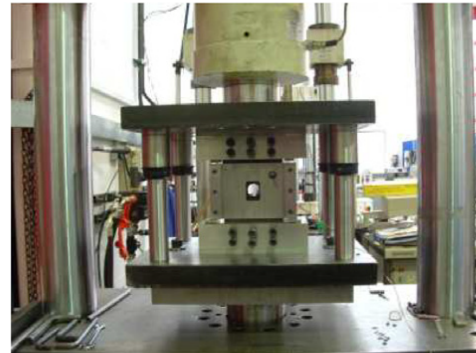


Figure A.3: ICSTM test fixture [39]

Lee et. al. [46], the authors of the OHC experiments reproduced here, mention stability issues were encountered in the 32 mm X 32 mm specimens. Despite using an anti-buckling plate, back to back strain gauges near the hole revealed an out of plane bending that increased with the vertical load (displacement occurring through the window area of the anti-buckling plate depicted in figure A.3). The extra stress around the hole has influenced initial failure and hence the ultimate failure. An exception is made to the 32 mm X 32 mm X 4 mm specimens, discussed in section 6.4 where no bending stresses were found before failure initiation.

B

All Panel Simulation Results

This chapter provides a structured and complete set of results obtained from the FNM based simulations done for the Validation chapter (chapter 6). The three mesh refinement levels mentioned in the section names of this chapter are depicted below.

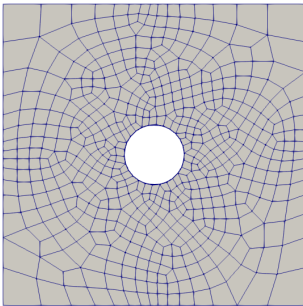


Figure B.1: Coarse Mesh

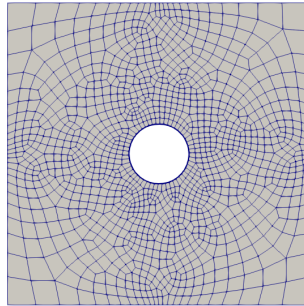


Figure B.2: Original Mesh

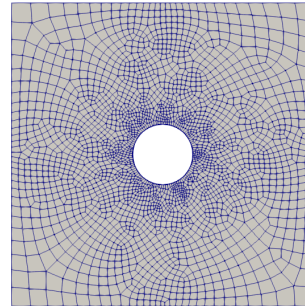


Figure B.3: Refined Mesh

B.1 $31.75 \text{ mm} \times 31.75 \text{ mm} \times 2 \text{ mm}$; $\Delta T=0.005 \text{ s}$; Mesh: Original; Failure Criterion: Maximum Stress

This Floating Node Method based simulation used the maximum stress failure criterion to model fiber failure.

Strength prediction

σ_{test} [MPa]	$\sigma_{\text{simulation}}$ [MPa]
373	423

Fiber Damage

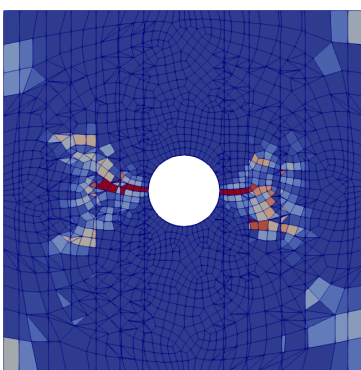


Figure B.4: Fiber damage 0° ply at failure onset

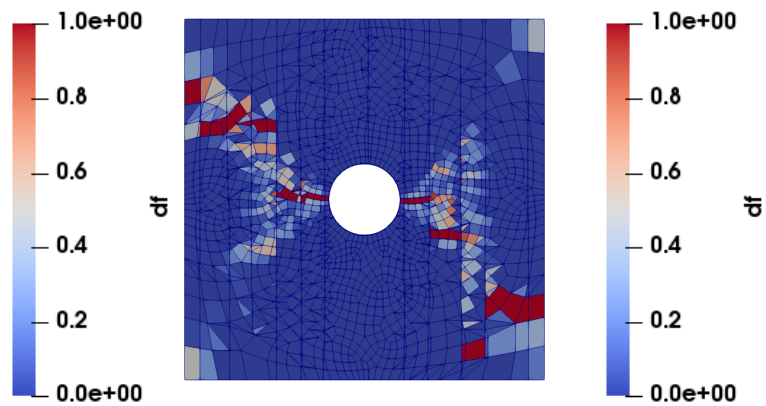


Figure B.5: Fiber damage 0° ply in post failure state

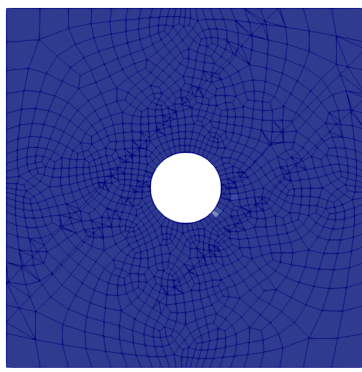


Figure B.6: Fiber damage 45° ply at failure onset

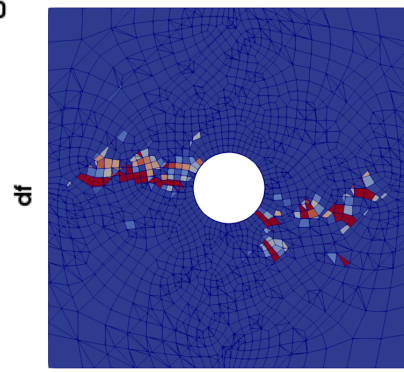
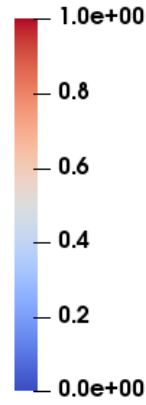
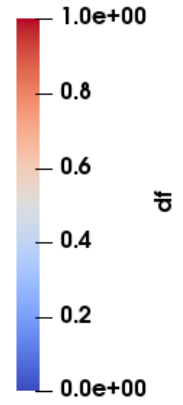


Figure B.7: Fiber damage 45° ply in post failure state



Delamination and Splits

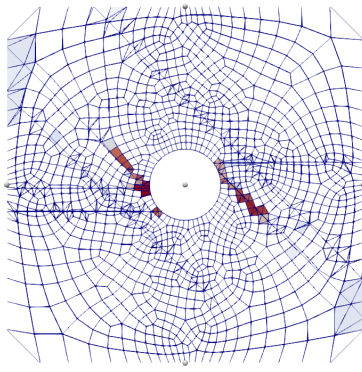


Figure B.8: Delamination 45°/90° interface at failure onset

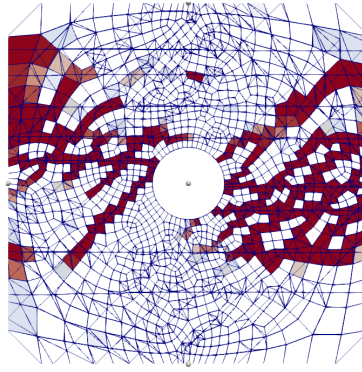
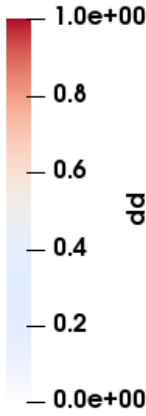


Figure B.9: Delamination 45°/90° interface in post failure state

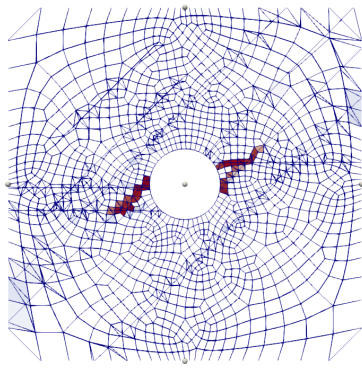
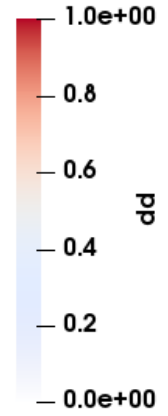


Figure B.10: Delamination 90°/-45° interface at failure onset

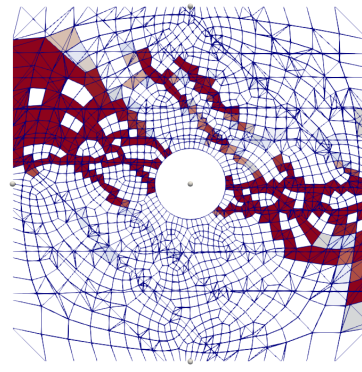
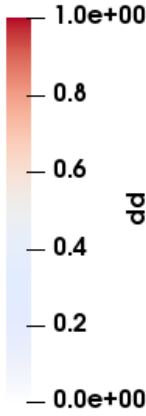
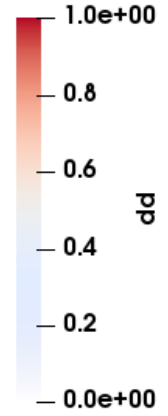


Figure B.11: Delamination 90°/-45° interface in post failure state



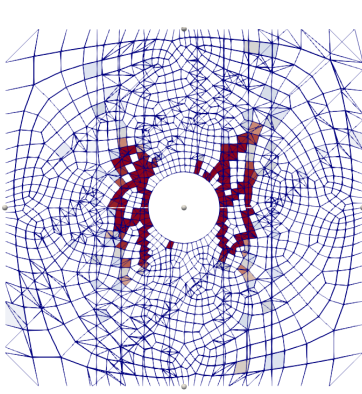


Figure B.12: Delamination -45°/0° interface at failure onset

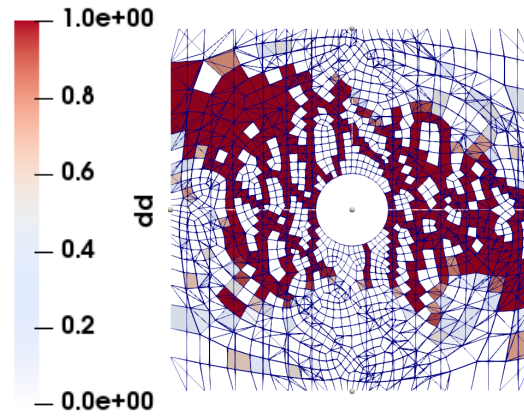


Figure B.13: Delamination -45°/0° interface in post failure state

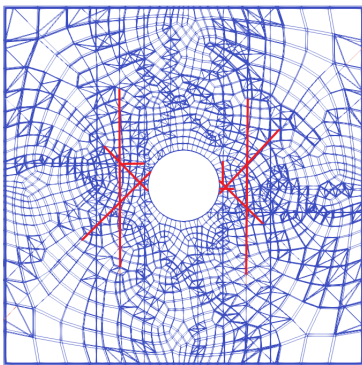


Figure B.14: Matrix splits at failure onset

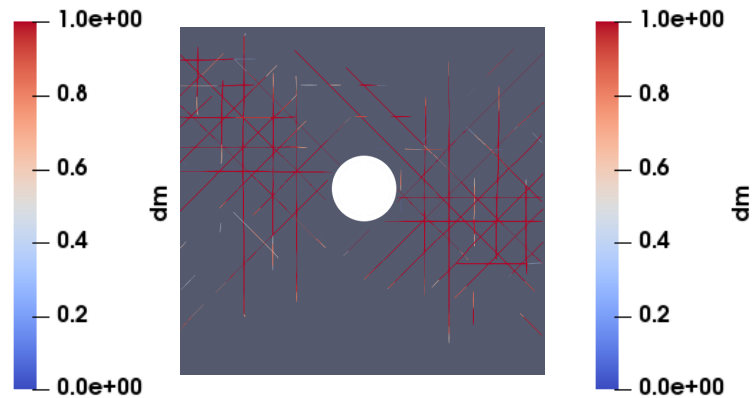


Figure B.15: Matrix splits in post failure state

B.2 31.75 mm × 31.75 mm × 2 mm; Δ T=0.005 s; Mesh: Original; Failure Criterion: Proposed Method

Strength Prediction

σ_{test} [MPa]	$\sigma_{simulation}$ [MPa]
373	404

Fiber Damage

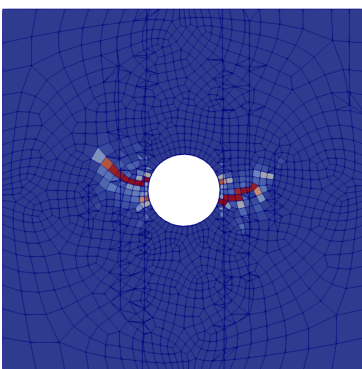


Figure B.16: Fiber damage 0° ply at failure onset

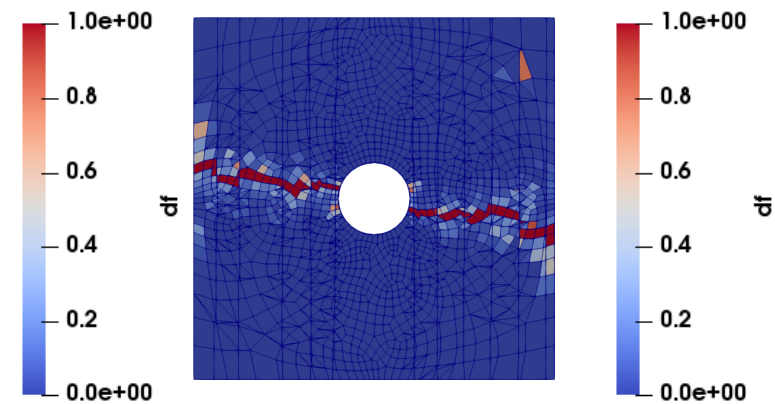


Figure B.17: Fiber damage 0° ply in post failure state

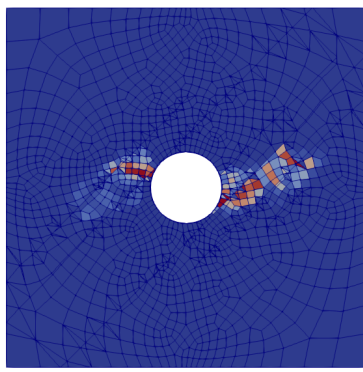


Figure B.18: Fiber damage 45° ply at failure onset

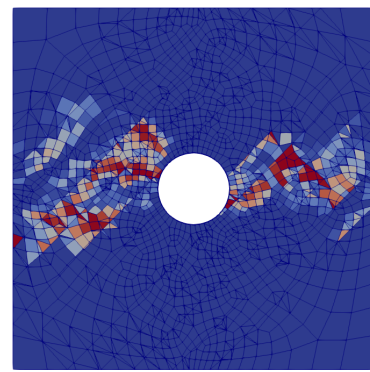
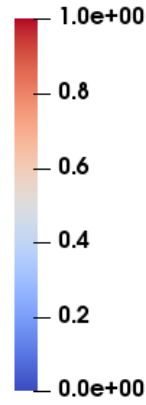
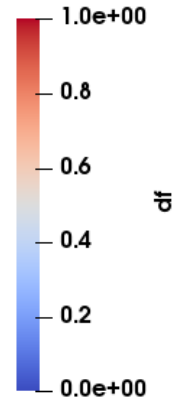


Figure B.19: Fiber damage 45° ply in post failure state



Delamination and Splits

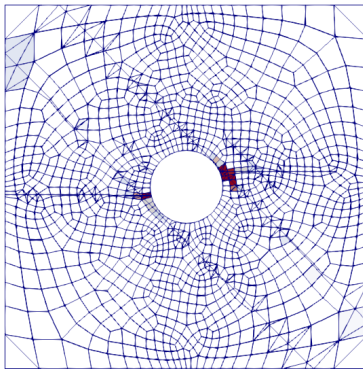


Figure B.20: Delamination 45°/90° interface at failure onset

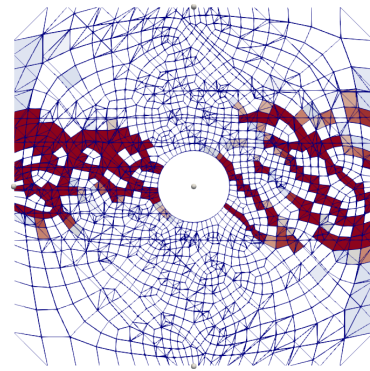
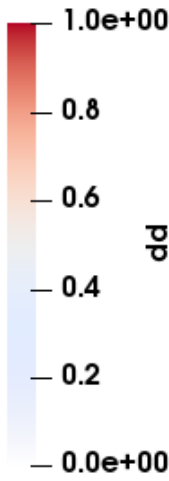


Figure B.21: Delamination 45°/90° interface in post failure state

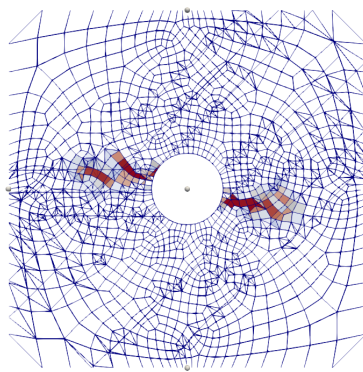
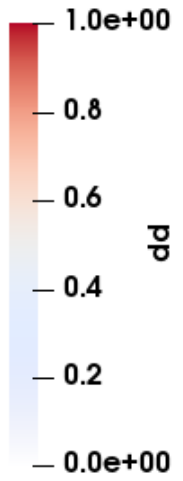


Figure B.22: Delamination 90°/-45° interface at failure onset

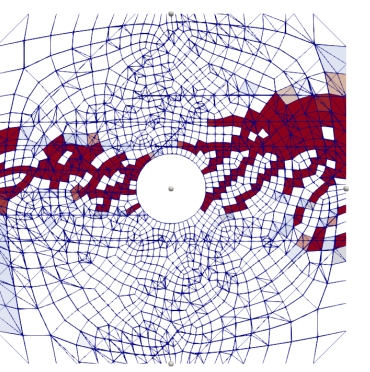
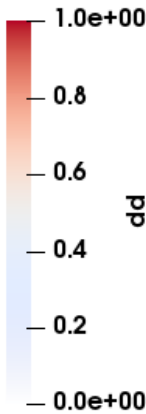
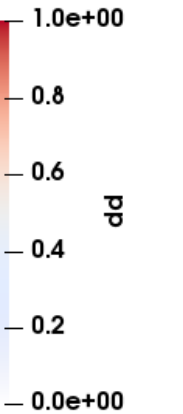


Figure B.23: Delamination 90°/-45° interface in post failure state



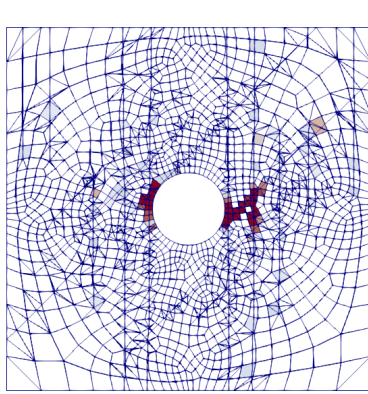


Figure B.24: Delamination -45°/0° interface at failure onset

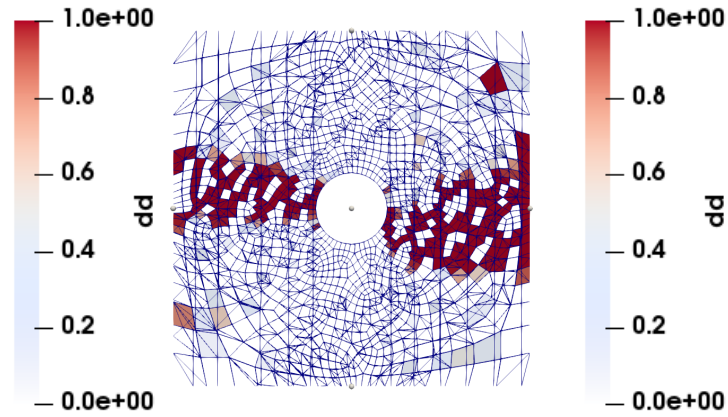


Figure B.25: Delamination -45°/0° interface in post failure state

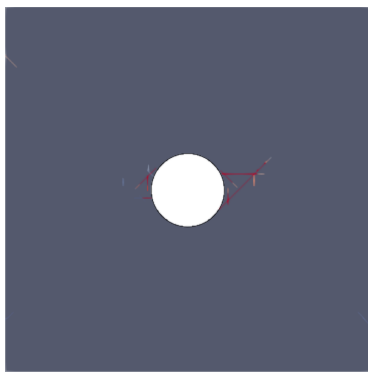


Figure B.26: Matrix splits at failure onset

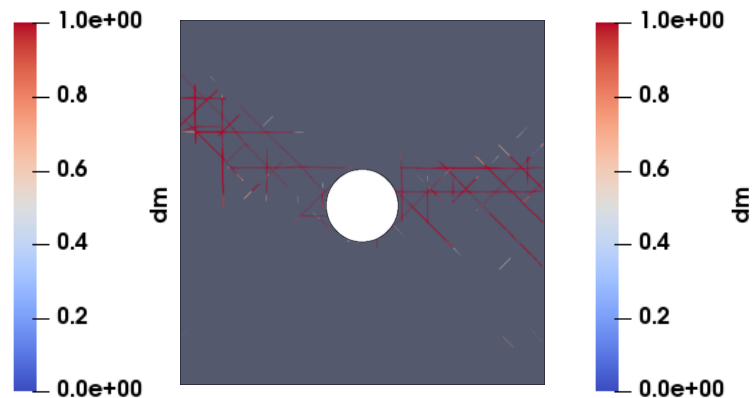


Figure B.27: Matrix splits in post failure state

B.3 31.75 mm × 31.75 mm × 2 mm; Δ T=0.005 s; Mesh: Coarse; Failure Criterion: Proposed Method

Strength prediction

σ_{test} [MPa]	$\sigma_{simulation}$ [MPa]
373	378

Fiber Damage

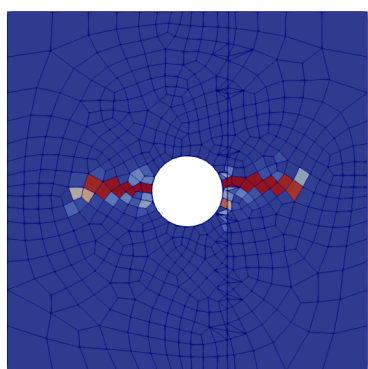


Figure B.28: Fiber damage 0° ply at failure onset

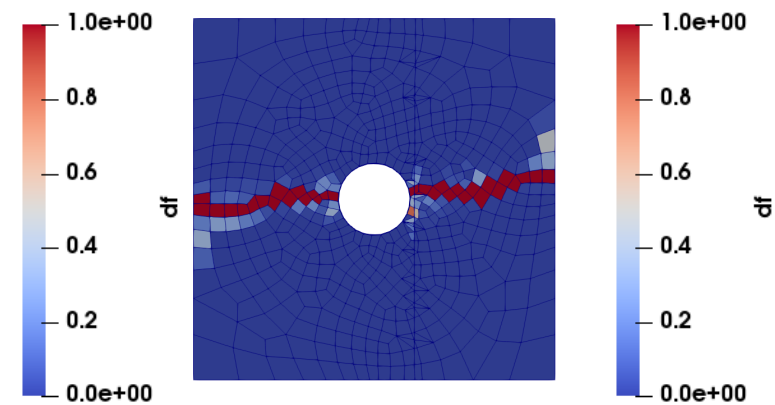


Figure B.29: Fiber damage 0° ply in post failure state

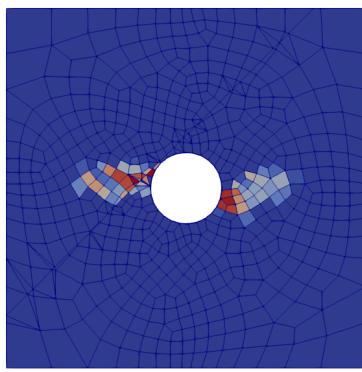


Figure B.30: Fiber damage 45° ply at failure onset

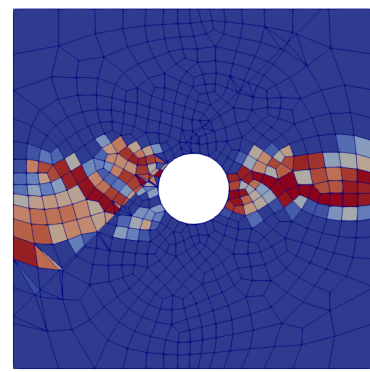
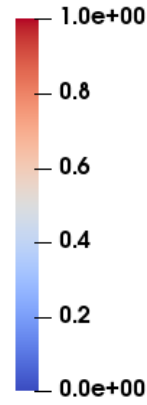
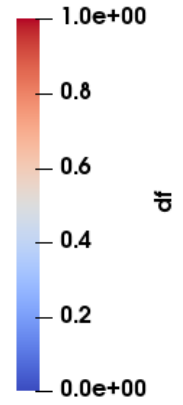


Figure B.31: Fiber damage 45° ply in post failure state



Delamination and Splits

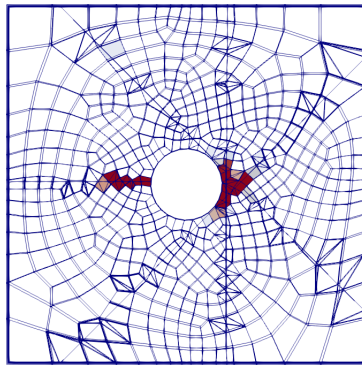


Figure B.32: Delamination all interfaces at failure onset

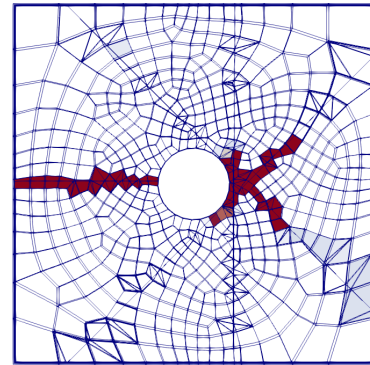
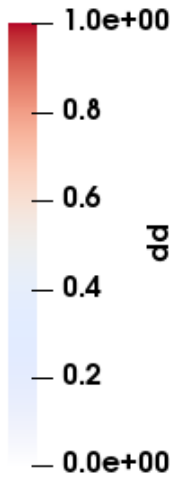


Figure B.33: Delamination all interfaces in post failure state

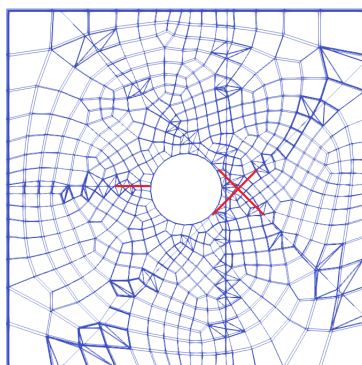
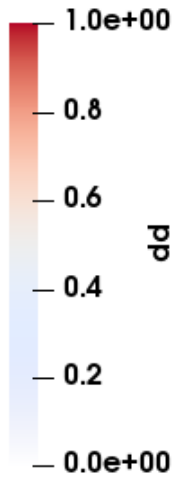


Figure B.34: Matrix splits at failure onset

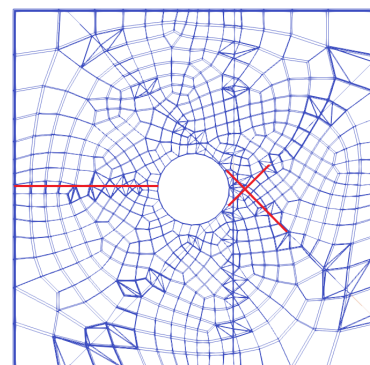
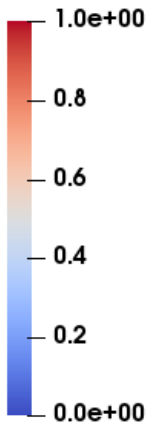
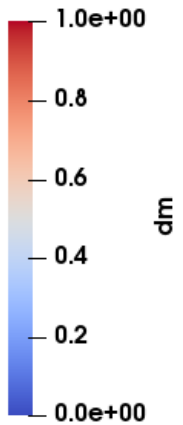


Figure B.35: Matrix splits in post failure state



B.4 31.75 mm × 31.75 mm × 2 mm; Δ T=0.005 s; Mesh: Refined; Failure Criterion: Proposed Method

Strength prediction

σ_{test} [MPa]	$\sigma_{simulation}$ [MPa]
373	384

Fiber Damage

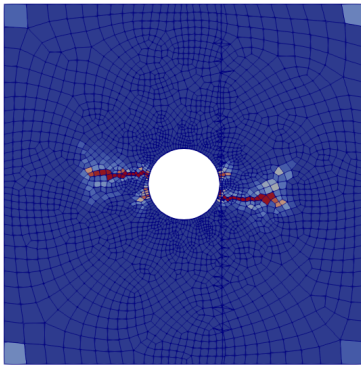


Figure B.36: Fiber damage 0° ply at failure onset

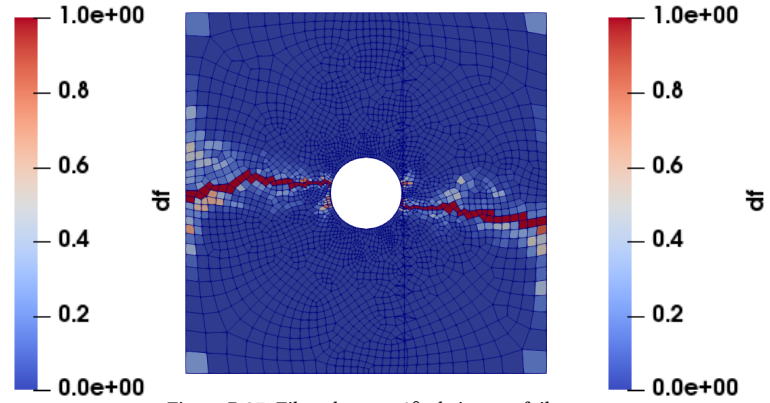


Figure B.37: Fiber damage 0° ply in post failure state

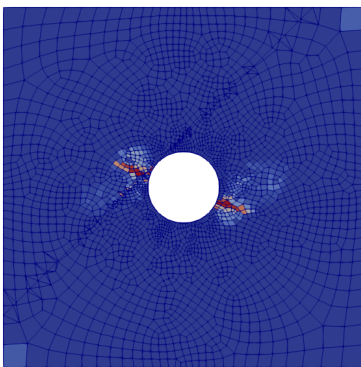


Figure B.38: Fiber damage 45° ply at failure onset

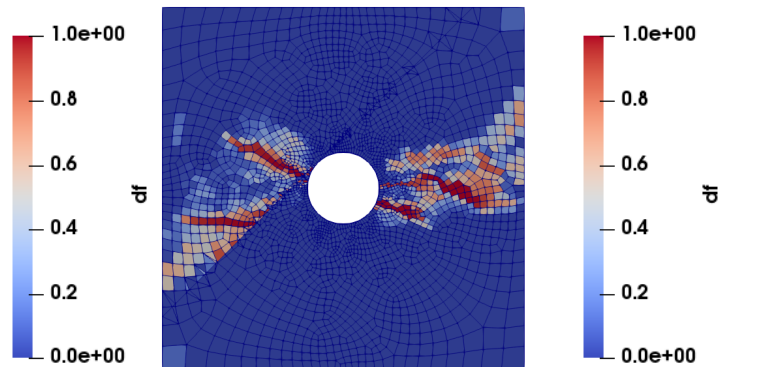


Figure B.39: Fiber damage 45° ply in post failure state

Delamination and Splits

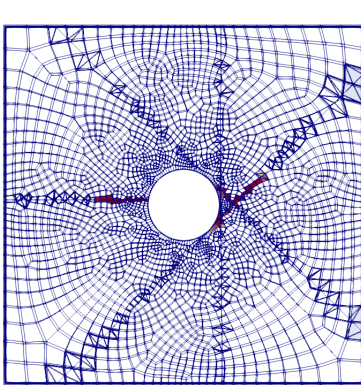


Figure B.40: Delamination all interfaces at failure onset

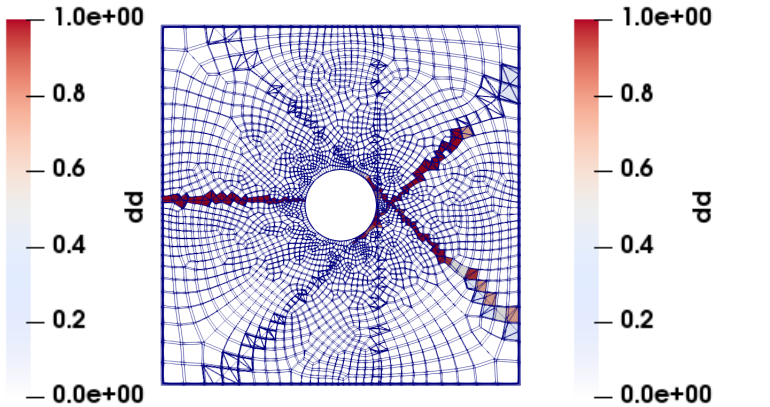


Figure B.41: Delamination all interfaces in post failure state

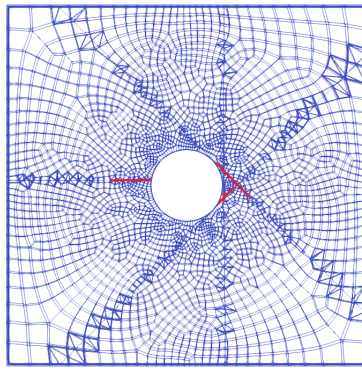


Figure B.42: Matrix splits at failure onset

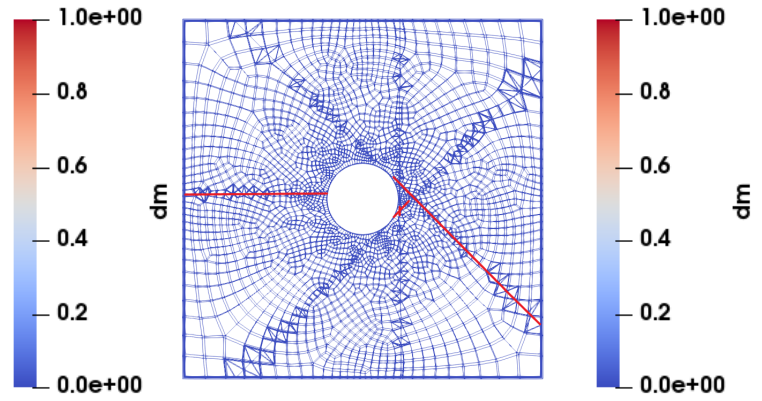


Figure B.43: Matrix splits in post failure state

B.5 31.75 mm × 31.75 mm × 2 mm; $\Delta T=0.025$ s; Mesh: Original; Failure Criterion: Proposed Method Strength prediction

σ_{test} [MPa]	$\sigma_{\text{simulation}}$ [MPa]
373	473

Fiber Damage

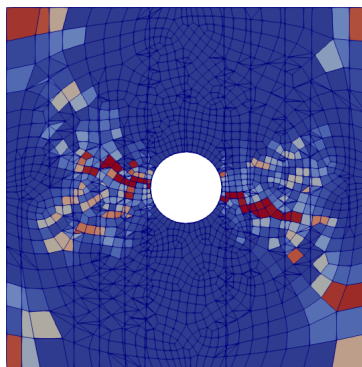


Figure B.44: Fiber damage 0° ply at failure onset

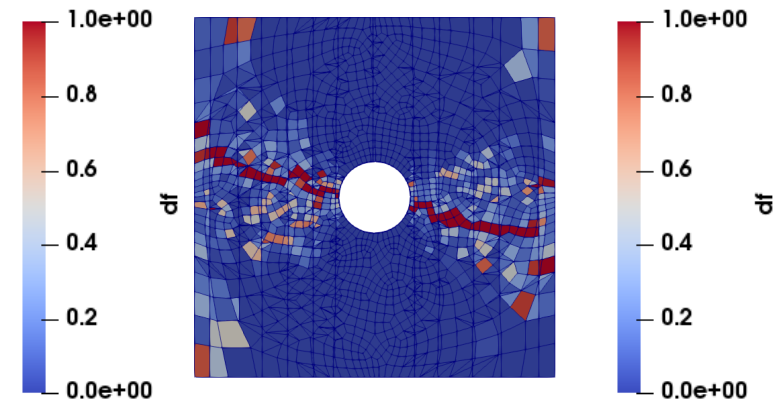


Figure B.45: Fiber damage 0° ply in post failure state

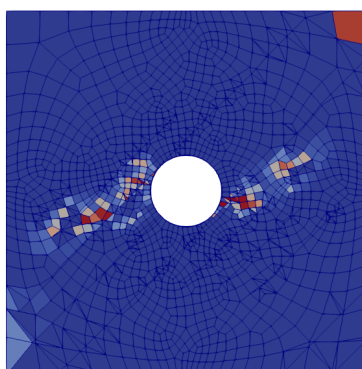


Figure B.46: Fiber damage 45° ply at failure onset

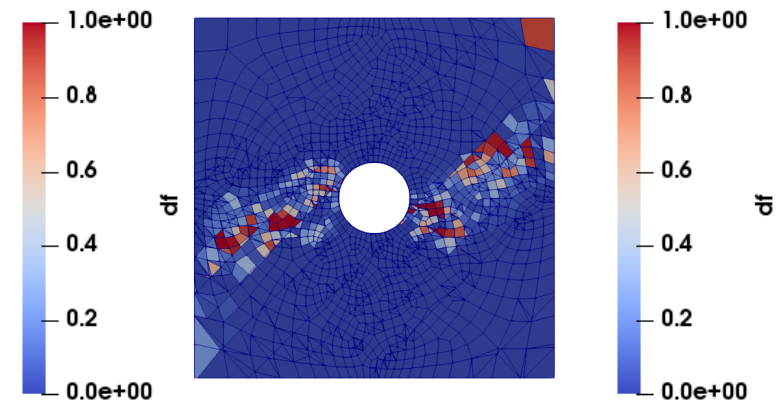


Figure B.47: Fiber damage 45° ply in post failure state

Delamination and Splits

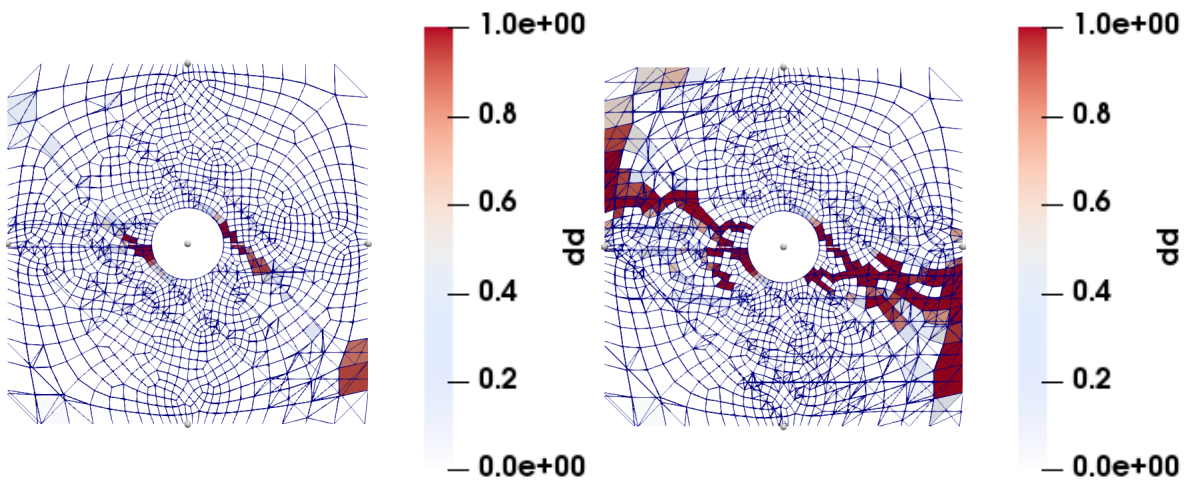


Figure B.48: Delamination 45°/90° interface at failure onset

Figure B.49: Delamination 45°/90° interface in post failure state

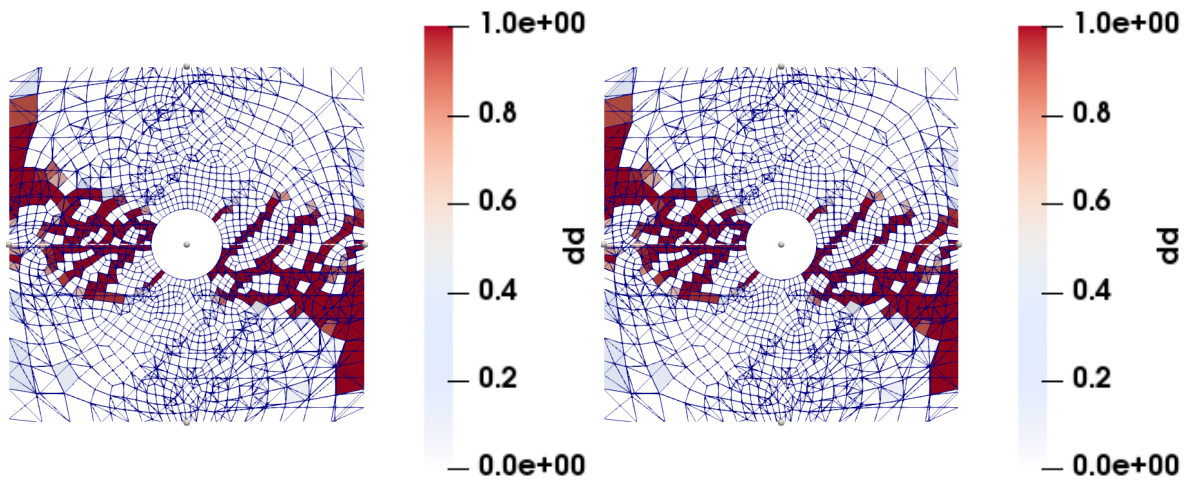


Figure B.50: Delamination 90°/-45° interface at failure onset

Figure B.51: Delamination 90°/-45° interface in post failure state

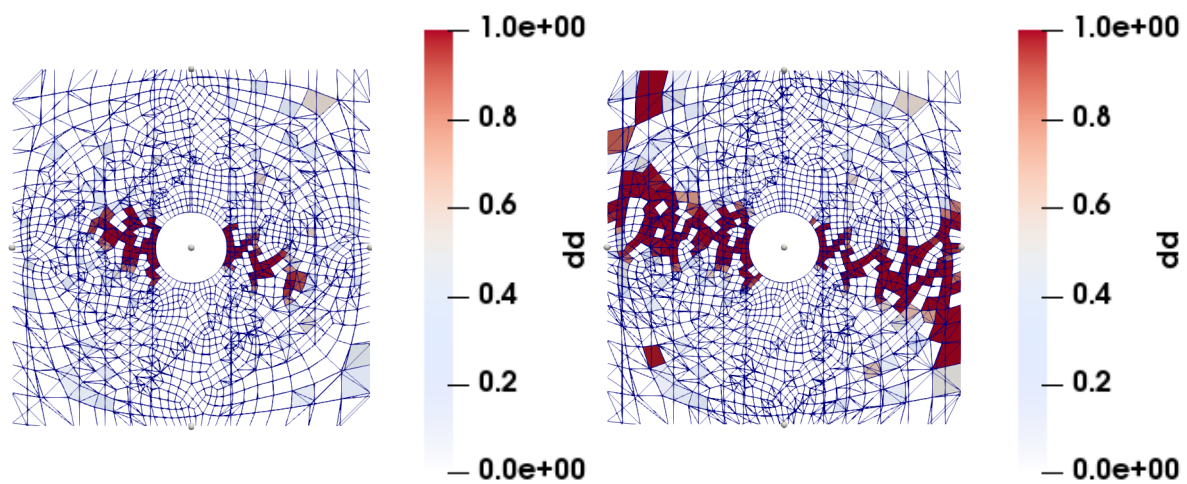


Figure B.52: Delamination -45°/0° interface at failure onset

Figure B.53: Delamination -45°/0° interface in post failure state

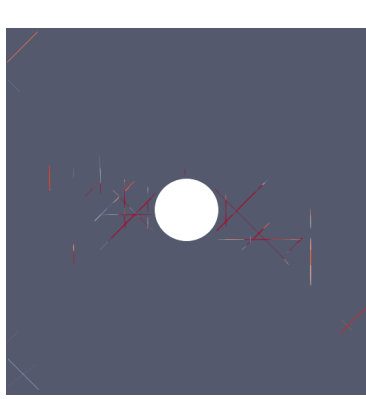


Figure B.54: Matrix splits at failure onset

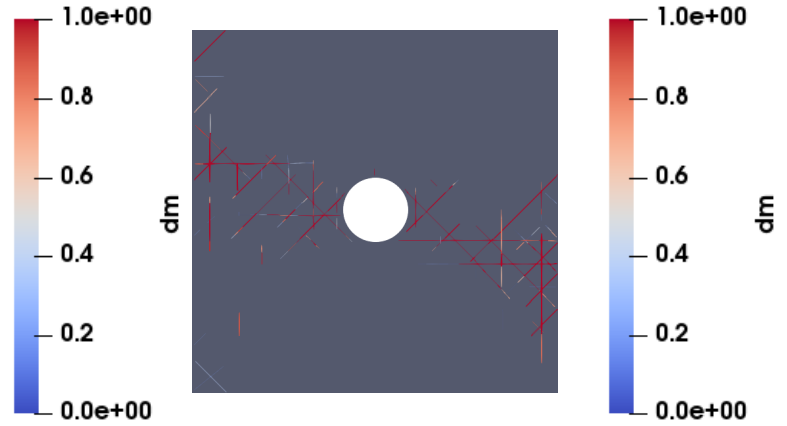


Figure B.55: Matrix splits in post failure state

B.6 $31.75 \text{ mm} \times 31.75 \text{ mm} \times 2 \text{ mm}$; $\Delta T=0.001 \text{ s}$; Mesh: Original; Failure Criterion: Proposed Method

Strength prediction

σ_{test} [MPa]	$\sigma_{\text{simulation}}$ [MPa]
373	394

Fiber Damage

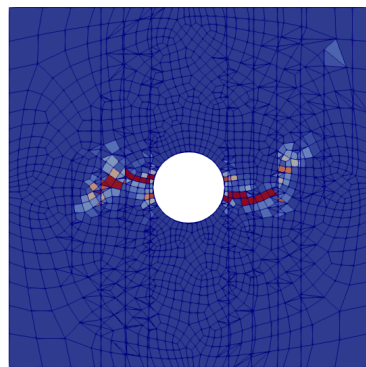


Figure B.56: Fiber damage 0° ply at failure onset

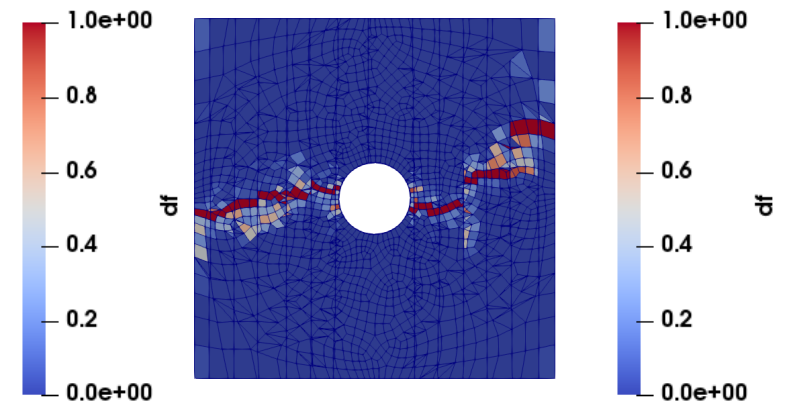


Figure B.57: Fiber damage 0° ply in post failure state

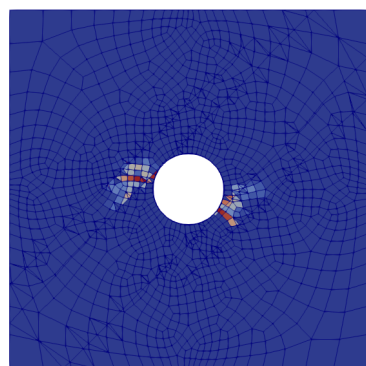


Figure B.58: Fiber damage 45° ply at failure onset

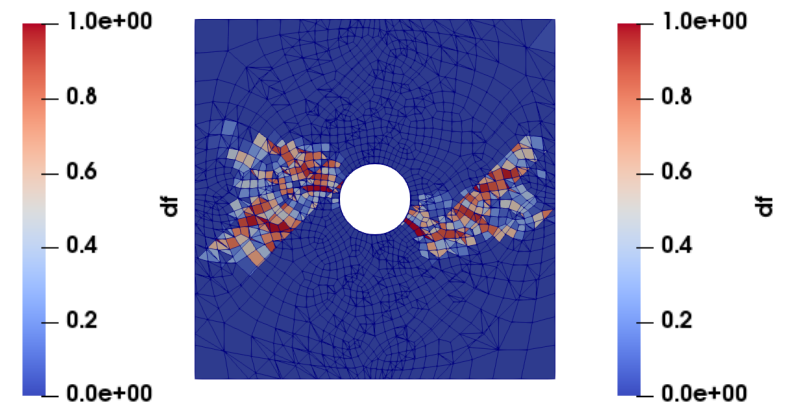


Figure B.59: Fiber damage 45° ply in post failure state

Delamination and Splits

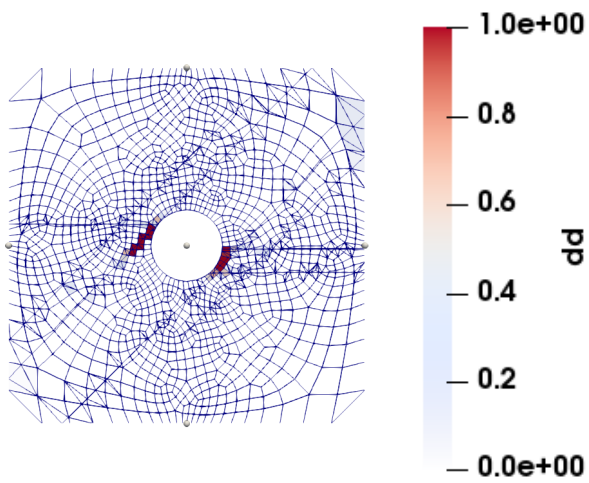


Figure B.60: Delamination 45°/90° interface at failure onset

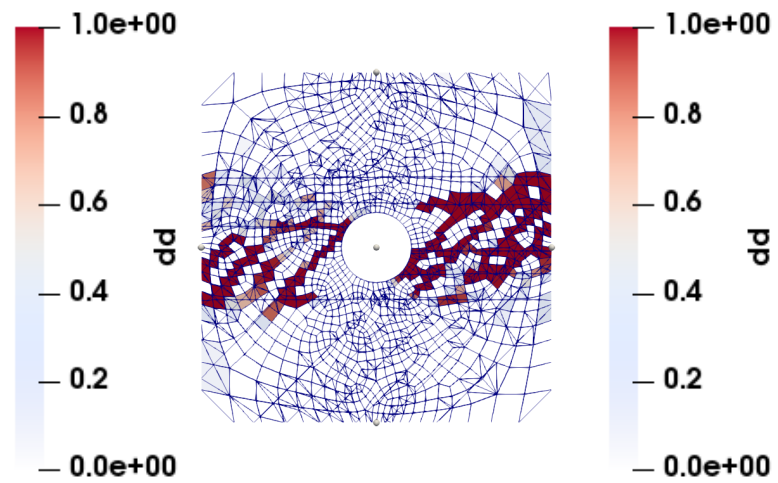


Figure B.61: Delamination 45°/90° interface in post failure state

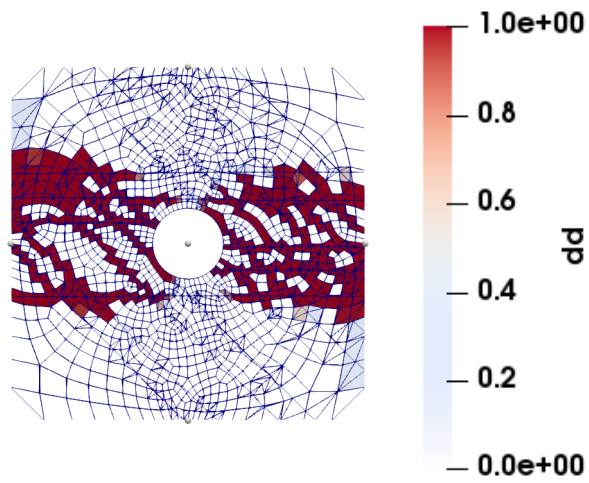


Figure B.62: Delamination 90°/-45° interface at failure onset

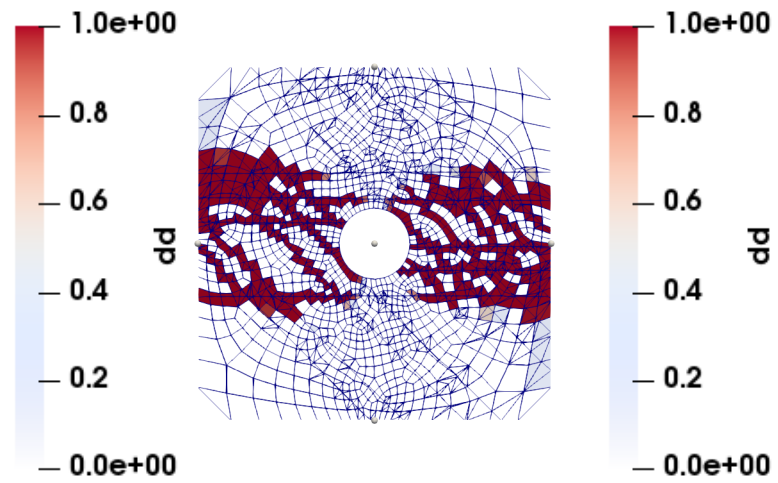


Figure B.63: Delamination 90°/-45° interface in post failure state

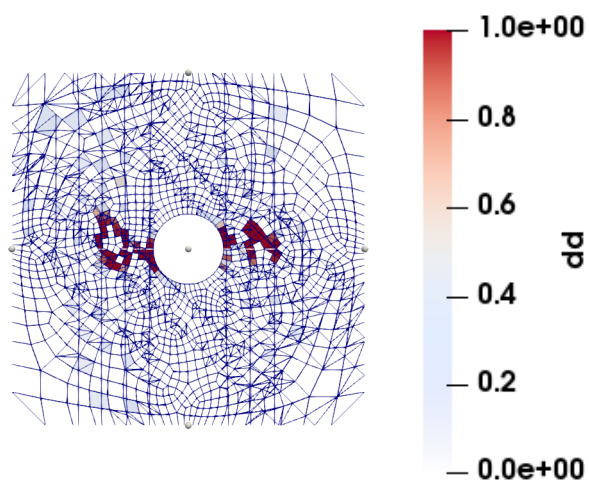


Figure B.64: Delamination -45°/0° interface at failure onset

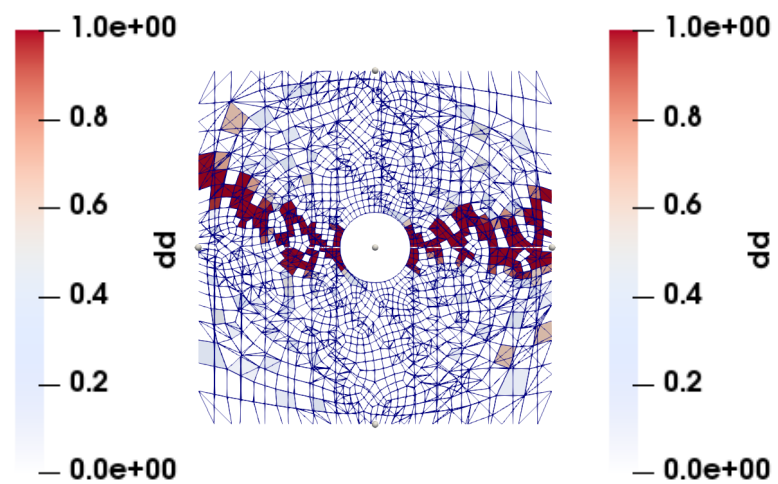


Figure B.65: Delamination -45°/0° interface in post failure state

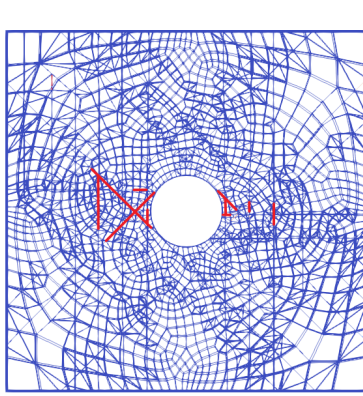


Figure B.66: Matrix splits at failure onset

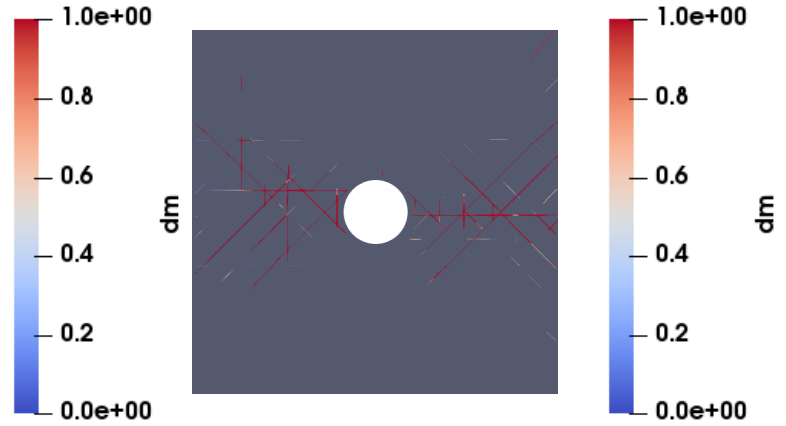


Figure B.67: Matrix splits in post failure state

B.7 31.75 mm × 31.75 mm × 4 mm; $\Delta T=0.005$ s; Mesh: Original; Failure Criterion: Proposed Method

Strength prediction

σ_{test} [MPa]	$\sigma_{\text{simulation}}$ [MPa]
424	445

Fiber Damage

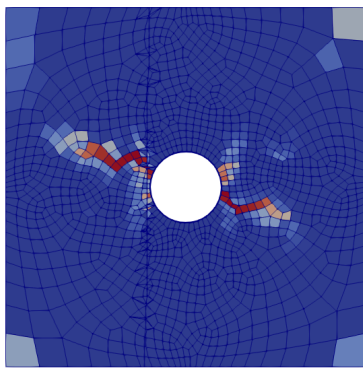


Figure B.68: Fiber damage 0° ply at failure onset

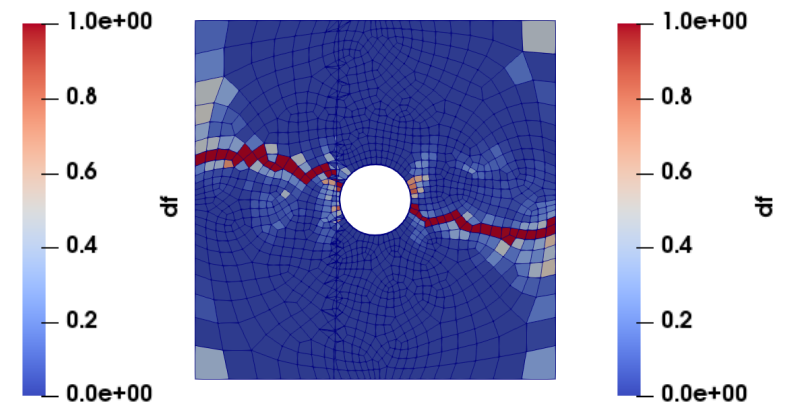


Figure B.69: Fiber damage 0° ply in post failure state

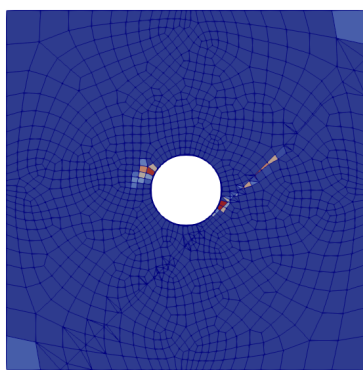


Figure B.70: Fiber damage 45° ply at failure onset

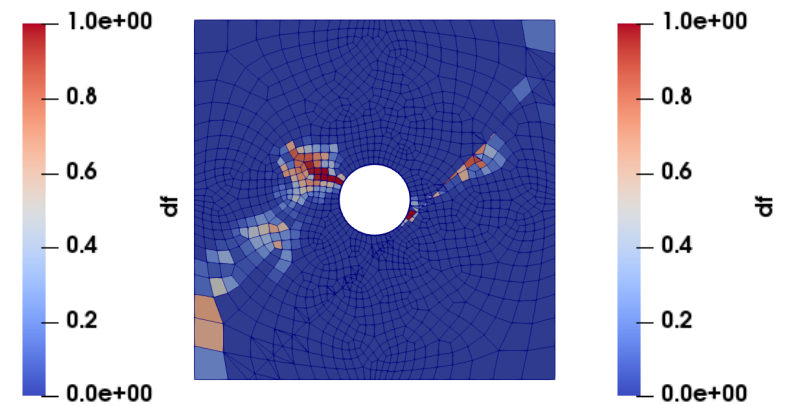


Figure B.71: Fiber damage 45° ply in post failure state

Delamination and Splits

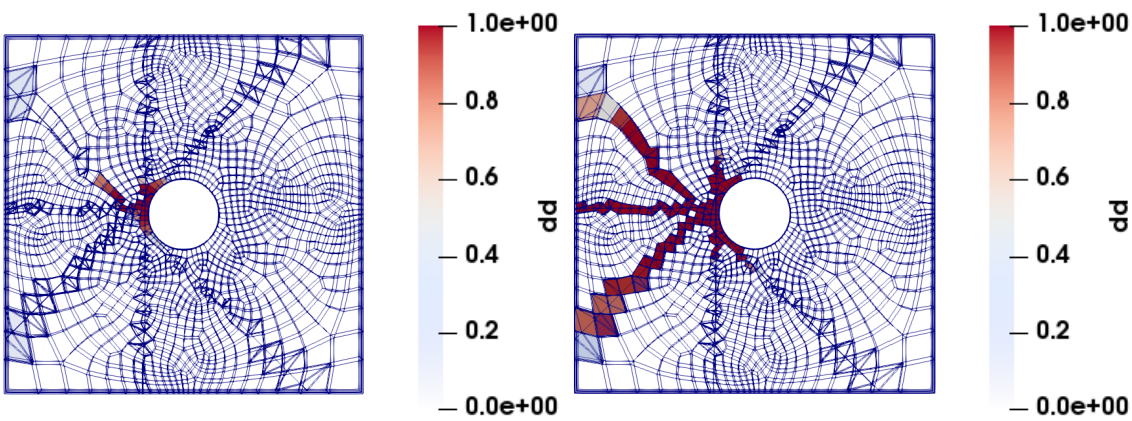


Figure B.72: Delamination all interfaces at failure onset

Figure B.73: Delamination all interfaces in post failure state

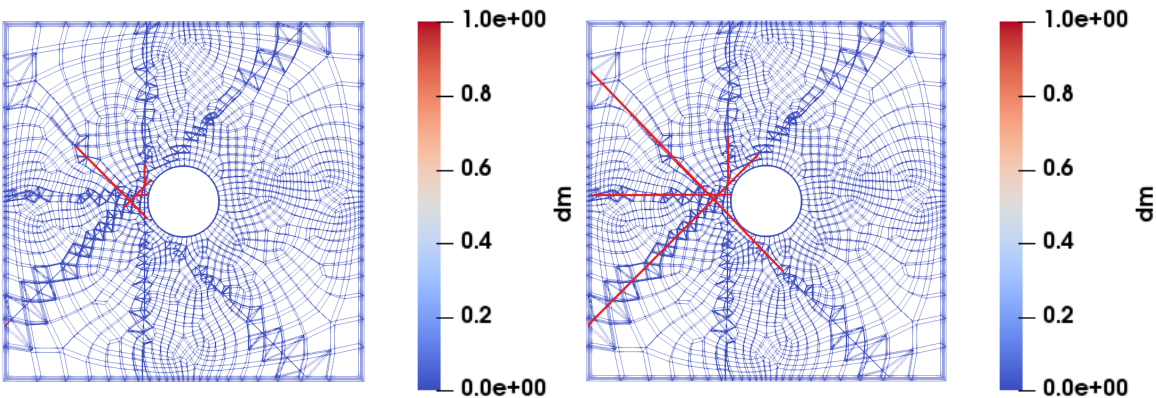


Figure B.74: Matrix splits at failure onset

Figure B.75: Matrix splits in post failure state

B.8 127 mm × 127 mm × 4 mm; Δ T=0.005 s; Failure Criterion: Proposed Method Strength prediction

σ_{test} [MPa]	$\sigma_{simulation}$ [MPa]
288	313

Fiber Damage

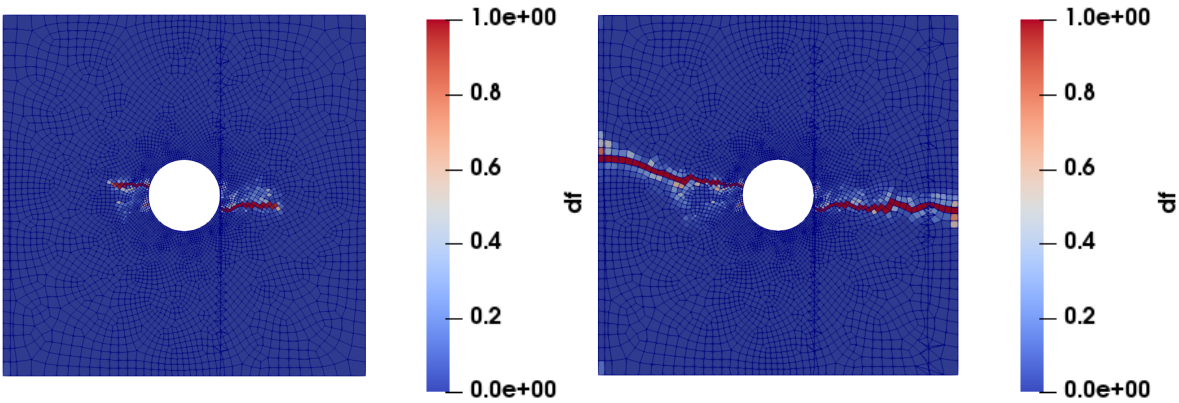


Figure B.76: Fiber damage 0° ply at failure onset

Figure B.77: Fiber damage 0° ply in post failure state

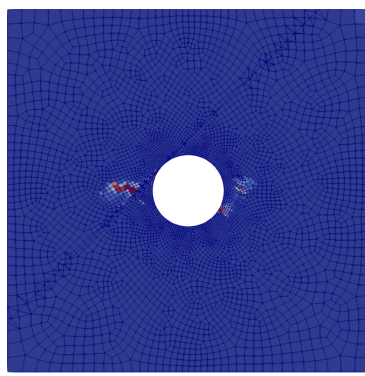


Figure B.78: Fiber damage 45° ply at failure onset

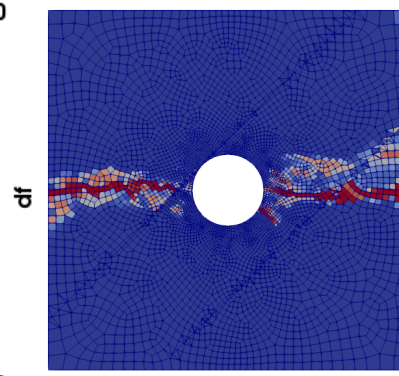
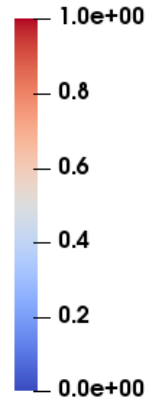
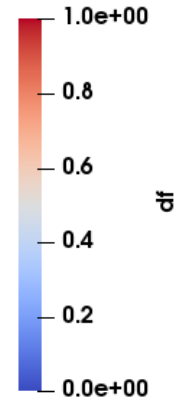


Figure B.79: Fiber damage 45° ply in post failure state



Delamination and Splits

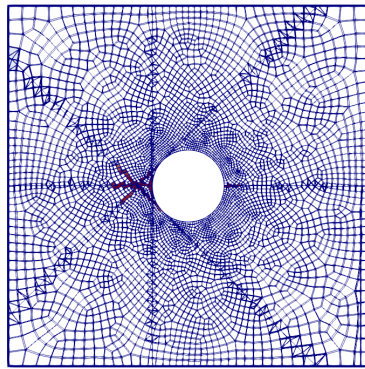


Figure B.80: Delamination all interfaces at failure onset

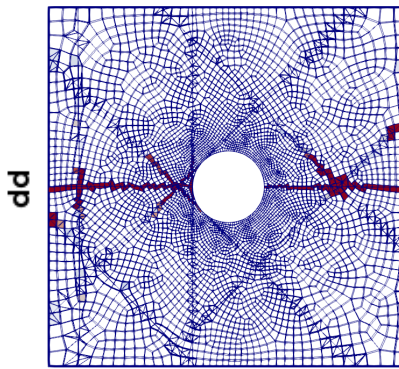
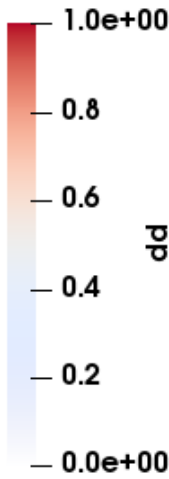


Figure B.81: Delamination all interfaces in post failure state

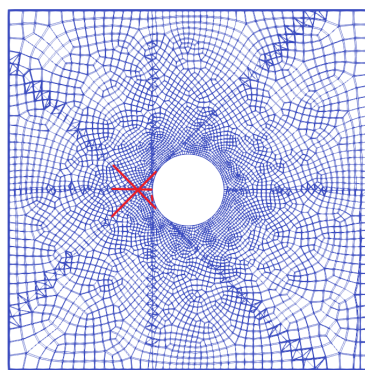
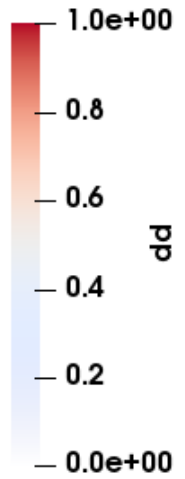


Figure B.82: Matrix splits at failure onset

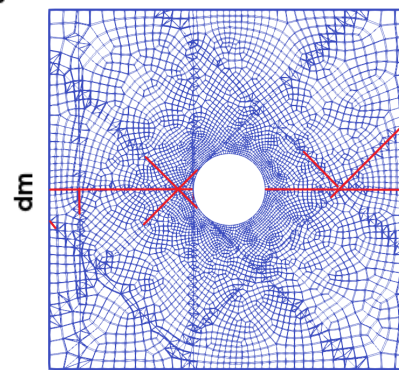
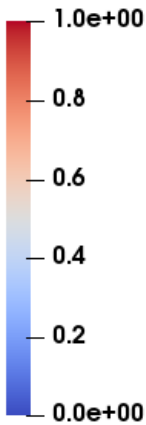
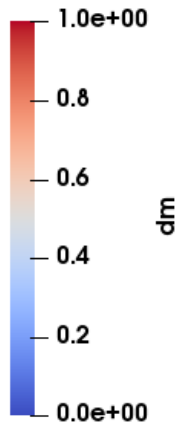


Figure B.83: Matrix splits in post failure state



Bibliography

- [1] Jumahat A., Soutis C., Jones F.R., and Hodzic A. Fracture mechanisms and failure analysis of carbon fibre/toughened epoxy composites subjected to compressive loading. *Composite Structures*, 92:295–305, 2010.
- [2] Puck A and Schürmann H. Failure analysis of frp laminates by means of physically based phenomenological models. *Composites Science and Technology*, 58:1045–1067, 1998.
- [3] P.M.A. Areias, J.H. Song, and T. Belytschko. Analysis of fracture in thin shells by overlapping paired elements. *Computational Methods Applied Mechanical Engineering*, 195(41-43):5343–5360, 2006.
- [4] A. A. Argon. Fracture of composites in: treatise on material science and technology. *Academic Press and New York*, 1972.
- [5] Zdeněk P. Bažant. Size effect. *Journal of Solids and Structures*, 37:69–80, 2000.
- [6] Z. Bažant, J.J. Kim, I. Daniel, E. Becq-Giraudon, and G. Zi. *Size effect on compression strength of fiber composites failing by kink band propagation*. Springer, 3 edition, 1999.
- [7] Andrew C. Bergan and Frank A. Leone Jr. A continuum damage mechanics model to predict kink-band propagation using deformation gradient tensor decomposition friction. Technical Report 106, NASA Langley Research Center, Dayton, Ohio, USA, September 2016. URL <https://ntrs.nasa.gov/search.jsp?R=20160012045>.
- [8] Andrew C. Bergen, Miguel Herraiez, Carlos Gonzalez, and Claudio S. Lopes. Development of a mesoscale finite element constitutive model for fiber kinking. *Structures, Structural Dynamics and Materials Conference*, 1221, 2018. URL <https://arc.aiaa.org/doi/abs/10.2514/6.2018-1221>.
- [9] Thomas Bru, Peter Hellström, Renaud Gutkin, Dimitra Ramantani, and Göran Peterson. Characterisation of the mechanical and fracture properties of a uni-weave carbon fibre/epoxy non-crimp fabric composite. *Data in Brief*, 6:680–695, 2016.
- [10] B. Budiansky and N. Fleck. Compressive failure of fiber composites. *Journal of the Mechanics and Physics of Solids*, 41(1):183–211, 1993.
- [11] B. Budiansky, N. A. Fleck, and J. C. Amazigo. On kink-band propagation in fiber composites. *Journal of the Mechanics and Physics of Solids*, 46:1637–1653, 1998.
- [12] B.P. Bussadori, K. Schuffenhauer, and A. Scattina. Modelling of cfrp crushing structures in explicit crash analysis. *Composites: Part B*, 60:725–735, 2014.
- [13] P.P. Camanho, P. Maimi, and C.G. Davila. Prediction of size effects in notched laminates using continuum damage mechanics. *Composites Science and Technology*, 67:2715–2727, 2007.
- [14] G. Cantalanotti, P.P. Camanho, J. Xavier, C.G. Dávila, and A.T. Marques. Measurement of resistance curve in the longitudinal failure of composites using digital image correlation. *Composites Science and Technology*, 70(13):1986–93, 2010.
- [15] N.V. De Carvalho, B.Y. Chen, S.T. Pinho, J.G. Ratcliffe, P.M. Baiz, and T.E. Tay. Modeling delamination migration in cross-ply tape laminates. *Composites, Part A*(71):192–203, 2015.
- [16] G. Catalanotti, P.P. Camanho, and A.T. Marques. Three-dimensional failure criteria for fiber-reinforced laminates. *Composite Structures*, 95:63–79, 2012.
- [17] Dávila CG, Camanho PP, and Rose CA. Failure criteria for frp laminates. *Journal of Composite Materials*, 39(4):323–345, 2005.

- [18] B.Y. Chen and T.E. Tay. *The Structural Integrity of Carbon Fiber Composites*. Springer, 2016.
- [19] B.Y. Chen, T.E. Tay, P.M. Baiz, and S.T. Pinho. Numerical analysis of size effects on open-hole tensile composite laminates. *Composites, Part A*(47):52–62, 2013.
- [20] B.Y. Chen, S.T. Pinho, N.V. De Carvalho, P.M. Baiz, and T.E. Tay. A floating node method for the modelling of discontinuities in composites. *Engineering Fracture Mechanics*, 127:104–134, 2014.
- [21] B.Y. Chen, T.E. Tay, S.T. Pinho, and V.B.C. Tan. Modelling the tensile failure of composites with the floating node method. *Computer Methods in applied mechanics and engineering*, 308:414–442, 2016.
- [22] HEXCEL Corporation. Hextow® im7 data sheet, 2018. URL https://www.hexcel.com/user_area/content_media/raw/IM7_HexTow_DataSheet.pdf.
- [23] Sérgio Costa. *Physically based fibre kinking model for crash of composites*. PhD thesis, Chalmers University of Technology, 2016.
- [24] J. MICHAEL STARBUCKDANIEL O. ADAMSMARC COURTEAU. Energy absorbing damage mechanisms in progressive crushing of composite tubes. *Conference: American Society for Composites*, (433), 2017.
- [25] B. Rene R. R. da Costa. Modeling of fiber kinking in composite laminates. Technical report, Delft University of Technology, 12 2015.
- [26] G.J. Dvorak and N. Laws. Analysis of progressive matrix cracking in composite laminates ii. first ply failure. *Journal of Composite Materials*, 21:309–329, 1987.
- [27] Carlos G. Dávila and Pedro P. Camanho. A procedure for superposing linear cohesive laws to represent multiple damage mechanisms in the fracture of composites. *International Journal of Fracture*, 158(2): 211–223, 2009.
- [28] E.Giner, N. Sukumar, J.E. Tاراçon, and E.J. Fuenmayor. An abaqus implementation of the extended finite element method. *Engineering Fracture Mechanics*, 76(3):347–368, 2009.
- [29] N.A. Fleck, L. Deng, and B. Budiansky. Prediction of kink width in compressed fiber composites. *Journal of Applied Mechanics*, 62(2):329–337, 1995.
- [30] National Center for Advanced Materials Performance Wichita State University. *Product Data Sheet*, 2011. URL https://www.niar.wichita.edu/coe/ncamp_documents/Hexcel%208552/NMS%20128%20slash%20%20Rev%20A%20June%2021%202011%20Hexcel%208552%20IM7.pdf.
- [31] S.P. Garbo and J.M. Ogonowski. Effect of variances and manufacturing tolerances on the design strength and life of mechanically fastened composite joints. Technical Report A101657, McDonnell Aircraft Company, St. Louis, Missouri 65166, April 1981. URL <http://www.dtic.mil/dtic/tr/fulltext/u2/a101657.pdf>.
- [32] W. Gerberich and W. Yang. *Comprehensive Structural Integrity*. Elsevier, 2003.
- [33] G.I. Barenblatt. The mathematical theory of equilibrium cracks in brittle fracture. *Advances in Applied Mathematics*, 7:55–129, 1962.
- [34] B.G. Green, M.R. Wisnom, and S.R. Hallet. An experimental investigation into the tensile strength scaling of notched composites. *Composites, Part A*(38):867–878, 2007.
- [35] P. Robinson E. Greenhalgh and S. Pinho. *Failure Mechanisms in Polymer Matrix Composites*. Woodhead Publishing Series in Composites Science and Engineering, 1 edition, 2012.
- [36] R. Gutkin and Silvestre T Pinho. Combining damage and friction to model compressive damage growth in fibre-reinforced composites. *Journal of Composite Materials*, 49(20):2483–2495, 2014.
- [37] R. Gutkin, S.T. Pinho, P. Robinson, and P.T. Curtis. A finite fracture mechanics formulation to predict fibre kinking and splitting in cfrp under combined longitudinal compression. *Mechanics of Materials*, pages 730–739, 2011.

- [38] R. Gutkin, Sergio Costa, and Robin Olsson. A physically based model for kink-band growth and longitudinal crushing of composites under 3d stress states accounting for friction. *Composites Science and Technology*, pages 39–45, 2016.
- [39] J. G. Haberle and F. L. Matthews. An improved technique for compression testing of unidirectional fibre-reinforced plastics; development and results. *Composites*, 25(5):358–371, 1994.
- [40] A. Hansbo and P. Hansbo. Fa finite element method for the simulation of strong and weak discontinuities in solid mechanics. *Computational Methods in Applied Mechanical Engineering*, 193:33–35, 2004.
- [41] P.W. Harper and S.R. Hallet. Cohesive zone length in numerical simulations of composite delamination. *Engineering Fracture Mechanics*, 75(16):4774–4792, 2008.
- [42] A.J. Hodge, A.T. Nettles, and J.R. Jackson. Comparison of open-hole compression strength and compression after impact strength on carbon fiber/epoxy laminates for the ares i composite interstage. *NASA Center for AeroSpace Information*, pages 1–3, 2011. URL <https://ntrs.nasa.gov/archive/nasa/casi.ntrs.nasa.gov/20110008641.pdf>.
- [43] I. Babuška and B.Q. Guo. The h, p and h-p version of the finite element method; basis theory and applications. *Advances in Engineering Software*, 15(3):159–174, 1992.
- [44] J. Dolbow and T. Belytschko. The partition of unity finite element method: Basic theory and applications. *Computer Methods in Applied Mechanics and Engineering*, 139(1):289–314, 1996.
- [45] J. Dolbow and T. Belytschko. A finite element method for crack growth without remeshing. *International Journal for Numerical Methods in Engineering*, 46(1):131–150, 1999.
- [46] J. Lee and C. Soutis. Measuring the notched compressive strength of composite laminates: specimen size effects. *Composites Science and Technology*, 68(12):2359–2366, 2008.
- [47] A. S. Kaddour and M. J. Hinton. Maturity of 3d failure criteria for fibre-reinforced composites: Comparison between theories and experiments: Part b of wwfe-ii. *Journal of Composite Materials*, 47(6-7): 925–966, 2013.
- [48] Christos Kassapoglou. *Modelling the Effect of Damage in Composite Structures*. Wiley, 1 edition, 2015.
- [49] Ronald Krueger. Virtual crack closure technique: History, approach, and applications. *Appl Mech Rev*, 57(2):109–140, 2004.
- [50] Ragnar Larsson, Renaud Gutkin, and Mohammad S. Rouhi. Damage growth and strain localization in compressive loaded fiber reinforced composites. *Mechanics of Materials*, 127:77–90, 2018.
- [51] H.K. Lee and B.R. Kim. Numerical characterization of compressive response and damage evolution in laminated plates containing a cutout. *Composites Science and Technology*, 67:2221–2230, 2007.
- [52] S. H. Lee and Anthony M. Waas. Compressive response and failure of fiber reinforced unidirectional composites. *International Journal of Fracture*, 100(3):275–306, 1999.
- [53] S.G. Lekhnitskii. The theory of elasticity of an anisotropic elastic body (originally: Teoriia uprugosti anisotropnovo tela). *Government Publishing House for Technical Theoretical Works*, 1963.
- [54] F. A. Leone Jr., Bergan A. C., and C. G. Dávila. Compdam - deformation gradient decomposition (dgd), v2.2.0, 2018. https://github.com/nasa/CompDam_DGD.
- [55] Hexcel Composites Ltd. *Product Data Sheet*, 2016. URL https://www.hexcel.com/user_area/content_media/raw/HexPly_8552_eu_DataSheet.pdf.
- [56] P. Maimí, P. P. Camanho, J.-A. Mayugo, and C. G. Dávila. A thermodynamically consistent damage model for advanced composites. Technical Report 214282, NASA Langley Research Center, Dayton, Ohio, USA, September 2006.
- [57] F.P. Van Der Meer and L.J. Sluys. Continuum models for the analysis of progressive failure in composite laminates. *Journal of Composite Materials*, 43(20):2131–2156, 2009.

- [58] W. Michaeli, M. Mannigel, and F. Preller. On the effect of shear stresses on the fibre failure behaviour in cfrp. *Composites Science and Technology*, 69:1354–1357, 2009.
- [59] Laffan MJ, Pinho ST, Robinson P, Iannucci L, and McMillan AJ. Measurement of the fracture toughness associated with the longitudinal fibre compressive failure mode of laminated composites. *Compos Part A-Appl Sci Manuf*, 43(11):1930–1938, 2012.
- [60] M.R.Wisnom, B.Khan, and S.R.Hallett. Size effects in unnotched tensile strength of unidirectional and quasi-isotropic carbon/epoxy composites. *Composite Structures*, 84(1):21–28, 2008.
- [61] Pedro P.Camanho, Carlos G.Dávila, Silvestre T.Pinho, Lorenzo Iannucci, and Paul Robinson. Prediction of in situ strengths and matrix cracking in composites under transverse tension and in-plane shear. *Composites*, 37(2):165–176, 2006.
- [62] S.T. Pinho, L. Iannucci, and P. Robinson. Physically based failure models and criteria for laminated fibre-reinforced composites with emphasis on fibre kinking. part ii: Fe implementation. *Composites:Applied science and manufacturing*, Part A(37):766–777, 2006.
- [63] S.T. Pinho, L. Iannucci, and P. Robinson. Physically-based failure models and criteria for laminated fibre-reinforced composites with emphasis on fibre kinking: part i: development. *Composites Part A- Applied Science and Manufacturing*, 37(1):63–73, 2006.
- [64] S.T. Pinho, R. Gutkin, S. Pimenta, N.D. Carvalho, and P. Robinson. Seven fiber dominated compressive failures in polymer matrix composites. *Failure Mechanisms in Polymer Matrix Composites*, pages 183–223, 2012.
- [65] ST Pinho, GM Vyas, and P Robinson. Material and structural response of polymer-matrix fibre-reinforced composites. *Journal of Composite Materials*, 47(6-7):679–696, 2013.
- [66] Ershad Pourbahaaddini and Philip Simonsson. A comparative study on the modeling of matrix cracking in fiber-reinforced polymer laminates under transverse compression. Technical report, Chalmers University of Technology, 09 2016.
- [67] M. Ridha, C.H. Wang, B.Y. Chen, and T.E. Tay. Modelling complex progressive failure in notched composite laminates with varying sizes and stacking sequences. *Composites Part A*, 58(0):16–23, 2014.
- [68] V.W. Rosen. Mechanics of composite strengthening. *Fiber Composite Materials*, 8(3):37–75, 1965.
- [69] W. Slaughter, N. Fleck, , and B. Budiansky. Compressive failure of composites: the roles of multiaxial loading and creep. *Journal of engineering materials and technology*, 115(3):308–313, 1993.
- [70] K. Song, Y. Li, and C.A. Rose. Continuum damage mechanics models for the analysis of progressive failure in open hole tension laminates. *Collection of Technical Papers*, 2011.
- [71] Z.C. Su, T.E. Tay, M.Ridha, and B.Y. Chen. Progressive damage modeling of open-hole composite laminates under compression. *Composite Structures*, 122:507–517, 2015.
- [72] S. C. Tan. Finite width correction factors for anisotropic plate containing a central opening. *Journal of Composite Materials*, 22:1080–1097, 1988.
- [73] Vedad Tojaga, Simon P.H. Skovsgaard, and Henrik Myhre Jensen. Micromechanics of kink band formation in open-hole fibre composites under compressive loading. *Composites*, Part B(149):66–73, 2018.
- [74] A. Turon, C.G. Davila, P.P. Camanho, and J. Costa. An engineering solution for solving mesh size effects in the simulation of delamination with cohesive zone models. *Engineering Fracture Mechanics*, 74(10):1665–1682, 2007.
- [75] B.R. van Dongen. Progressive damage modelling of frps using a blended stress-strain and fracture mechanics approach in fem. Technical report, Delft University of Technology, 6 2017.
- [76] A. M. Waas and W. Schultheusz. Compressive failure of composites, part i: Testing and micromechanical theories. *Progress in Aerospace Sciences*, 32(1):1–42, 1996.

-
- [77] J. M. Whitney and R. J. Nuismer. Stress fracture criteria for laminated composites containing stress concentrations. *Journal of composite materials*, 8(3):253–265, 1974.
- [78] Libin Zhao, Jie Zhi, Jianyu Zhang, Zhanli Liu, and Ning Hu. Xfem simulation of delamination in composite laminates. *Applied Science and Manufacturing*, 80:61–71, 2016.